Mechanisms and consequences of μ-opioid receptor dimerization

Mechanismen und Konsequenzen der μ-Opioid-Rezeptor-Dimerisierung

Doctoral thesis for a Doctoral degree
at the Graduate School of Life Sciences,
Julius-Maximilians-Universität Würzburg,
Section Biomedicine
submitted by

Jan Möller
from Gelnhausen, Germany

Würzburg, 2020

Mechanisms and consequences of μ-opioid receptor dimerization

Mechanismen und Konsequenzen der μ-Opioid-Rezeptor-Dimerisierung

Doctoral thesis for a Doctoral degree
at the Graduate School of Life Sciences,
Julius-Maximilians-Universität Würzburg,
Section Biomedicine
submitted by

Jan Möller
from Gelnhausen, Germany

Würzburg, 2020

Submitted on: ……..……..

Office stamp

Members of the Promotionskomitee:

Chairperson: **Prof. Dr. Manfred Gessler**

Primary Supervisor: **Prof. Dr. Martin J. Lohse**

Supervisor (Second): **Prof. Dr. Markus Sauer**

Supervisor (Third): **Prof. Dr. Marta Filizola**

Date of Public Defence: ……..……

Date of Receipt of Certificates: ……

Affidavit

I hereby confirm that my thesis entitled "**Mechanisms and consequences of μ-opioid receptor dimerization**" is the result of my own work. I did not receive any help or support from commercial consultants. All sources and / or materials applied are listed and specified in the thesis.

Furthermore, I confirm that this thesis has not yet been submitted as part of another examination process neither in identical nor in similar form.

Place, Date Signature

Eidesstattliche Erklärung

Hiermit erkläre ich an Eides statt, die Dissertation „**Mechanismen und Konsequenzen der μ-Opioid-Rezeptor-Dimerisierung**" eigenständig, d.h. insbesondere selbständig und ohne Hilfe eines kommerziellen Promotionsberaters, angefertigt und keine anderen als die von mir angegebenen Quellen und Hilfsmittel verwendet zu haben.

Ich erkläre außerdem, dass die Dissertation weder in gleicher noch in ähnlicher Form bereits in einem anderen Prüfungsverfahren vorgelegen hat.

Ort, Datum Unterschrift

Mechanisms and consequences of μ-opioid receptor dimerization

Doctoral thesis by

Jan Möller

Abstract

One third of all market approved drugs target G protein coupled receptors (GPCRs), covering a highly diverse spectrum of indications reaching from acute anti-allergic treatment over blood-pressure regulation, Parkinson's disease, schizophrenia up to the treatment of severe pain. GPCRs are key signaling proteins that mostly function as monomers, but for several receptors constitutive dimer formation has been described and in some cases is essential for function. I have investigated this problem using the μ-opioid receptor (μOR) as a model system - based both on its pharmacological importance and on specific biochemical data suggesting that it may present a particularly intriguing case of mono- vs- dimerization. The μOR is the prime target for the treatment of severe pain. In its inactive conformation it crystallizes as homodimer when bound to the antagonist β- funaltrexamine (β-FNA), whereas the active, agonist-bound receptor crystallizes as a monomer. Using single-molecule microscopy combined with super-resolution techniques on intact cells, I describe here a dynamic monomer-dimer equilibrium of μORs where dimer formation is driven by specific agonists. The agonist DAMGO, but not morphine, induces dimer formation in a process that correlates temporally and, in its agonist, and phosphorylation dependence with β-arrestin2 binding to the receptors. This dimerization is independent from but may precede μOR internalization. Furthermore, the results show that the μOR tends to stay, on the cell surface, within compartments defined by actin fibers and its mobility is modulated by receptor activation. These data suggest a new level of GPCR regulation that links receptor compartmentalization and dimer formation to specific agonists and their downstream signals.

I finally present at the end of this work a few side- projects that have developed, based on methodological advances, during the course of these studies, addressing other research topics such as second messenger measurements at various wavelengths, GPCR activation measurements as well as intermediate receptor states.

Table of Contents

List of Figures

1. Introduction

1.1. Biological impact of G protein-coupled receptors and importance for therapy

More than 800 genes within the human genome encode for a sequence signature of seven-transmembrane (7TM) receptors. 7TM-receptors are commonly referred to as G protein- coupled receptors (GPCRs), since most of them signal through heterotrimeric G proteins[1]. GPCRs represent the largest family among cell- membrane receptors and allow organisms to receive and promote signals from the environment, from other organisms or from themselves to intracellular structures. The activation of such receptors is followed by coupling and activation of G proteins relaying the signal to other signaling proteins, responding via a second messenger to the stimulus. The stimuli for these receptors cover a broad range reaching from light, ions, mechanical force, neurotransmitters, hormones to other proteins and for sure several more unmentioned triggers. One third of all market approved drugs target G protein coupled receptors, covering a highly diverse spectrum of indications reaching from acute anti-allergic treatment over blood-pressure regulation, HIV, Parkinson's disease, schizophrenia to the treatment of severe pain.

1.2. Structure and activation of G-protein-coupled receptors

Based on their sequence homology and thereby their structural similarity, GPCRs within the human genome are classically divided into five families[2]: Class A (rhodopsin), class B (secretin), class C (glutamate), adhesion and frizzled/taste2. Apart from these classes, several orphan GPCRs, e.g. GPR107, GPR143 and a few others have not been assigned to any of the other families. Class A, which covers also the receptors studied in this work, is by far the largest and most diverse GPCR family and comprises highly conserved sequence motifs, structural similarities and the following shared activation mechanisms[3].

Most prominent is that all GPCRs consist of seven transmembrane domains (TMs), which are embedded in the phospholipid double layer of cell-membranes (**Figure 1**). The TMs are connected via three extracellular (ECLs) and three intracellular loops (ICLs) of varying length. ECLs often contain disulfide bridges to maintain loop stability and preserve the three-dimensional structure of the GPCR[4]. TM7 is followed by an intracellular, class-dependent more or less complex C-terminal end and contains most prominent in class A GPCRs also a helix 8 (H8). For a better comparison of individual GPCR structures with each other, the Ballesteros–Weinstein numbering system prevails[5], which indicates with its first number the TM of the GPCR. The second number indicates the relative position to the highest conserved amino-acid residue, which is assigned the number 50. The TMs contain several highly conserved motifs, most important the DRY-motif (TM3), the CWxP- motif (TM6) and the NPxxY. motif (TM7).

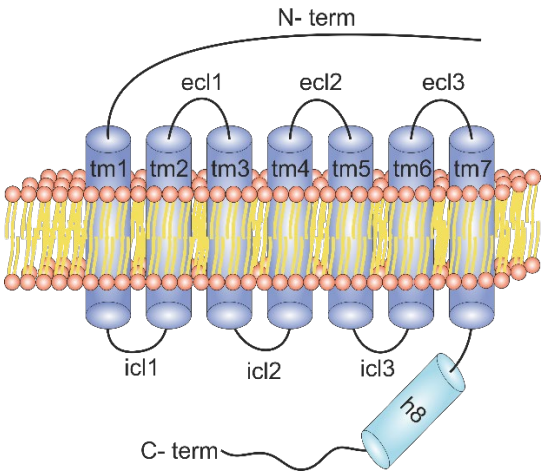

Figure 1: General structure of GPCRs:
Shown is the sequence of the general structural elements embedded into a phospholipid bilayer. The extracellular parts are mainly involved in ligand binding and induce conformational changes during activation. In contrast the intracellular parts are responsible for the signaling of the GPCR as well as the allosteric stabilization of the active state by G proteins. Phosphorylation sites on the intracellular part (mostly C-terminal) can be phosphorylated e.g., by G protein-coupled receptor kinases (GRKs) and induce thereby β-arrestin recruitment, leading to further signaling opportunities and/or signal termination.

GPCRs have a ligand binding domain exposed to the extracellular surface and a G protein coupling domain formed by the intracellular structures. The ligand-binding domain is decisive for the selective activation of a GPCR by a corresponding stimulus. The orthosteric binding pocket for class A GPCRs is formed by the extracellular TM region, mainly by residues of TM3, 5, 6 and 7- helices[6], whereas the ligand binding of glutamate and other class C receptors is rather taking place at the N-terminus[7]. Ligand binding is mostly mediated via salt-bridges, hydrogen bonds or hydrophobic interactions, but can also be covalently supported as in the prototypical class A GPCR rhodopsin. Here, the inactive ligand 11-cis-retinal is bound covalently to a lysine in TM7 and gets transferred upon light absorption to the active isomer all-trans-retinal, which causes receptor activation.

Receptor activation itself, even though intensively studied at the moment, is not entirely understood yet, since it is a fast process and thereby difficult to study on a molecular level. Structural data, mainly based on crystallographic discoveries of the same GPCRs in both active and inactive state (e.g. β_{2-} adrenergic receptor, M2 muscarinic receptor, A_{2A} adenosine receptor, rhodopsin, κ- opioid receptor and the μ-opioid receptor) helped to develop models which show common mechanisms of GPCR activation among class A receptors. One shared feature is the contraction of the binding pocket after agonist binding, allosterically enhanced by G protein- coupling, and often contributing to high- affinity binding of such compounds[8]. Another common mechanism is an intracellular gap opening due to a 5-14 Å cytoplasmatic outward movement of TM6, which is amplified , most prominent in the β_2 adrenergic receptor, owing to the strong kink of this TM[9], and a less pronounced inward movement of TM7. The gap opening allows the C- terminal alpha helical domain of the corresponding G protein to dock into the receptor core[6]. A salt- bridge between the highly conserved DRY- motif and TM6 stabilizes the inactive state, whereas the active state is mainly stabilized by polar interactions between the DRY- motif, the NPxxY- motif and some other polar contacts between TM4 and TM5 (**Figure 2**). Via a network between TM3, TM6, TM7 and the G protein, the active state is further steadied[10]. Several recent studies propose furthermore micro switches and intermediate receptor states of short lifetime[11,12], which a receptor might adopt after agonist application, before ultimately reaching the active state.

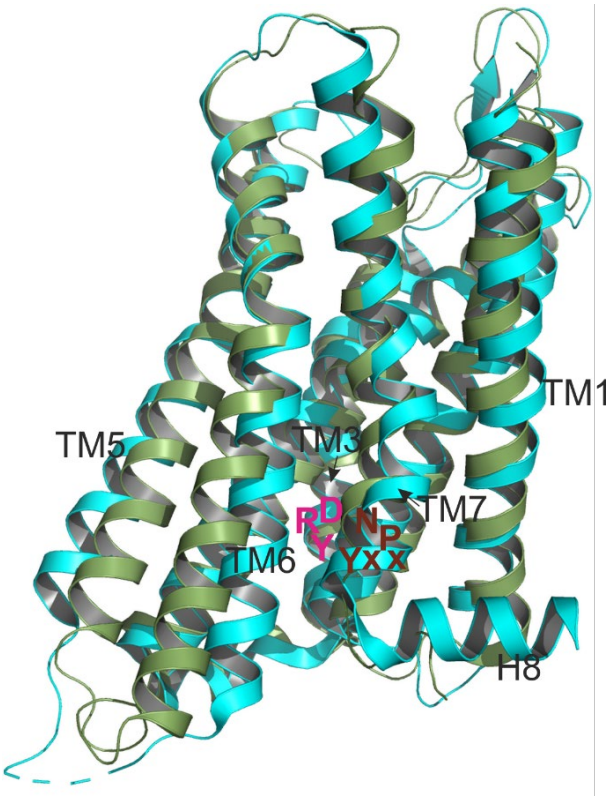

Figure 2: Overlay of the inactive/active μOR structures
Shown is an overlay of the inactive (cyan) and active (dark green) crystal structures of the μOR. The most prominent movement is the 10 Å outward displacement of the intracellular part of TM6 upon receptor activation. The conserved DRY-motif (magenta letters) is roughly indicated to show the spatial proximity to the NPxxY motif (dark red).

Image was plotted using PyMOL according to the crystal structures 4DKL (inactive state) and 5C1M (active state) of the μOR.

However, while agonist and antagonist binding interactions differ among GPCRs, the activation pathways that agonists initiate nevertheless converge close to the transducer-binding region[13]. From an evolutionary point of view, GPCRs seem to have evolved distinct pockets and mechanisms that bind ligands to initiate activation, retaining similar conformational changes after activation on the intracellular side to interact with their downstream effectors.

Even though it was already seen in the late seventies, by the lab of Robert Lefkowitz, that the presence or absence of G proteins in radioligand binding assays influences agonist binding[14,15], G proteins were classically seen as effector proteins of GPCRs rather than allosteric influencers of the receptor. More recent studies showed also agonist independent influences of G proteins on the receptor[8,12] and in the last year the Kobilka lab obtained an active/intermediate state structure of the β_2-adrenergic receptor, stabilized with the carboxyl terminal 14 amino acids of $G\alpha_s$[16]. Such studies show that the G protein can be more than just an effector protein of the GPCR, and even though it is presumably not necessary for receptor activation, it facilitates and stabilizes the active state of several prototypical GPCRs also in the absence of agonists. The next years will show if this is also true for other receptors than class A and/or if this is even a general feature of all GPCRs.

1.3. Downstream signaling of GPCRs and feedback mechanisms

The most prominent direct signaling partners of GPCRs are G proteins themselves, and following GRK-mediated phosphorylation, β-arrestins. G proteins as heterotrimeric complexes of three different subunits are generally referred to by their α-subunit, and 16 genes for α-subunits, comprising 23 different α-subunits, five β-subunits as well as 12 γ-subunits have been identified[17]. G proteins are based on their main functionalities assigned to four different families: G_s proteins, which stimulate the adenylyl cyclases; G_i, proteins, which inhibit the adenylyl cyclases and can further activate inwardly rectifying potassium channels; G_q proteins, which activate the phospholipase C and finally $G_{12/13}$ proteins which signal mainly to guanine nucleotide exchange factors for the Rho small GTPases[1]. In addition, the βγ-subunits can activate in a cell and tissue dependent manner several different effectors such as ion-channels or mitogen-activated protein kinases (MAP-kinases), making G protein mediated signaling highly diverse.

G protein coupling selectivity towards the receptors is complex and so far, even though decisive for GPCR signaling, not fully understood. Recent computational approaches to identify critical amino-acid residues and three dimensional arrangements for the alpha-helical domains[10] could now be confirmed with structural data for this domain of G_s in complex with the β_2 adrenergic receptor[16].

The Gα subunit of G proteins is in the basal state bound to guanosine diphosphate (GDP). The βγ-subunit is a stable complex that does not dissociate under native conditions. However, usually ligand binding is inducing a conformational change on the receptor, leading to an outward displacement of TM6 and opening of an interface for G protein coupling, which seems to be facilitated by the third intracellular loop of the receptor[18,19]. The binding of G protein is usually further stabilizing the active receptor state. Subsequently, GDP is exchanged by guanosine triphosphate (GTP) and this leads to G protein activation due to a conformational change of the α-subunit (**Figure 3**). Consequently, the βγ-subunit dissociates from the α-subunit. The subunits target afterwards their effector proteins and cause the corresponding cellular signaling. Signal termination is facilitated by GTPase activating proteins, which enhance the GTPase activity of the Gα-subunit, and GTP becomes hydrolyzed to GDP. As a result, the GDP bound α-subunit turns back into the basal/inactive state and associates again with a βγ- subunit.

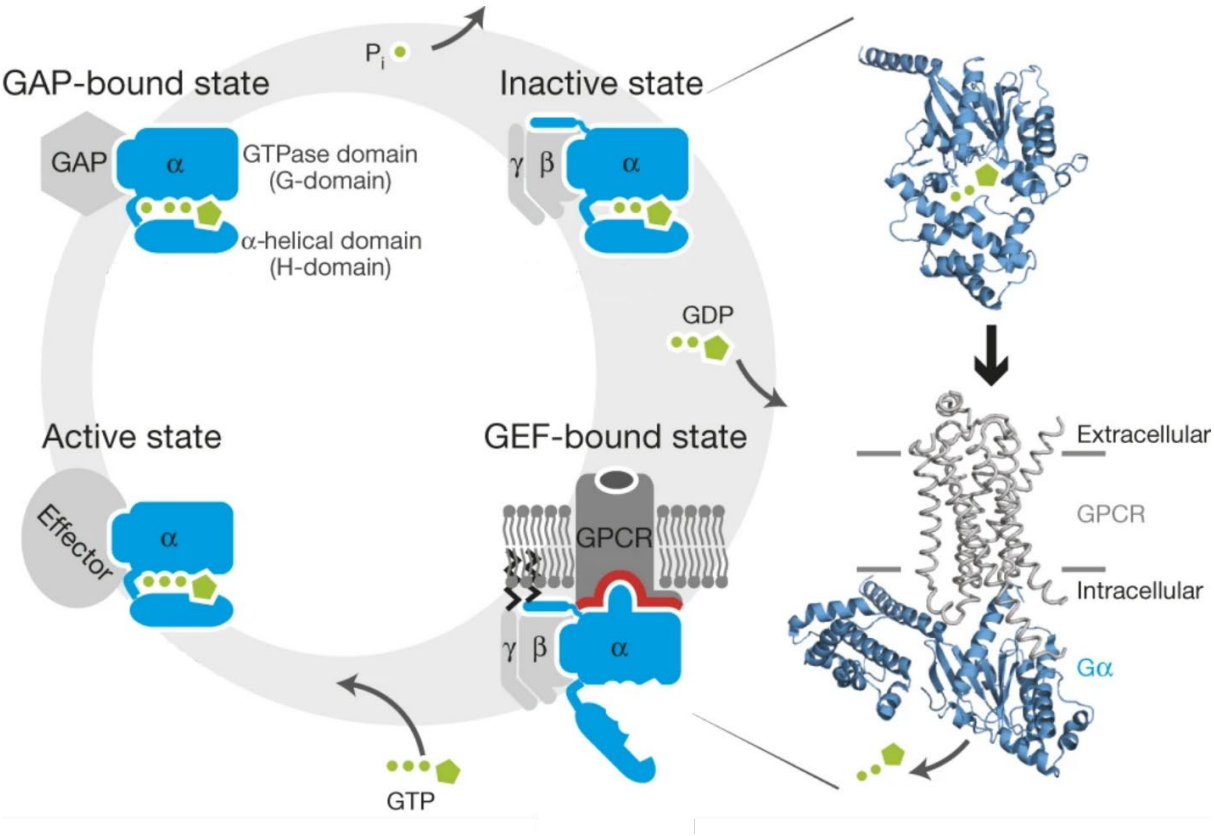

Figure 3: G protein activation/deactivation cycle

The basal/inactive GDP-bound heterotrimeric G protein complex binds to a guanine nucleotide exchange factor (GEF≈ GPCR) , the α-subunit turns into the open conformation, GDP is released and exchanged by GTP. This leads to the active state of Gα, causing βγ- dissociation and both subunits target their corresponding effector proteins. GTPase activating proteins bind and initiate signal termination. Afterwards GTP is hydrolyzed and the α-subunit returns to the basal/inactive conformation and can associate again with βγ.

Adapted with permission from [*Springer Nature*]: [Nature] [Reference[10] (Universal allosteric mechanism for Gα activation by GPCRs, Tilman Flock et al), [Copyright © 2015, Springer Nature] (2015).

Continuous GPCR activation can ligand- and receptor- dependent lead to distinct phosphorylation by G protein-coupled receptor kinases (GRKs). Subsequently, β-arrestins are recruited and can either cause further signaling or signal termination due to receptor internalization. This cellular feedback mechanism is discussed in more detail in (**Figure 7**), following page **22,** and to avoid redundancy is not further elaborated here.

1.4. GPCR dimerization

Whereas it is nowadays well accepted that class C GPCRs form and function as dimers[20], the meaning and importance of class A dimerization is still not sufficiently understood. While there were initial believes that dimerization might be a requirement for G protein activation, convincing studies with single receptors, including the μOR, reconstituted in nanodiscs showed that this is not the case[21–23].

However, these results do not exclude the existence or another physiological meaning of class A dimerization in living cells. The number of class A receptors reported to dimerize or even to form higher order oligomers raised dramatically, when fluorescence and bioluminescence resonance energy transfer (BRET and FRET, respectively) based whole cell assays became fashionable laboratory practice[24–27]. Even though these assays might be able to report GPCR oligomerization in a qualitative way, they lack information about oligomer sizes, cellular localization, and their respective lifetime.

More details on such properties have been elucidated by advanced microscopy techniques, such as total internal reflection fluorescence (TIRF) microscopy and confocal microscopy-based approaches. Single-molecule-TIRF microscopy gives directly access to the oligomeric size, the localization of oligomers on the cell-membrane as well as their lifetimes, and has unveiled such information for several prototypical class A GPCRs[28–30]. However, single-molecule microscopy on living cells is limited to a density of fluorescent molecules which might be for several GPCRs below the physiological expression level. Confocal based fluorescence fluctuation spectroscopy (FFS) as a statistical approach can work at higher expression levels and can serve as a complementary method. The method stays short, however, regarding information about oligomer lifetimes, and the ability to deconvolve individual oligomer fractions has been disputed recently[31–33].

Enormous progress in structural research has given insights into the quaternary organization of dimeric GPCR structures and has suggested certain dimer interfaces. The crystal structure of the inactive μOR proposed a TM5-TM6 interface with a surface area of 1492 Å^2 as well as a TM1-TM2-H8 interface of 615 Å^2 between individual receptor protomers[34]. Whereas the TM1-TM2-H8 interface is compatible with an inactive as well as an active receptor structure, the TM5-TM6 interface is due to a steric clash, caused by the 10 Å outward displacement of TM6 upon activation, just compatible with an inactive receptor state[35] (**Figure 4**). A TM5-TM6 interface was also proposed in the crystal structure of the chemokine receptor CXCR4[36], whereas TM1-TM2-H8 interfaces have been suggested for the κ-opioid[37], the β_1-adrenergic receptor (β_1AR)[38], and photoactivated rhodopsin[39]. This might leave room to speculate that dimerization at TM1-TM2-H8 interfaces underlies a distinct mechanism from TM5-TM6 dimerization and might even be linked to an active receptor conformation.

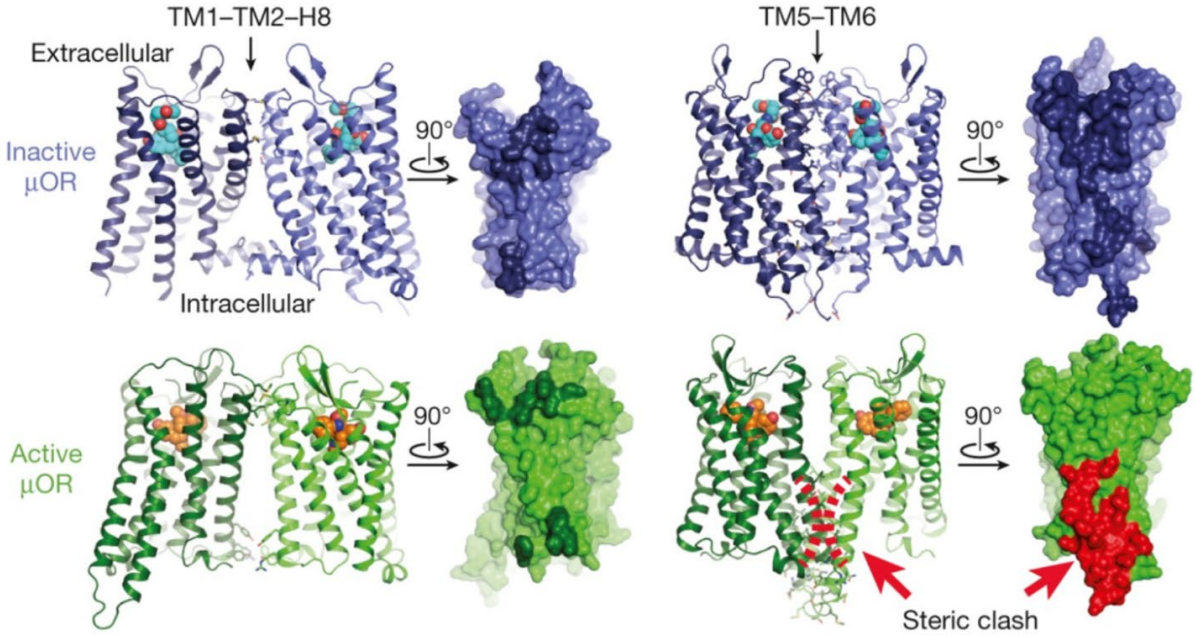

Figure 4: μOR dimer interfaces and compatibility with receptor state
An interface between TM1–TM2 and helix 8 (H8) is observed in both inactive and active structures of the μOR. The residues comprising the interface are highlighted in dark colours on the surface view. The TM5–TM6 interface observed for inactive μOR is not compatible with the active state due to clashing residues in TM5 and TM6 (highlighted in red). Adapted by permission from [*Springer Nature*]: [Nature] [Reference[35] (Structural insights into μ-opioid receptor activation, *Huang, W. et al*), [Copyright © 2015, Springer Nature] (2015).

Apart from studies on GPCR homodimers, there is also an almost countless number of heterodimers that have been reported. Some works show convincing results for positive and negative allosteric modulation of receptor heterodimers and recommend them as selective drug targets[40–42] . Criticism of such studies was raised by N. Lambert and J. Javitch[43], since several of these studies focus on a second messenger as readout instead of directly showing an effect between receptor protomers. Therefore, these authors raise doubt if the relevance of this receptor crosstalk might be overestimated for pharmacological implications. One of the rare studies which showed directly receptor protomer mediated effects is the heterodimer formed between the α_{2A}-AR and the μOR[41]. Since hetero-dimerization or even hetero-oligomerization of several different GPCRs leads quickly to a highly complex scenario, this work stayed focused on homodimerization of the μOR.

Even though it would be expected that with advancing methodologies the results about receptor oligomerization would become more consistent, this has not been yet achieved for class A GPCRs[44,45]. Obvious reasons for these diverse results are the differences in the experimental conditions such as the assay itself, but also the cell type, temperature, labeling technique as well as the way how the data is finally analyzed. To facilitate comparison, to understand if and how, and even more importantly under which experimental conditions individual GPCRs dimerize, databases as the GPCR-Oligomerization Knowledge Base (GPCR-OKB)[46] have been established and contribute to an improved transparency. Additionally, it would of course be desirable to cover a broad range of different methods and conditions in individual studies to understand the critical parameters involved in receptor dimerization.

Until clearly defined structural and functional properties of GPCR dimers have been determined, the question stays open if class A dimers and oligomers exist and whether they are comprising different signal properties in contrast to their individual entities[43]. With the present work, I aim to close this gap of information for the μOR by complementing the existing structural information[19,34,35] with functional data, using a variety of different experimental approaches and conditions.

1.5. Opioid receptors and the μ- opioid receptor

Even though first traces of history about the usage of *Papaver somniferum*, the plant which produces opium, go back to 4,000 B.C., the molecular existence of opioid receptors and their endogenous ligands was just described in more recent times[47]. Opium was already known early as a pain-relieving drug and went during history through episodes of blessing and curse. Opium is the dried latex rinsing out of cut poppy seeds and contains the opiates morphine, codeine and thebaine along with other non-analgesic alkaloids of which are most prominent papaverine and noscapine. Opioid receptors are GPCRs and classically divided into the three subtypes **μ**, **κ** and **δ**. They have in common that they are Gi-coupled and mediate via this an inhibition of adenylyl cyclases. Since several years there is an ongoing debate about the existence of another subtype[48], the nociceptin receptor, which shows high structure and sequence similarity, but doesn't display the pharmacological profile of ligands as the classical opioid receptors[4].

The μ-opioid receptor is the prime target for the treatment of severe pain and due to that of high clinical interest. Unfortunately, the successful treatment of pain comes with a series of side effects such as respiratory depression, constipation and sedation. Apart from that, repeated opioid application causes a physical drug dependency, which limits the clinical usage of these drugs and causes societal problems, most prominent for the morphine derivative heroin. Even though the sedation makes opioids like remifentanil, sufentanil and alfentanil popular as injection-narcotics with effective pain treatment, the usage requires, due to the small therapeutic window, a careful dosage application to avoid lethality.

The endogenous ligands of the opioid receptors are peptides, derived from various precursors, and exhibit different subtype selectivity[49]. Besides endomoprhin-1 and 2, which are highly selective for the μ-opioid receptor (μOR)[50], they all contain the conserved motif Tyr-Gly-Gly-Phe (YGGF). Since the pharmacophoric sequences (message) are identical, the subtype selectivity (address) is mediated by the extension of the sequence. Judging purely based on the peptide sequence, an extension of the sequence by leucin and two positively charged amino acid residues might contribute to a subtype selectivity for κ-opioid receptors.

Precursor	Opioid	Selectivity	Sequence
Unidentified[51]	Endomorphin-1	μ	YPWF
Unidentified[51]	Endomorphin-2	μ	YPFF
Proopiomelanocortin	β-Endorphin	μ ≈ δ	YGGFMTSEKSQTPLVTLFKNAIIKNAY-KKGE
Proenkephalin	Met-Enkephalin	δ > μ	YGGFM
	Leu-Enkephalin	δ > μ	YGGFL
	Methorphamide	μ	YGGFMRRV-(NH_2)
Prodynorphin	Dynorphin A	κ	YGGFLRRIRPKLKWDNQ
	Dynorphin B	κ	YGGFLRRQFKVVT
	α-Neo-endorphin	κ	YGGFLRKYPK
	β-Neo-endorphin	κ	YGGFLRKYP

Table 1: Endogenous opioid peptides, precursors, sequence and selectivity profile[49,52–54]

A shared structural element, which most opioid agonists (including the endogenous ones) carry, is an electron-rich aromatic residue (or at least a structural element with delocalized π-electrons), connected via 2 C-atoms to a basic nitrogen atom (**Figure 5**). Since this tyrosine based structural element alone is also present in other physiological molecules as e.g. catecholamines, it might be essential for functionality but not for the selectivity towards opioid receptors. Selectivity and affinity are, therefore, rather mediated via other surrounding structural elements. A comparison of the YGGF motif's chemical structure with morphine, as in **Figure 5**, shows that these molecules might be able to exhibit a similar pose in the receptor's binding pocket, since their functional groups comprise similar physicochemical properties, positions and distances.

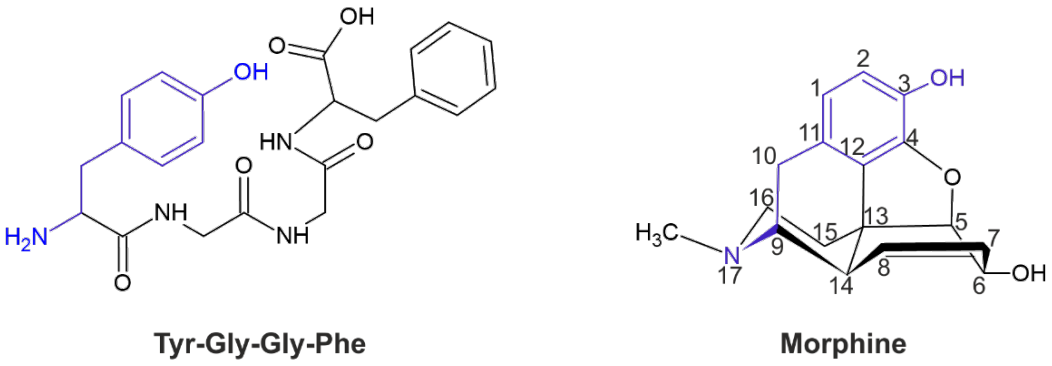

Figure 5: Structures of the YGGF motif and morphine
The left structure depicts the first 4 amino acids, which are incorporated in all endogenous opioid peptides, besides the endomorphins. The right structure is morphine with stereochemistry and numbering according to IUPAC. Highlighted in blue is the common pharmacophoric element of all endogenous opioid peptides and opioids which are based on a morphinan scaffold.

Latest advances in structural biology contributed decisively to molecular understanding of the μOR activation mechanism and its signaling. Apart from crystal structures of the inactive[34] and active[35] receptor conformation, most recent progresses in cryo electron microscopy (Cryo-EM) unveiled a structure of the μOR with its cognate G protein[19]. The active state crystal structure of the μOR with a morphinan scaffold agonist[35] reveals a binding motif which involves apart from the earlier dicovered[55] salt bridge at D147$^{3.32}$ and hydrogen bond at H297$^{6.52}$ also the residues Y148$^{3.33}$, K233$^{5.39}$, Y326$^{7.43}$ (**Figure 6**). The hydroxy group in position 3 of the morphinan agonist is, based on these results, rather forming a polar network of hydrogen bonds including H297$^{6.52}$, Y148$^{3.33}$ and K233$^{5.39}$ instead of a single hydrogen bridge with H297$^{6.52}$. This causes a rotation of TM6 and thereby an intracellular outward movement of TM6 by 10 angstroms (Å)[35], opening the cavity for the α-helical domain of Gi proteins[19]. Additionally, the hydroxy group of Y326$^{7.43}$ associates with the free electron pair of the carboxyl-group of D147$^{3.32}$ and brings thereby the extracellular part of TM7 a few angstroms closer to the receptor core. As described before in mutagenesis based studies[55] D147$^{3.32}$ itself is interacting due to a salt bridge with the basic nitrogen atom of the agonist (Position 17 in morphine).

The inactive crystal structure[34] of the μOR points out that also for antagonist binding the salt bridge at D147$^{3.32}$ is essential. The size and electron density of the residue connected to the antagonist's nitrogen (in **Figure 6** an allyl-group) leads to a repulsion of Y326$^{7.43}$, which excludes the association of its hydroxy group with the free electron pair of the carboxy group in D147$^{3.32}$ and thereby the formation of an hydrogen bond between TM3 and TM7. Following Y148$^{3.33}$ cannot reach out to K233$^{5.39}$ and contribute to the polar network among Y148$^{3.33}$, K233$^{5.39}$ and H297$^{6.52}$. Instead Y148$^{3.33}$ seems to form a hydrogen bound with the free electron pair of the oxygen bridge between position 4 and 5. Moreover, a hydrogen of K233$^{5.39}$ is associating with the carboxyl group in position 6 of the antagonist, whereas H297$^{6.52}$ is linking, via two water molecules, with the hydroxy group in position 3. This arrangement does not cause the TM6 rotation, required for an intracellular outward movement of TM6, and the receptor remains rather in the inactive conformation.

Interestingly the differences in positions and orientations of the agonist vs antagonist binding are quite subtle and reject thereby a previous hypothesis[56] of functional antagonism due to a deeper binding of antagonists.

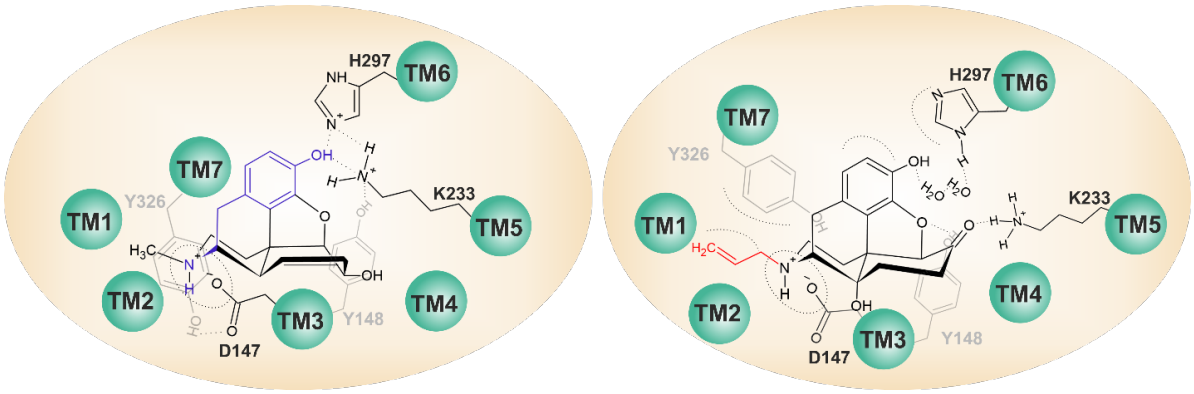

Figure 6: Binding poses of agonist and antagonist adapted from μOR structures[19,34,35,57]
The left binding pocket shows an illustration of agonist binding using morphine as an example. The right binding pocket contains naloxone and illustrates antagonist binding. The shown salt- bridges, shared hydrogen bonds as well as the electronic repulsions are indicated by dashed lines/circles based on the observations in the referenced cryo-EM and crystal structures.

After μOR activation and G protein recruitment, the GDP/GTP exchange leads to G_i protein activation and subsequent dissociation of the βγ-subunit. The G protein subunits can exhibit in a cell and tissue dependent manner, with deviating prominence, different signaling pathways (**Figure 7**). Generally, inhibition of adenylyl cyclases by $G\alpha_i$ leads to a lower production of cyclic adenosine monophosphate (cAMP) and subsequently to a reduced activity of protein kinase A (PKA). Whereas PKA has a huge variety of targets, for neuronal opioid signaling the reduced phosphorylation of voltage-gated calcium channels is of central importance[58]. Furthermore, there are several lines of evidence for $G\alpha_i$ mediated phosphorylation of cytosolic ERK[59,60]. The most prominent contribution of Gβγ towards μOR signaling is the inhibition of voltage-gated calcium channels to reduce neuronal depolarization[61] as well as the activation of inward rectifying potassium channels (GIRK/KIR3.x). Activation of GIRK is terminated by $G\alpha_i$-GTP hydrolysis to $G\alpha_i$-GDP and the reassociation with Gβγ[62,63].

μOR activation leads also to an agonist dependent recruitment of G protein-coupled receptor kinases (GRKs), predominantly GRK2, and causes thereby receptor phosphorylation[64,65] (**Figure 7**). Such phosphorylation leads further to the recruitment of β-arrestins, where for the μOR a major involvement of β-arrestin2 has been described[66,67]. Besides inducing internalization of the μOR, β- arrestins are also able to execute ligand dependent further signaling via MAP-kinases such as ERK, JNK and p38[68–70]. Furthermore, β-arrestin knock-down experiments have shown, that after μOR activation by morphine, Gβγ is able to activate protein kinase C (PKC) (via PLCβ) on the plasma membrane and thereby cause ERK phosphorylation without involvement of β-arrestin[59,68]. As for several other GPCRs, β-arrestin2 terminates also signaling of the μOR to G proteins, involving a protein complex of which most prominent partners are adapter protein 2 and clathrin (**Figure 7**). After internalization the receptor becomes either dephosphorylated and recycled to the cell surface or follows lysosomal protein degradation[71].

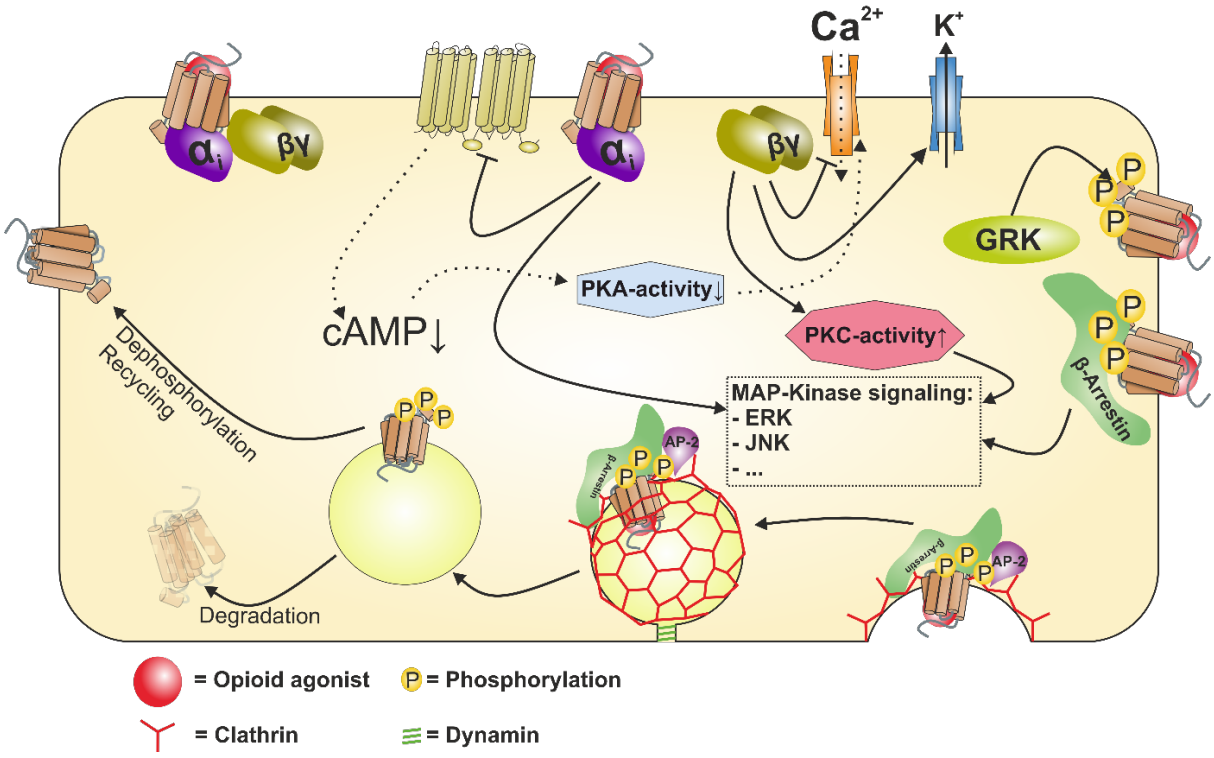

Figure 7: Signaling pathways of the μOR
Shown are the signaling cascades which can follow μOR activation. The immediate opioid responses are mediated through Ion channels and inhibition of adenylyl cyclases, followed by β- arrestin mediated signaling and ensuing MAP- kinase signaling, which results in altered gene transcription. Signaling of the μOR is terminated by receptor endocytosis and followed by either recycling to the cell surface or protein degradation.

The control of ion channels and reduced PKA activity mediated through μOR activation can explain the analgesic profile as well as the immediate pain-relieving effect of opioids. In contrast, withdrawal symptoms and drug addiction seem to be rather connected to a slower, long lasting signaling, as for example caused by MAP- kinases, since those are able to modify gene expression and neural plasticity[72].

The analgesic effect on the nociceptive system caused by μOR activation occurs mainly by opening of post-synaptic GIRK channels as well as the inhibition of pre-synaptic voltage-gated calcium channels. Whereas the activation of GIRK channels is leading to a hyperpolarization of the post- synaptic neuron, the reduced pre-synaptic calcium influx reduces the release of the exicitatory neurotransmitters such as glutamate or substance P (**Figure 8**). The following decreased concentration of those neurotransmitters in the synaptic cleft reduces the activation of the corresponding nociceptive receptors like the NMDA receptor and the NK_1-receptor, respectively[73].

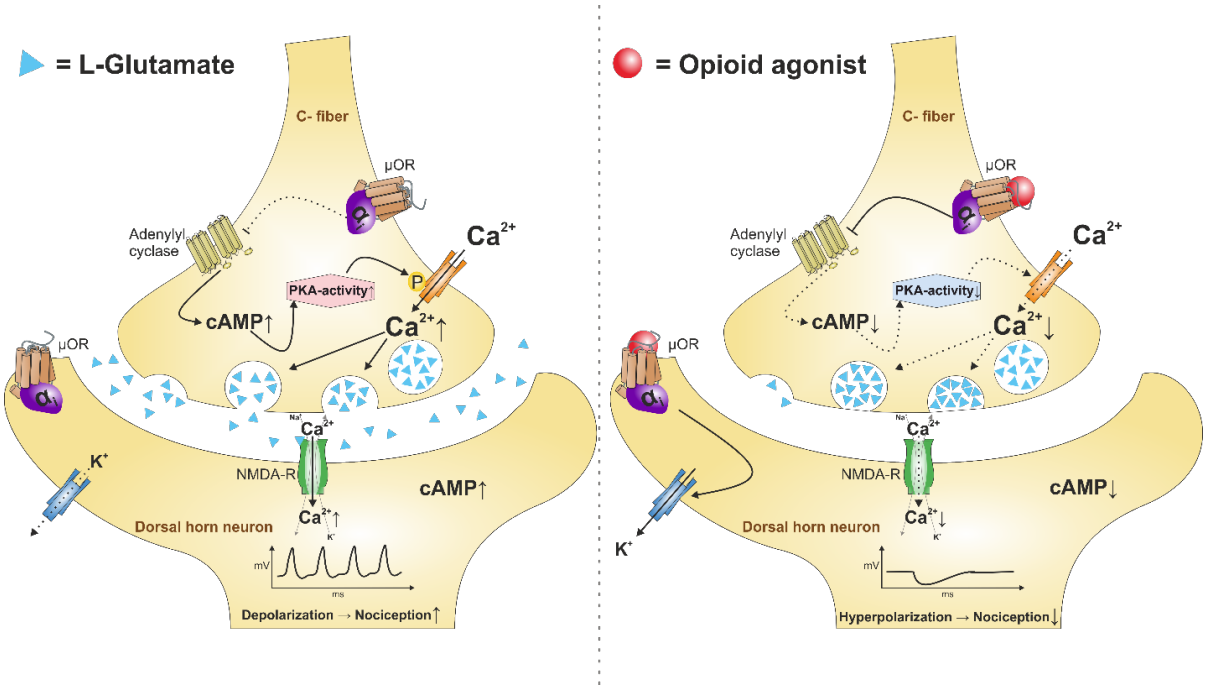

Figure 8: Inhibitory opioid effects and mechanisms of analgesia
μOR activation leads through the decreased release of excitatory neurotransmitters from the presynapsis and hyperpolarization of the postsynapsis to reduced pain perception.

Overall, opioids mediate antinociceptive efffects via a reduced excitability of pain transmitting neurons. μORs are highly expressed in brain regions that regulate pain perception such as thalamus, cingulate cortex, and insula, whereas the most prominent effect of endogeneuos opioids is mediated through descending inhibitory neurons to the dorsal horn[58,74]. Even though opioid drugs are understood to mainly mediate analgesic effects via the central nervous system, several groups repeatedly reported an underestimated influence of opioid mediated analgesia in the periphery[75,76]. However, μORs are also of high density in further brain regions and tissues, where they rather contribute to undesired side effects such as constipation, respiratory depression and opioid addiction (**Figure 9**) .

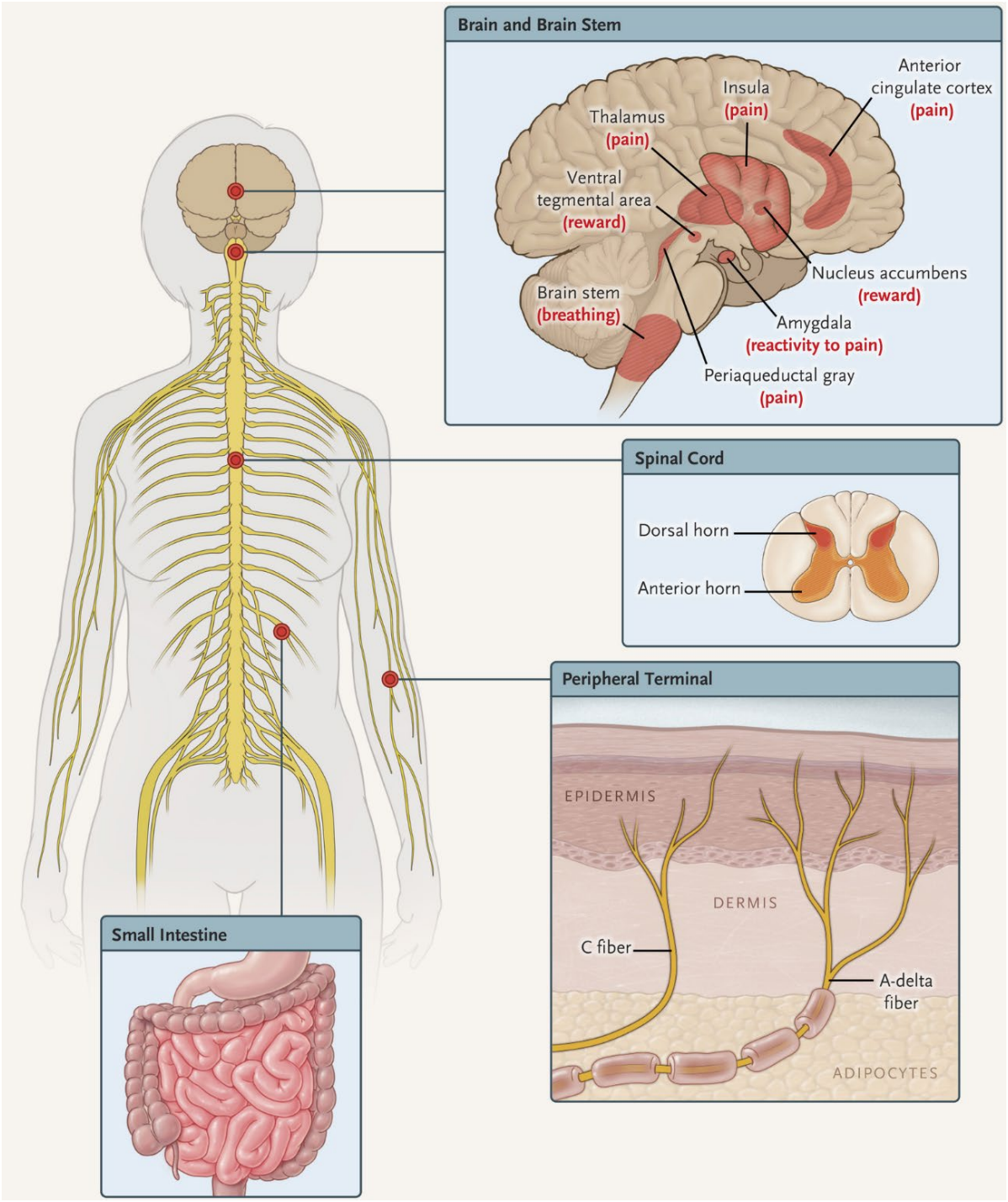

Figure 9: Local distribution of μORs

Shown are localizations of μORs in the human brain, with high concentrations in the thalamus, periaqueductal gray, insula, and anterior cingulate (regions involved with pain perception), in the ventral tegmental area and nucleus accumbens (regions involved with reward and thereby contributing to opioid addiction), in the amygdala (a region involved with emotional reactivity to pain), and in the brain stem (nuclei that regulate breathing and thereby mediate respiratory depression). In the spinal cord, a high concentration of μORs is located in the dorsal horn and thereby inhibits pain transmission from the periphery to the central nervous system. μORs in peripheral terminals modulate the perception of pain, and receptors in the small intestine reduce gut motility and lead to constipation. Reproduced with permission from (Volkow et al., 2016, Opioid Abuse in Chronic Pain — Misconceptions and Mitigation Strategies), Copyright Massachusetts Medical Society.

Attempts to develop safer opioids by targeting other receptor subtypes than μ were so far not successful. For instance, the targeting of the κ- subtype with pentazocine led to a therapeutic analgesia, but also to severe dysphoria and, due to an additional μ antagonism, to severe withdrawal symptoms of opioid addicted patients[77]. The therapeutic potential of the δ- subtype is controversial. Several groups proposed that targeting heterodimers of μ and δ might be beneficial[78–80], whereas others stated that dimerization in this regard might be of overestimated relevance[81]. Overall, the research on opioids has so far not achieved a breakthrough in discriminating the desired therapeutic effects from side- effects and risks of drug addiction. It stays open if the ongoing improvements in research technologies will at some point lead to a molecular understanding, precise enough to target opioid receptors in a way which allows an enhancement of desired opioid signaling over its undesired concomitants.

1.6. Fluorescence and resonance energy transfer

Fluorescence is the spontaneous emission of light after previous light absorption at a shorter wavelength. Materials or molecules which can exhibit this phenomenon are commonly called fluorophores. According to the Jablonski diagram (**Figure 10**), absorption of photons lifts electrons of a fluorophore to higher energy levels. Electrons can be either lifted directly or return, due to processes such as vibrational relaxations and internal conversions, from higher energy levels to the basal singlet excited state (S_1). Fluorescence is of short lifetime (10^{-9} – 10^{-6} s) and occurs when electrons return from the S_1 state to a lower energy level within the singlet ground state (S_0) and emit thereby photons[82]. Phosphorescence, which can last up to several seconds, requires that electrons undergo intersystem crossing, reach the triplet state T_1 and return from there to a singlet ground state[82]. The term "intersystem crossing" is related to an alternation of the electron spin. It causes that the transfer from T_1 to S_0 states is very slow and because of its small likelihood to occur is called "forbidden transition".[82]

Vibrational relaxation and solvent effects cause that the amount of energy contributing to fluorescence is smaller or at most equal to the energy taken up during absorption. As a result, the emission maximum is shifted to longer wavelengths compared to the absorption maximum. Apart from a few exceptions, this shift is for most fluorophores ≈ 20-30 nm and is commonly named Stokes shift (according to its discoverer, the Irish physicist George Gabriel Stokes).

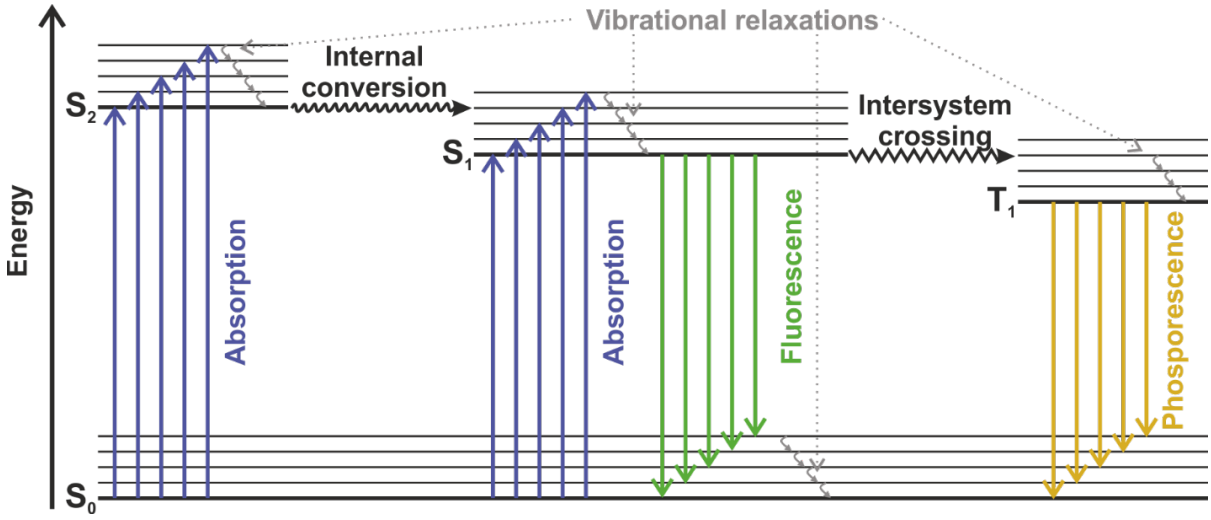

Figure 10: Jablonski diagram illustrating fluorescence
Absorption of photons by an atom or organic molecule can lift electrons from their basal energy level (S_0) to higher energy levels (S_1,S_2,S_n) including higher vibrational levels (thin lines). Due to internal conversion and vibrational relaxations the electrons can drop to the S_1 ground state. Emission of photons by means of fluorescence occurs when an electron is transferred from the S_1 ground state to a lower S_0 energy level. Phosphorescence occurs after intersystem crossing and transition from basal T_1 to S_0 states.

FRET (Förster resonance energy transfer) can occur if two fluorophores are in close proximity to each other and describes the non-radiative transfer of energy from one fluorophor (donor) to another one (acceptor). An essential requirement for FRET is that the emission spectra of the donor fluorophore and the excitation spectra of the acceptor molecule overlap[83]. The donor fluorophore can then, instead of emittiing light by itself, transfer the energy of electrons returning to S_0 to an acceptor fluorophore and thereby lift the acceptor's electrons to an excited singlet state (**Figure 11**).

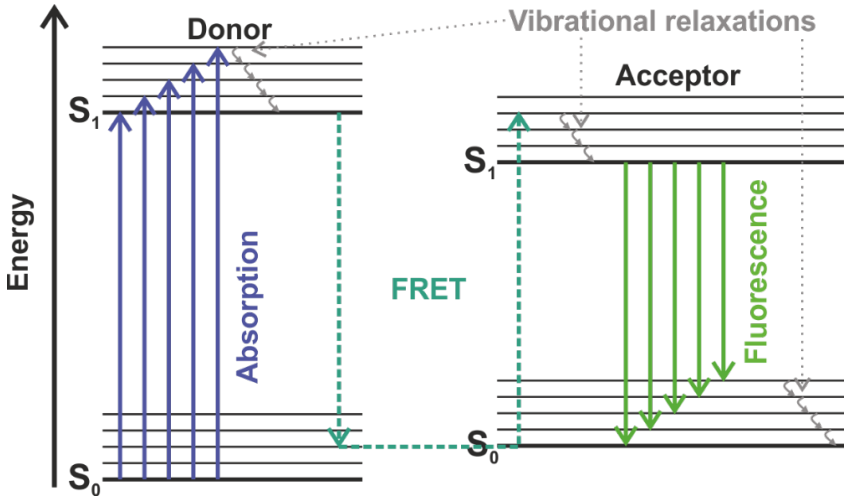

Figure 11: Jablonski diagram illustrating FRET
If two fluorophores are in close proximity, the donor fluorophore can transfer its energy in a non-radiative manner to the acceptor fluorophore and thereby lift electrons up to an excited singlet state. Return of electrons from basal S_1 to an S_0 state causes fluorescence emission by the acceptor molecule.

The distance for the half-maximum of energy transfer from one fluorophore to another one is defined as Förster radius or Förster distance (R_0)[84,85]:

$$R_0 = 0.2108 \left(\kappa^2 \phi_D n^{-4} \left(\int_0^\infty f_D(\lambda)\varepsilon_A(\lambda)\lambda^4 d\lambda\right)\right)^{1/6} \quad (1)$$

where κ^2 is the interdipole orientation factor (mostly assumed to be 2/3 corresponding to a random orientation), ϕ_D is the quantum yield of the donor in the absence of the acceptor, n the refractive index of the surrounding medium; f_D is the donor's fluorescence intensity in dependency of the wavelength (λ) ,and $\varepsilon_A(\lambda)$ is the wavelength-dependent extinction coefficient of the acceptor (in $M^{-1}*cm^{-1}$). The integral term represents the spectral overlap between the donor emission and the acceptor excitation (**Figure 12a**).

The FRET-efficiency (E) describes the percentage of energy transfer from a donor to an acceptor molecule. It depends inverse proportionally to the power of six on the distance r between donor and acceptor:

$$E = \frac{1}{1+\left(\frac{r}{R_0}\right)^6} \quad (2)$$

Due to its strict distance dependence (**Figure 12b**) FRET gained importance in an abundance of biological studies to measure distances, prove interactions and quantify intramolecular conformational changes. Measurements of FRET-efficiencies allow by use of the above equations a quite good estimate of the distance between fluorophores attached to biological entities such as proteins or nucleic acids. Even though a huge combination of useful FRET pairs has been reported, the majority of the currently used biological FRET sensors are based on the combination of cyan fluorescent protein variants (CFP) as donor with yellow fluorescent protein variants (YFP) as acceptor fluorophores[85].

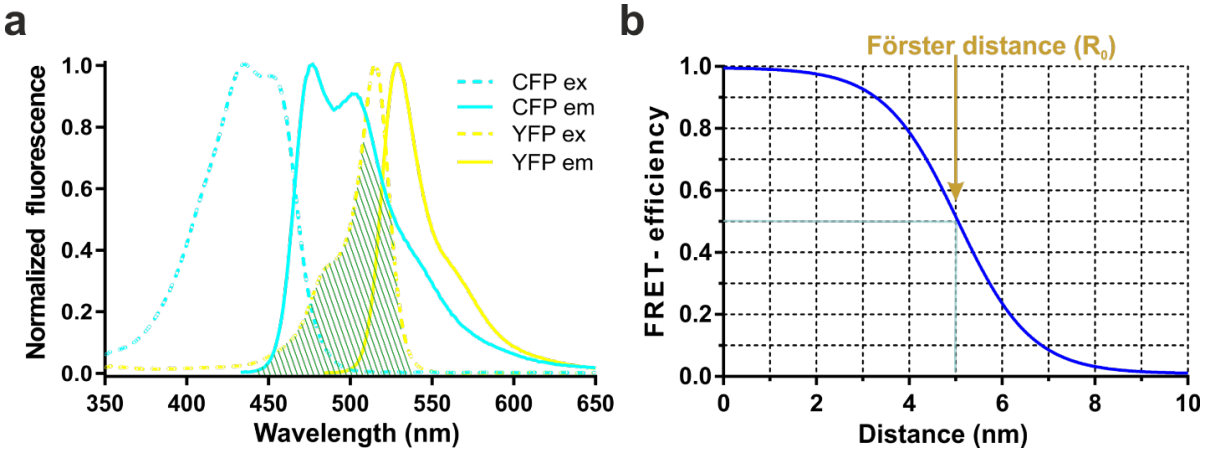

Figure 12: Spectral overlap, distance and FRET efficiency

(a), Excitation and emission spectra of CFP and YFP. The green hatched area shows the overlap between the donor emission and acceptor excitation spectra, which is a necessary requirement for FRET. (b), The graph illustrates the correlation between the distance of two fluorophores and their FRET- efficiency. The distance of 50% FRET efficiency is called Förster distance (R_0). Shown as an example is here correlation of the FRET- pair CFP-YFP, with an R_0 of 4,9 nm.

Development of new labeling techniques and continuous progress in the modification and optimization of fluorophores enabled FRET measurements at various wavelengths and even simultaneous measurements of several FRET sensors within one biological sample[86]. Nowadays, most of these measurements are conducted either by using fluorescence microscopy or with particularly robust sensors in high-throughput formats such as microtiter plates[87].

While biosensor FRET measurements are enormously supportive to investigate molecular mechanisms, it should be mentioned that such measurements come also with an assortment of issues which can ultimately lead to vague or meaningless results. Assuming that instrument sensitivities for donor and acceptor channels are balanced and that the donor-acceptor stoichiometry is stable, channel crosstalk impairs such measurements and requires often corrections to yield meaningful results. In several cases, the acceptor can be directly excited by the used excitation light (**Figure 13a**). Additionally, emission spectra of donor and acceptor can significantly overlap, causing that the donor emission leaks into the detection channel of the acceptor, an occurrence which is commonly named as "bleed-through"(**Figure 13b**). To minimize those issues, excitation light and detection optics for donor and acceptor channel should be carefully chosen. Furthermore, the selected fluorophores should always be measured individually on the used instrumental setup to estimate the impact of the channel crosstalk and to enable corrections for such occurrences.

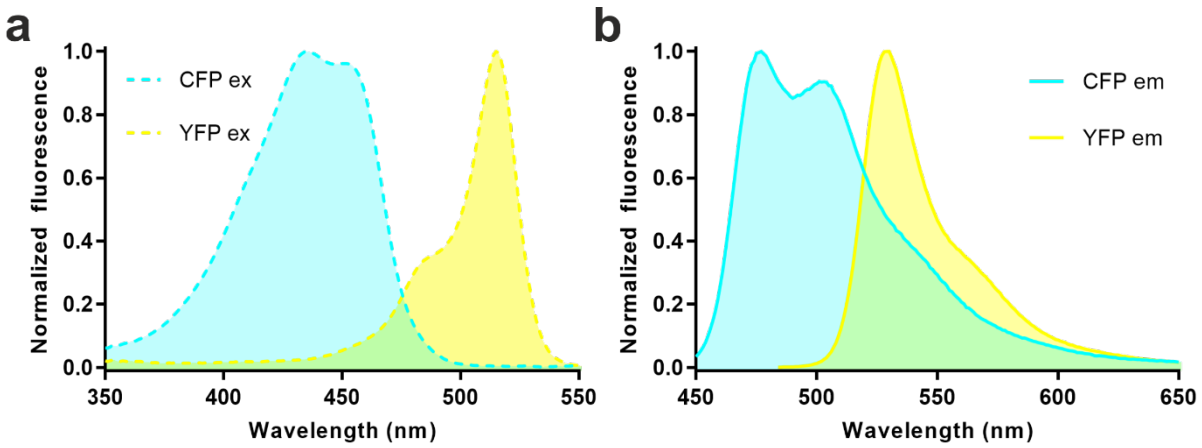

Figure 13: Direct excitation and bleed-through
(a), Overlap of CFP and YFP excitation spectra, showing the common excitation wavelength range (green area). In such pairs it can be advantageous (if autofluorescence of the cellular background is negligible) to excite left (at shorter wavelengths) from the CFP excitation peek, minimizing direct acceptor excitation. (b), Overlap of CFP and YFP emission spectra (green area) to exemplify the extent of donor bleed-through into YFP emission channels at given wavelengths.

Apart from ratiometric measurements, FRET gained popularity in several important microscopy techniques such as acceptor photobleaching (FRET-AB), fluorescence lifetime imaging microscopy (FLIM) or fluorescence polarization imaging.

FRET-AB is a relatively simple way to measure FRET-efficiencies (**Figure 14**). If FRET between two fluorophores occurs, the selective destruction of the acceptor by photobleaching causes that the energy, which supplies the acceptor, remains at the donor and therefore increases its fluorescence intensity. FRET-efficiencies can be calculated by subtracting the donor intensity (in the presence of the acceptor) from its intensity after acceptor photobleaching and normalizing this value to the donor intensity after bleaching (see also Formula $\mathrm{FRET}\ \ efficiency = \frac{\mathrm{Donor_{post}\text{-}Donor_{pre}}}{\mathrm{Donor_{post}}}$ (10) in method section)[88].

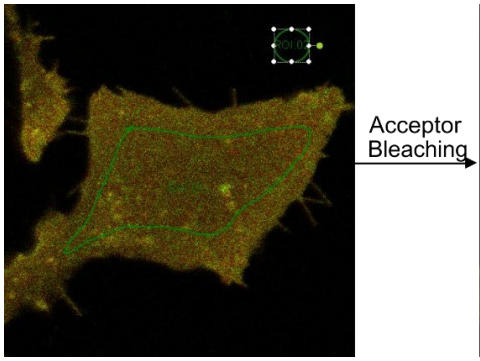

SNAP-CD28	ROI.01	ROI.02
Donor Pre	44.02	0.58
Donor Post	56.01	0.54
Acceptor Pre	111.3	0.94
Acceptor Post	46.32	0.88
Efficiency	0.2141	0

Figure 14: FRET- AB example
Example of a confocal based FRET- AB experiment. Cells are labelled to an equimolar extent with donor (green) and acceptor (red) dye. Bleaching of the acceptor causes an increase of the donor's intensity and reveals a FRET-efficiency of ≈ 21 %. (ROI.01 = Cell; ROI.02 = Background)

FLIM is conceptionally related to FRET-AB, since it also measures FRET by evaluating the influence of donor quenching by the acceptor. In contrast to an increase of donor intensity, such measurements rely on the fluorescence lifetime after donor excitation. Fluorescence lifetime (which is of nanoseconds) of a donor decays faster if an acceptor demands FRET mediated energy from it. The faster decay of a donor's fluorescence lifetime gives a quite reliable estimate of the FRET-efficiency, and is less artifact prone, since just the single parameter of donor lifetime needs to be monitored[89].

Fluorescence polarization imaging enables a special type of FRET measurements, which are relying on the use of the same species of fluorophore for the donor as well as the acceptor and are known as HomoFRET[90]. In this case the excitation light is linearly polarized and selectively excites fluorophores with dipoles in similar orientation. The loss of polarized light in the emission channel occurs mainly due to rotation of the fluorophore and FRET to fluorophores in differing dipole orientation. Due to the large molecular size of fluorescent proteins and the use of short time intervals in these measurements the impact on depolarization by rotation can be minimized, resulting in depolarization occurring dominantly through FRET.

A methodological modification of FRET measurements, which also relies on resonance energy transfer, (RET) is BRET (bioluminescence resonance energy transfer). In BRET experiments the donor is substituted by a luciferase, catalyzing the oxidation of a luciferin. Energy release by such reactions is usually leading to the emission of photons but can also be transferred via RET to a suitable acceptor fluorophore. An obvious advantage of such measurements is that no excitation light-source is required and therefore the above-mentioned acceptor direct excitation or photobleaching become insignificant[91].

Another RET based method, which also surpasses the issues of acceptor direct excitation and background fluorescence, is time resolved FRET (TR-FRET). Donor dyes with large Stokes shift and long luminescence lifetime (10^{-6}-10^{-3} s), such as complexes of the lanthanoids terbium or europium, are used for this approach. It enables measurements, shortly delayed, after the excitation light source is switched off, which are not impaired by the fast decaying background fluorescence or direct excitation.

FRET-based experiments with all their different modifications and methodologies offer tremendous potential to reveal molecular dynamics and signaling processses in living cellular systems[92]. The selection of the best FRET pair might not be generalizable and rather depend on the experimental procedure and question. Whereas among fluorescent proteins the combination of mNeonGreen-mRuby3 was reported to have the largest R_0 (65 Å) and showed a huge dynamic range in kinase FRET sensors[93], this pair might not be so powerful in other sensors. A recent comparative study of different acceptors and FRET pairs reported that mScarlet-I is a better overall acceptor[94] and blames the longer maturation time of mRuby3 for its lower performance. In imaging-based approaches combinations of chemical dyes with high photostability might be preferred and in simultaneous measurements of multiple FRET sensors, fluorophores with narrow spectra (but still sufficient spectral overlap) might be preferred[86]. The still growing interest and a broader usage of FRET techniques, will probably reveal further progress on the development of fluorophores and instruments within the next decades.

1.7. Labeling techniques

Protein labelling with fluorescent tracers is an essential requirement for studying cell biology with most optical methods. Since biological research gained through molecular cloning the ability to genetically manipulate DNA and thereby create fusion proteins of desired combinations, the basic requirement of protein labelling with fluorescent proteins or affinity tags has been achieved. Nevertheless, if genetic engineering is not an option because it is necessary to study the protein of interest in its native state, if expression should not be altered or if the genetic modification is too difficult without impairing the functional protein folding, successful protein labelling can be achieved using target specific antibodies or ligands conjugated with fluorescent probes.

1.7.1. Antibody labeling

Antibody labeling is usually done with antibodies, which are chemically modified with organic fluorophores or quantum dots after protein purification. This allows protein labeling with high photo-stability and superior signal to noise ratios. Most commonly the protein of interest is targeted with a primary antibody, whereas a secondary antibody binding to the first one is carrying the fluorescent probe[95]. For some proteins of interest (POI) also fluorescent primary antibodies are available, which allow a direct labeling of the POI, reducing time and effort of the labeling procedure. The major advantages of this labeling strategy are a broad availability of antibodies and that the protein itself stays apart from the attached antibodies in its native state. However, even though it is commonly advertised that antibodies are highly specific, there are convincing data for several POIs showing that selectivity of some antibodies is not sufficient for cellular labeling[96]. Especially if antibodies are used to address GPCRs, the experimental protocol should be well and thoroughly validated as pointed out by Michel et al.[97]. Another drawback is that for intracellular labeling cell permeabilization and fixation is required, abolishing the advantage of having the protein in its native state. For live cell assays, which rely on non-altered diffusion of the POI, it should also be considered that the molecular size of the antibody (≥ 150 kDa for a full IgG) may impair its mobility. In some specialized applications like super-resolution microscopy the size of the antibody might also reduce the localization precision for the POI, since the fluorophore might be a few nanometers away from the antibody’s binding site.

1.7.2. Labeling with fluorescent ligands

Particularly in the GPCR field an interesting labeling strategy with ongoing improvement in specificity and selectivity is the use of fluorescently tagged small molecule ligands (≤ 1,000 Da)[98], which bind with high affinity to the studied receptor[99]. Such ligands allow it to investigate the GPCR of interest in its native tissue at endogenous expression levels. In addition, some of them show superior signal to noise ratios and high photo-stability as required in single-molecule microscopy[100]. Whereas medicinal chemists made huge progress in subtype selectivity of the pharmacophoric units used in those ligands, there is still just a limited number of highly photo-stable fluorophores with negligible non-specific binding to cellular membranes or other proteins availible[101]. One drawback of this labeling strategy is that most of these ligands occupy the orthosteric binding pocket and thereby limit the options of further pharmacological experiments on the labelled receptor. Consequently, the development of "traceless affinity labeling[102]" is of high interest within the GPCR community. Recent works on this topic have successfully shown efficient labeling of GPCRs without impairing the receptors' functionality[103,104]. The strategy is based on delivering a fluorophore with a reactive linker group, ligand-assisted, in proximity to a suitable reaction partner. In the examples given here (Arttamangkul et al.[103]; Stoddart et al.[104]), the basic nitrogen of a lysine side-chain acts as a nucleophile, attacking a reactive carbonyl carbon atom within the linker. The nucleophilic substitution by the amino acid side-chain leads to a cleavage of the receptor's ligand, which can subsequently diffuse away from the orthosteric binding pocket and enables the binding of another ligand (**Figure 15**). A difficulty of this labeling technique might be the fine tuning of the linker's reactivity in a way that enough specific reactions with the receptor occur, while negligible amounts of unspecific reactions with other proteins or nucleophiles take place. If accomplished with satisfaction, this labeling technique will most probably be of strong interest for the development of further GPCR FRET sensors or FRET-based ligand binding experiments.

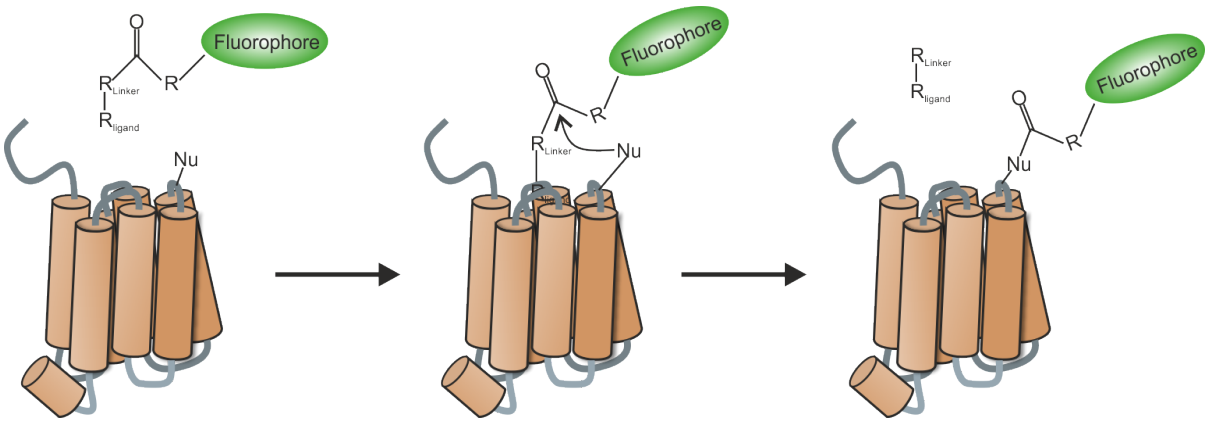

Figure 15: "Traceless affinity labeling" of GPCRs
The scheme visualizes the principle of the labeling technique. A nucleophilic side-chain residue of the GPCR attacks at the carboxylic carbon atom of the linker and replaces thereby the remaining linker- agonist part, which can afterwards diffuse out of the binding pocket and makes it available to binding of other GPCR ligands.

1.7.3. Fluorescent proteins

The use of fluorescent proteins is so far the most common and broadly used labeling technique in molecular biology. The first fluorescent proteins which became beneficial for biological research were phycobiliproteins extracted from cyanobacteria[105]. Due to their huge size (200 kDa) and the need to be supplied with bilin chromophores, their application in molecular biology is limited[95]. A breakthrough for biological imaging was the discovery and cloning of green fluorescent protein (GFP) derived from the jellyfish *Aequorea victoria*[106]. Molecular cloning allowed the generation of GFP fusion proteins, which do not need any other co-factor despite ubiquitous oxygen. A cyclization, dehydration and oxidation of three amino acid residues in the center of the GFP barrel creates the core- chromophore, the essential requirement for its fluorescence[107] (**Figure 16**). Since 1999, several other GFP homologues have been revealed in Anthozoa, Hydrozoa and Copepoda species, indicating the diverse evolutionary and spectral multiplicity of these proteins[108].

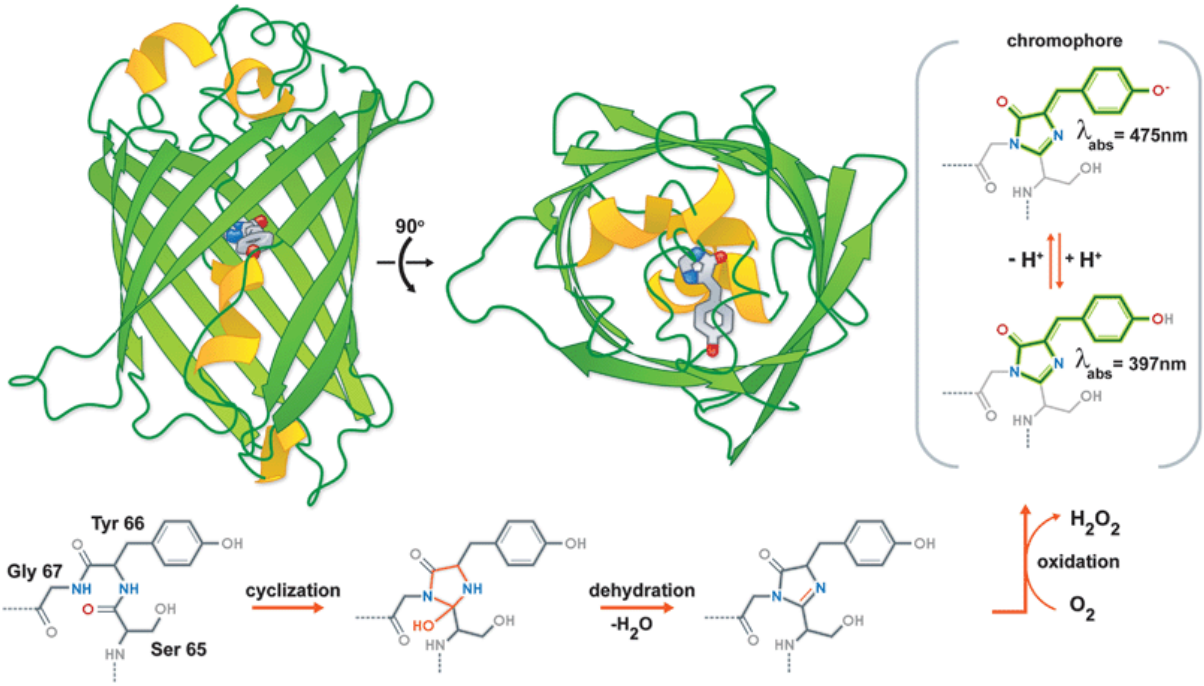

Figure 16: Protein and chromophore structure of GFP
Shown are 90° orthogonal views of the GFP barrel comprising 11 strands of beta-sheets as well as one alpha-helix crossing through the middle of this tertiary structure. The intrinsic chromophore within the center of this structure is formed by cyclization, dehydration and oxidation of S65, Y66 and G67 residues. Furthermore, excitation by blue light (370-400 nm) causes a phenomenon known as Excited State Proton Transfer (ESPT), which shifts without significant changes of the emission spectra the excitation peak towards 475 nm[109].
Figure was reproduced from Ref. (Frommer et al.)[110] with permission from The Royal Society of Chemistry.

Over the last decades, there has been an ongoing development of these GFP homologues due to many different mutagenesis approaches, yielding a variety of fluorescent proteins, reaching from ultraviolet to the infrared range of the electromagnetic spectrum. Whereas several fluorescent proteins were described to form oligomers, further mutagenesis studies led to fluorescent proteins with monomeric behavior, increased photo-stability and high quantum yied[95,106]. Lately also fluorescent proteins, which can be switched by light of a certain wavelength into specific emission states, have been developed. In 2004 Wiedenmann et al. published a fluorescent protein from the stony coral *Lobophyllia hemprichii* and named it EosFP[111]. It emits green fluorescence and can be photo-switched by UV-light to red emission. Additionally, other fluorescent proteins that can be photo-switched between several states such as Dreiklang, IrisFP and pcDronpa have been developed. They find their usage mainly in single-molecule localization microscopy (SMLM)-based super-resolution microscopy, where the activation of individual fluorophores enables the fit of individual point spread functions (PSF) and thereby the reconstruction of a super-resolved image (**1.8.1**). An obvious advantage of labeling with fluorescent proteins is the high labeling efficiency. Even though some fluorescent proteins need time for maturation, the labeling efficiency of the POI is theoretically close to 100 %. This is especially of advantage for the labeling of intracellular or even intranuclear cell structures, which are more difficult to label with antibodies or chemical fluorophores. However, if the experimental assay requires the use of endogenous protein in its native state or if very high photo-stability is needed, the labeling with fluorescent proteins reaches its limitations.

1.7.4. Peptide tags

Whereas peptide tags are classically understood as affinity sequences in protein purification from cell lysates, some of them can also serve for labeling of POIs with fluorescent entities. Peptide tags have the advantage that they are, in comparison to antibodies, fluorescent proteins or self-labeling enzymes, considerably smaller in size and therefore expected to alter protein function to a smaller extent[112]. One strategy of labeling with peptide tags is the use of a recognition sequence for an enzyme, which is involved in posttranslational modifications. The enzyme's substrate bound to a fluorescent dye serves in this case as a mediator to the POI. Examples for this principle are the biotin acceptor peptide (AP-tag) which can be labeled by biotin ligase[113], the LAP-tag which can be labeled by lipoic acid ligase[114] or the TMP-tag to be labeled by Escherichia coli dihydrofolate reductase[115]. Even though several groups showed convincing results of site-specific protein labeling with these methods in live cells, a major drawback are the complex and time-consuming labeling protocols, which require also the presence of the corresponding enzyme during labeling. A quite different strategy is the use of metal ion recognition tags such as a tetracysteine motif or His-tags. Tetracysteine motif ligands like FlAsH and ReAsH have been successfully applied for the labeling of GPCRs and enabled furthermore their usage in FRET measurements[116,117]. Successful extracellular GPCR labeling in live cells has also been shown for His-tags using fluorophores covalently bound to chelators which form a complex with Ni^{2+} or Zn^{2+} - ions[118]. The sequence of histidine side chains functions here as a second chelator, binding to these complexes and leading to labeling of the POI. Unfortunately, labeling with such metal ion recognition tags comes so far also with a non-negligible amount of non-specific labeling of other cysteine or histidine rich protein sequences[112]. This limits their usage for particularly sensitive approaches such as single-molecule microscopy in living cells. Peptide sequences, which rely on peptide-peptide interactions such as coiled-coil peptides[119,120] , leucine zipper tags[121] or even split proteins like split inteins[122] may be able to overcome the problem of non-specific binding and some might become valuable for single-molecule tracking[123]. A disadvantage here can be the peptide stability and thereby related the labeling efficiency as well as the need of cross-linking reactions in some labeling protocols[112]. Furthermore, the expensive synthesis of peptides covalently connected to fluorophores limits so far a broader use of these techniques.

1.7.4.1. SNAP-tag

In 2003 it was shown that the human DNA repair protein O^6-alkylguanine-DNA alkyltransferase (hAGT), can be used for fast, selective and covalent labeling of POIs[124]. The hAGT irreversibly transfers an alkyl group from its substrate (O^6-alkylguanine-DNA) to one of its cysteine residues (**Figure 17**a). Keppler et al. were able to prove that due to a low substrate specificity of hAGT also derivatives of O^6-benzylguanines with benzyl para substitution can serve as substrates[124](**Figure 17**b). Creating hAGT fusion proteins and the combination with fluorescently labeled benzylguanines enabled the opportunity to covalently tag POIs with a variety of different fluorophores. During the process of commercialization, the hAGT got the nowadays more usual name SNAP-tag, and numerous commercial and non-commercial substrates with different fluorophores, magnetic beads and other modifications have been developed. Protein engineering of the SNAP-tag led to another enzyme called “CLIP”, which has a higher selectivity for benzylcytosines, and allows in combination with the SNAP-tag a simultaneous labeling of two POIs in one sample[125]. Both enzymes have a size of 19.4 kDa, which is smaller than GFP variants, and they allow furthermore the labeling with chemical fluorophores of high photostability. However, among all the available SNAP-dyes just a few fluorophores show sufficient photostability, quantum yield and negligible unspecific labeling to other cellular structures[101]. A previous single-molecule study in our laboratory showed for extracellular GPCR labeling the best results by use of SNAP-Surface 549® dye[126], which is the reason for its usage also in the present study.

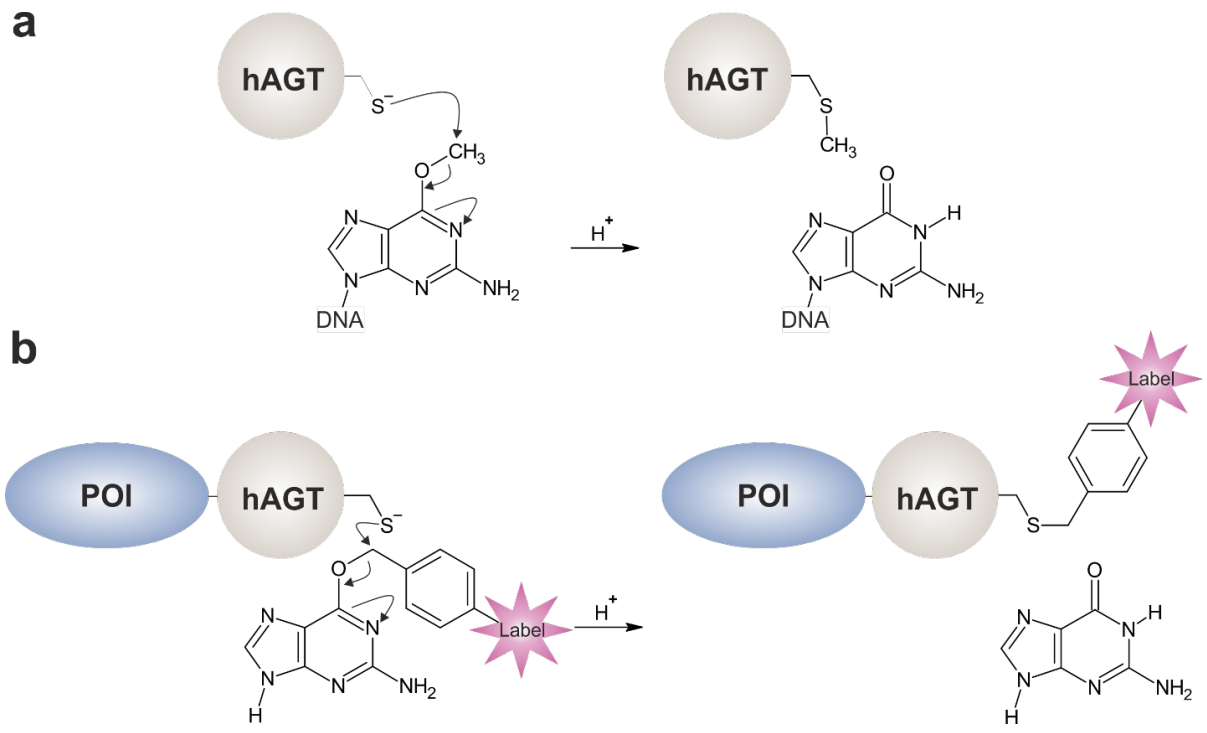

Figure 17: SNAP-tag and its working principle
(a), The O^6-alkylguanine-DNA alkyltransferase (hAGT) removes alkylations (here a methyl-group) from guanine bases by transfer to an as nucleophile serving cysteine residue within the enzyme (b), Fusion proteins of POIs and hAGT can be labeled covalently using benzyl- para substituted benzylguanines, based on the mechanism described in (a).
Material adapted with permission from: 'Keppler et a., A general method for the covalent labeling of fusion proteins with small molecules in vivo, Nature Biotechnology, published [Dec 9, 2002], [Springer Nature]'

1.7.4.2. Halo-tag

Clarification of the haloalkane dehalogenase's working mechanism[127] allowed the industrial development of a 33KDa self-labeling protein, known as Halo-tag[128]. Insertion of the H272F mutation into haloalkane dehalogenase abolished the enzyme's ability for regeneration and leads thereby to an irreversible alkylation of D106[129](**Figure 18**). The Halo-tag is another self-labeling enzyme, which allows due to its entirely different working mechanism also a simultaneous labeling along with SNAP-tagged POIs in the same sample. In the present work it showed especially for labeling of intracellular actin structures along with extracellular receptor SNAP-labeling a superior specificity and negligible background. Similarly as for the SNAP-tag, a broad number of commercial and non-commercial labels have been developed. A slight disadvantage of the Halo-tag is its size, which might impair the diffusion behavior of mobile POIs. Therefore, I decided in the single-molecule part of this work to use it just for the labeling of rather immobile protein- structures such as actin.

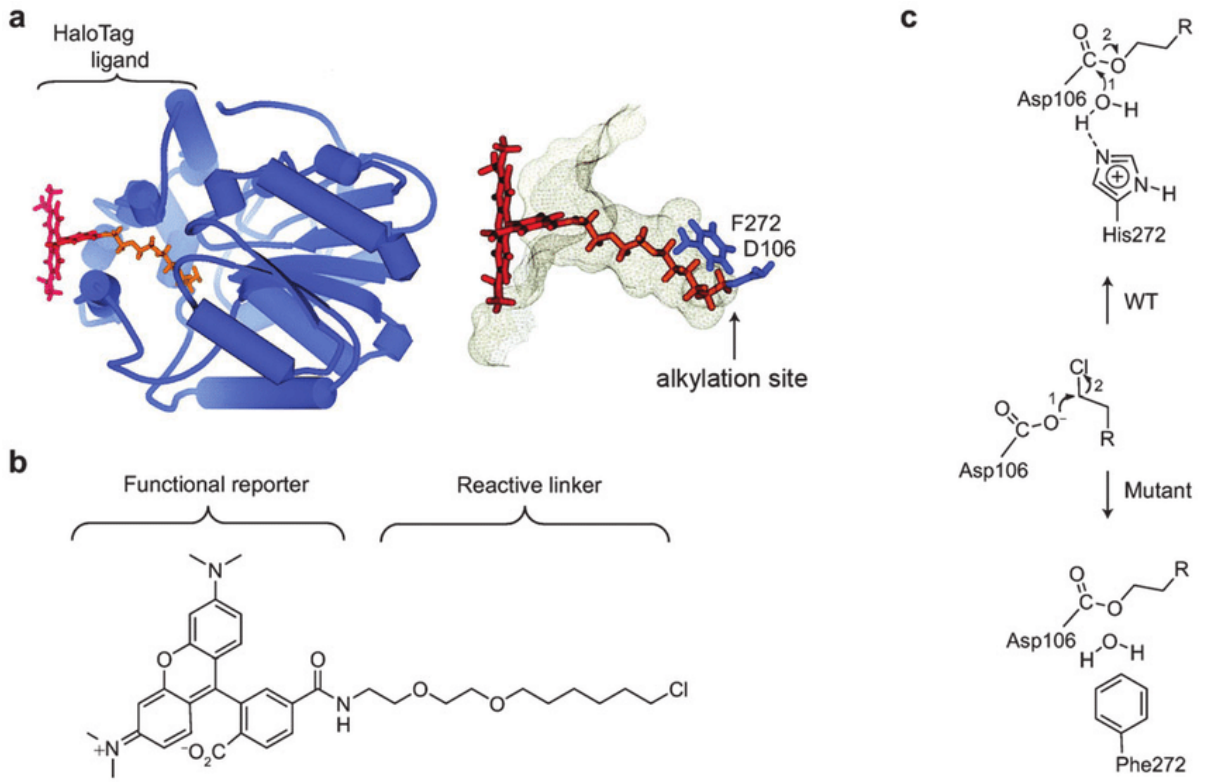

Figure 18: Halo-tag and its working principle
(a), Structure of the Halo-tag. The reactive linker matches selectively in the binding pocket of the enzyme and reaches out to the alkylation site (D106). (b), Halo-tag ligands are usually comprised of a fluorophore or other functional reporters, covalently bound to the reactive linker. (c), The H272F mutation of the haloalkane dehalogenase's abolishes the enzyme's ability for regeneration and enables thereby a persisting covalent labeling due to a nucleophilic attack of D106, leading to a displacement of the linker's chloride.
Figure was reproduced from Ref.[129] with permission from The Royal Society of Chemistry.

1.7.5. Luciferases

Luciferases are enzymes catalyzing the reaction of substrates, called luciferins, which cause upon oxidation the emission of light. A huge number of different luciferases with large chemical and biological diversity has been described over the last decades[130], but just a handful of those became popular for the usage in biological assays. Initially luciferases became, due to the low detection limit and a large dynamic range, popular for reporter gen assays. They raised further interest for usage in resonant energy transfer (RET) based assays by enabling such measurements in absence of an excitation light source, conclusively reducing photo-bleaching, cross talk and background. Classically such assays have been conducted using the combination of a 35 kDa Renilla luciferase (originating from the sea pansy *Renilla reniformis*) and a 27 kDa GFP variant[131]. Recent findings from our laboratory were able show a superior dynamic range in RET-based GPCR sensors by using a combination of a 19.1 kDa Luciferase (nanoLuc®) and Halo-tag, labelled with a specific commercial red-dye (Halo-tag ligand 618)[132]. NanoLuc® is a luciferase which originates from the deep-sea shrimp *Oplophorus gracilirostris.* It was in an industrial development further optimized and combined with an imidazopyrazinone substrate (furimazine), leading together to a ≈150-fold greater specific activity than Renilla luciferase in similarly constituted measurements[133]. I used this BRET-pair in the present work to measure intermolecular receptor interactions, β- arrestin2 recruitment and receptor internalization.

1.8. Fluorescence microscopy

Technical development and improvement of different microscopy methods for a broad range of applications makes fluorescence microscopy nowadays a very global term. The simplest setup among fluorescence microscopes is the epi-fluorescence microscope (**Figure 19a**). The essential parts of such a microscope are an excitation light-source, a dichroic mirror, an objective, suitable excitation and emission filters, a detector (e.g. a camera) and a stage which is holding the investigated sample. Since historically the objective was usually placed above the sample, the majority of today's microscopes, where the samples are placed above the objective, are called inverted or inverted stage microscopes. Microscope variants besides normal epi-fluorescence microscopes which were used in this work are a confocal microscope (**Figure 19b**) as well as a total internal reflection (TIRF)-microscope (**Figure 19c**).

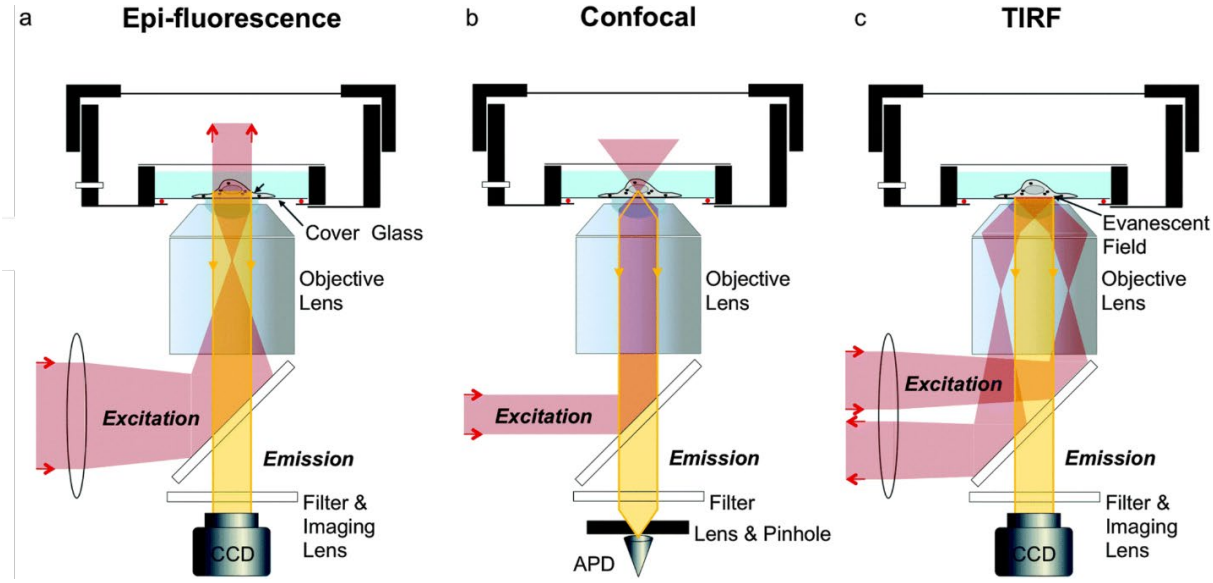

Figure 19: Microscope variants used in this work
(a), Epi-fluorescence microscope as used in this study for measurements of receptor activation with a cpGFP based GPCR sensor[134]. (b), Confocal microscope as used in this study for FRET-AB and molecular brightness measurements. (c), TIRF microscope as used for all single-molecule and super-resolution experiments in this study. Figure was reproduced from Ref. (Park et al.)[135] with permission from The Royal Society of Chemistry.

Standard fluorescence microscopy is diffraction limited and the optical resolution is therefore according to Ernst Abbe rather limited by the wavelength of the used light than by the magnification of the used objective[136]. Ernst Abbe approximated the diffraction limit as:

$$d = \frac{\lambda}{2n\,sin\theta} = \frac{\lambda}{2\,NA} \tag{3}$$

Where d is the resolvable distance between two objects, λ is the wavelength of the used light, n is the refractive index of the medium in which the object of interest is imaged (e.g. water, air) and θ is the half-angle subtended by the optical objective lens. $n\,sin\theta$ is also called numerical aperture (NA) and describes the capability of an optical element (objective) to focus light up to a certain angle θ (**Figure 20**), originating from the investigated sample[137].

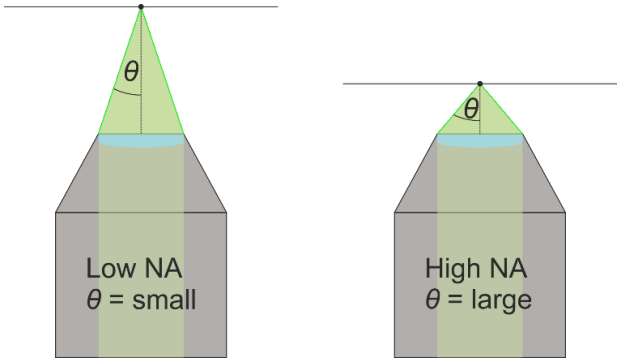

Figure 20: Numerical aperture of objectives *Objectives with a high numerical aperture are usually capable to collect more light from an investigated sample due to a larger angle θ. According to Abbe's approximation not just shorter wavelengths of light, but also higher NA objectives enable the discrimination of two objects with the distance d. Most commonly the higher NA correlates also with a higher magnification and a shorter working distance of the objective.*

Conventional fluorescence microscopy is nowadays a standard tool in many biological labs of several disciplines. Using fluorescent markers and fluorescence based biological sensors the minimal-invasive investigation of countless biological processes has been enabled. Ongoing research and new modifications of fluorescence microscopy were further able to find different ways to circumvent Abbe's still valid principle and achieved optical resolutions below the diffraction limit.

1.8.1. Single-molecule-total internal reflection fluorescence microscopy

TIRF microscopy is a microscopy technique which allows the selective excitation of fluorophores within proximity (≤ 100nm) of a solid surface by electromagnetic waves commonly known as evanescent field. The solid surface is usually a glass coverslip or slide and can, depending on the required optical quality also be made from quartz glass or even sapphire. Objective-based TIRF microscopy requires objectives with a high numerical aperture (NA > 1.4)[138] since high angles of incidence are necessary to achieve total internal reflection. In contrast to prism-based TIRF microscopes (not further discussed since not used in this work), the objective serves both for illumination and for the collection of emitted light (**Figure 19c**).

An evanescent field occurs when a light beam (usually a laser beam of a certain wavelength) approaches the interface between a higher and a lower refractive index material (e.g., glass/aqueous buffer) at an incidence angle greater than the critical angle[138]. The strength of the evanescent field decays exponentially with increasing distance from the reflective interface and causes that just fluorophores within close proximity to the reflective interface are excited (**Figure 21**). The small penetration depth of the evanescence field leads to a very low background fluorescence from out-of-focus planes and the resulting images have a high signal to noise ratio as necessary for the detection of single fluorescent molecules at the cell surface[138].

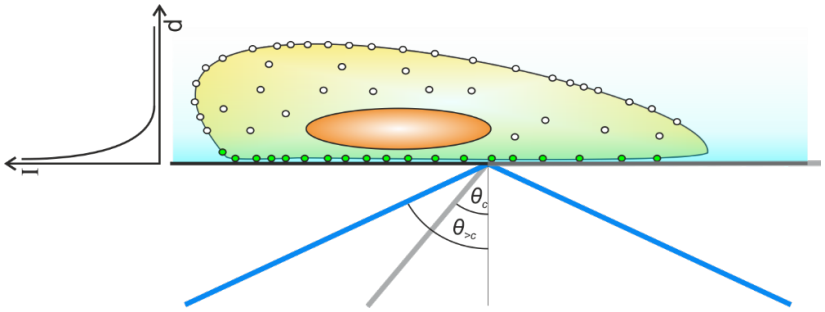

Figure 21: Evanescence field *The light beam (blue) arrives with a greater angle ($\theta_{>c}$) than the critical angle (grey; θ_c), becomes reflected and produces thereby an evanescent field. The intensity (I) of the evanescent field decays exponentially and causes thereby an exclusive excitation of fluorophores in proximity of the reflective interface.*

The exponential decay of the evanescent field occurs according to:

$$I_z = I_0 e^{-z/d} \tag{4}$$

where I_z is the intensity at a distance z from the reflective interface I_0 and d is the decay constant:

$$d = \frac{\lambda_0}{4\pi\sqrt{n_1^2 \sin\theta_1 - n_2^2}} \tag{5}$$

λ_0 is the excitation wavelength, n_1 the refractive index of the cover glass, n_2 the refractive index of the sample/buffer solution and θ_1 is the angle of incidence.

To obtain images from single emitting fluorophores highly sensitive cameras are required such as electron multiplying charge coupled device (EMCCD) or scientific complementary metal-oxide-semiconductor (sCMOS) cameras. Whereas EMCCDs cameras with large chip sizes (16 µm/pixel) are still unbeaten for extremely low light applications, the recent developments of sCMOS cameras are getting very close to the performance of such EMCCD cameras but comprise further advantages such as a bigger field of view or faster sampling rates[139,140].

Single-molecule microscopy is diffraction limited and relies on the detection of point-spread functions (PSFs) of individual emitting fluorophores. The size of a PSF is by far larger than the emitting fluorophore itself and can be fitted by a Gaussian function to localize its center (**Figure 22**). For single-particle tracking on live cells the POI is labeled with a sufficiently photostable fluorophore, and a stack of cell images is recorded over time (movie). During image processing the PSFs for each individual frame are detected and the localizations are connected via a tracking algorithm. A simple example principle for this is the nearest neighborhood tracking, which connects localizations of one frame with the closest detected localization in the subsequent frame[141].

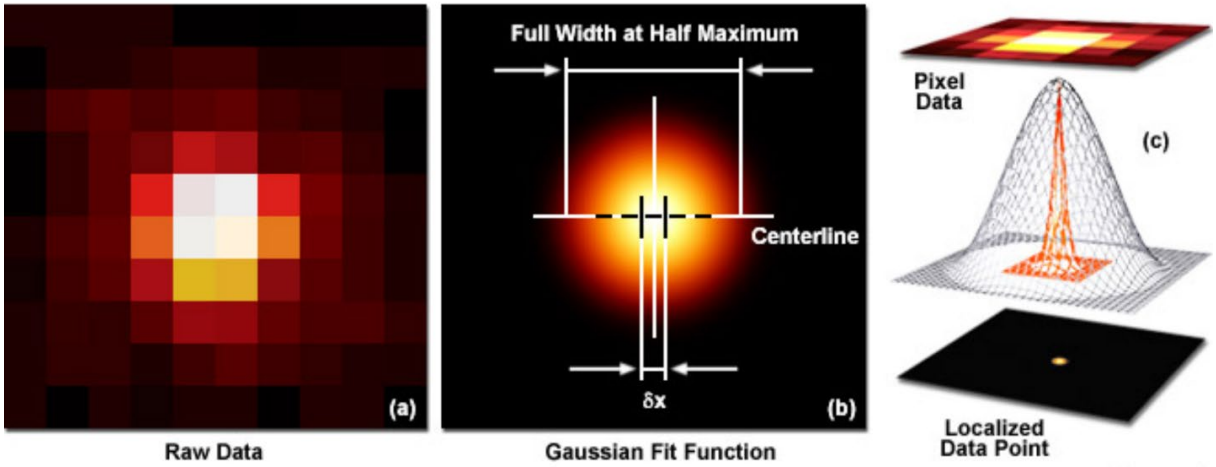

Figure 22: Fitting of single-molecule data to a Gaussian function
(a), Diffraction limited raw image data of an individual PSF (b), Two-dimensional Gaussian fit of the PSF to estimate its center (c), Illustration of the localization procedure leading to a datapoint localization with sub-pixel resolution. Adapted from: Carl Zeiss Microscopy Online Campus.
Copyright permitted on June 18, 2020. Retrieved June 18, 2020, from:
http://zeiss-campus.magnet.fsu.edu/articles/superresolution/palm/practicalaspects.html

For the detection of individual PSFs the density of emitting fluorophores needs to be low enough to avoid an overlap of multiple PSFs within one frame. Whereas intensity histograms of the detected particles can give information about the oligomeric constitution of the labeled POI, tracking can disclose information about diffusion behavior, dynamic interactions and areas with higher probability of residence.

1.8.2. Direct Stochastic Optical Reconstruction Microscopy (dSTORM)

Conventional fluorescence microscopy is, as mentioned above, diffraction limited and fails therefore in discrimination of two fluorophores if they are closer to each other than this limit. As described in the previous chapter, single-molecule localization of individual fluorophores can be done more precisely than their diffraction limited optical appearance by two-dimensional Gaussian fitting of individual PSFs. Single-molecule localization microscopy (SMLM)-based super resolution techniques take advantage of this by activating only a subpopulation of all available fluorophores within each imaging interval (frame). The collection of individual fluorophore localizations over a large series of images can then be used to assemble (reconstruct) an image which bypasses Abbe's diffraction limit (**Figure 23**). With this procedure, spatial resolution down to a few nanometers ("super-resolution microscopy") can be achieved, which permits a very precise insight to study cellular processes[142].

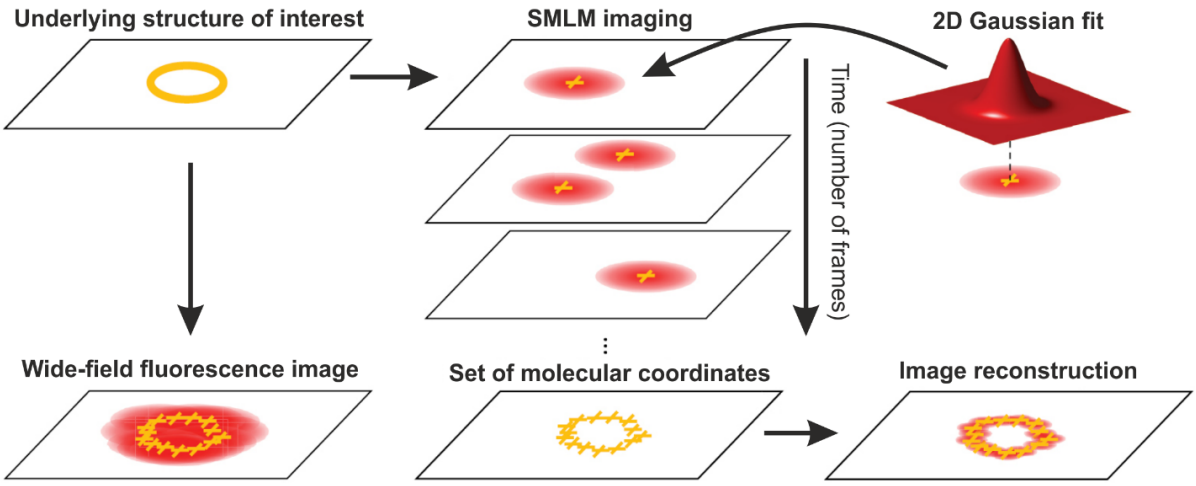

Figure 23: SMLM and image reconstruction
With standard wide-field fluorescence microscopy and simultaneous activation of all available fluorophores the structure of interest appears as a blurred object and cannot be identified. In SMLM imaging just a subset of fluorophores is active in each imaging frame and the density of emitters is kept low enough to capture PSFs with sufficient separation (max. 80% overlap of the PSFs airy disk[143]). Two-dimensional Gaussian fitting of the PSFs in all collected frames gives access to a set of molecular coordinates and enable the construction of a super-resolved image.
Edited adaption of Figure 2 from "From single-molecule spectroscopy to super-resolution imaging of the neuron: a review" Laine, R. et al (2016) Methods Appl. Fluoresc. ***4*** *022004 doi:10.1088/2050-6120/4/2/022004*

Whereas in SMLM approaches the method of analysis commonly relies on a similar principle, there have been different methods developed to assure the appearance of sufficiently separated single emitters in the individual recorded frames. Initial stochastic optical reconstruction microscopy (STORM) is based on the pair Cy3-Cy5 and relies on the recovery of Cy5 due to a FRET mediated reactivation by Cy3 (activator-dye)[144]. Almost simultaneously to the publication of STORM, others reported a SMLM based method, called photoactivated localization microscopy (PALM), which takes advantage of the controlled stepwise photo-activation and bleaching of suitable fluorescent proteins[145]. Whereas fluorescent proteins require a certain time for maturation, organic fluorophores are not impaired by this and several dyes can achieve, due to a higher photostability, also larger photon-yields[142]. Further advancement in SMLM was achieved due to the development of direct stochastic optical reconstruction

microscopy (dSTORM)[146]. In contrast to STORM usage of dSTORM does not require the presence of an activator-dye and uses conventional fluorescent dyes that can be reversibly cycled between fluorescent and dark states[146]. Usually the imaging buffers contain reducing agents and an oxygen scavenger system for the controlled modulation of fluorescent and dark states (**Figure 24**). If fluorophores enter after excitation, via intersystem crossing, the triplet state T_1 instead of emitting fluorescence, several fluorophores are able, in the presence of reducing agents with free thiol groups, to form relatively stable radical anions, representing a non-fluorescent dark state[147]. By reaction with molecular oxygen or with near-UV light excitation the fluorophores can be returned to the ground state S_0[148]. Some fluorophores form radical anions with high electron affinity and can therefore become further reduced to a non- fluorescent so called "leuco-form", which can also return to S_0 due to the reaction with oxygen[149]. Whereas transition to the dark state is controlled by the irradiation intensity and concentration of reducing agents, transition to the on state depends on thermal stability of the dark state, the oxygen concentration and can be further enhanced by near-UV light excitation[148]. Those parameters should be set in a way that the density fluorophores in the on state are kept low enough to assure single-molecule detection within the individual recorded frames.

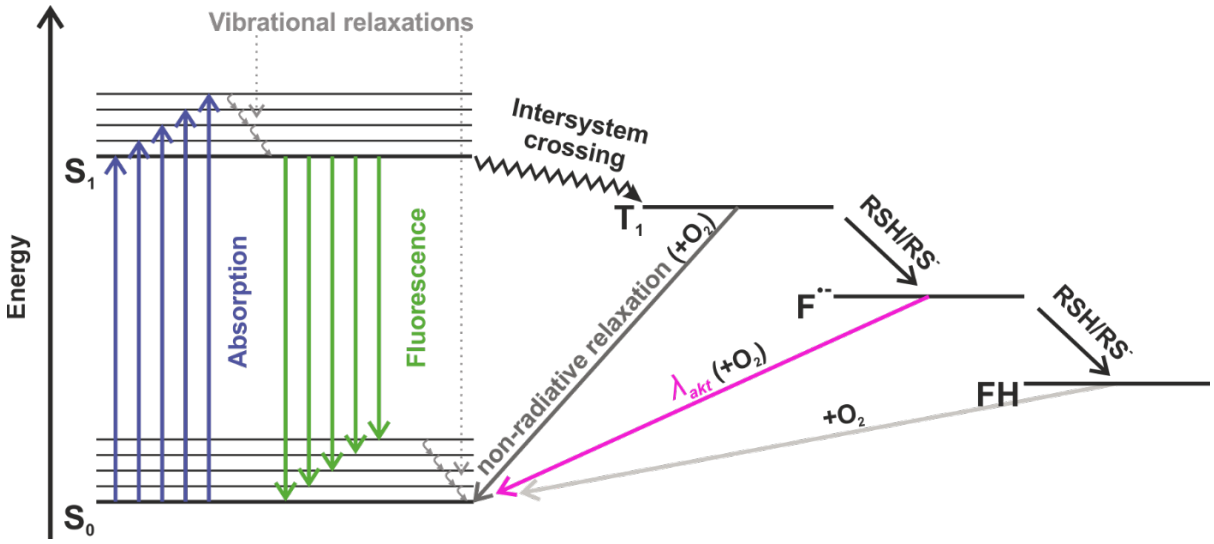

Figure 24: Simplified Jablonski diagram for redox-induced photo switching
Upon absorption of photons (excitation) electrons are lifted to S1 states. From there fluorophores can either emit fluorescence or depending on the intersystem crossing yield enter the long-lived triplet state T1. From there fluorophores can either react with molecular oxygen and return to S0 or react with free thiol groups, leading to a radical anion. Recovery to S0 can then either occur by excitation with near-UV light or by oxidization with molecular oxygen. Some fluorophores (e.g. ATTO 655) can be fully reduced to a so called "leuco-form", which can also by reaction with molecular oxygen return to S0.
Material adapted from Ref[148]: 'Endesfelder U., Heilemann M., Direct Stochastic Optical Reconstruction Microscopy (dSTORM)', In: Advanced Fluorescence Microscopy. Methods in Molecular Biology, published [Oct 30, 2014], [Springer Nature]'.

With SMLM methods resolutions down to ≈20 nm or even less can be achieved. Besides the above mentioned well controlled activation of individual fluorophores an appropriate drift control during the relatively long image acquisition is essential. For the same reason SMLM methods have reduced precision in live cells and should just be done on cellular structures with small or negligible movement such as actin. Besides for the reconstruction of super-resolved images, SMLM can be used for highly sensitive distance measurements[150], is a powerful tool for colocalization analysis[151], cluster analysis[152] and can give access to the stoichiometry of ternary protein complexes[153].

1.8.3. Confocal Microscopy

Laser scanning confocal microscopy (LCSM) is nowadays broadly distributed in biological research and many confocal microscopes are relatively easy to operate and therefore integral parts of many multiuser imaging facilities. Confocal microscopes are equipped with a pinhole, which rejects “out of focus” light emitted from the sample (**Figure 19b**), additionally this pinhole allows due to a more concise capturing of light theoretically a slight increase of resolution[154]. Practically this increase of resolution just starts to carry at very little pinhole sizes, which causes a reduction of signal, due to a lower amount of captured photons[155]. Image formation in confocal microscopes is conceptionally different from conventional widefield microscopes. The illumination is achieved by scanning of the sample with a focused laser-beam and the detector signal, caused by the emitted light, is used to reconstruct an image. Elimination of “out of focus” light by the pinhole size enables further the capturing of z-series of samples, which can be used to reconstruct three dimensional images and if repeated over time, it is even possible to obtain four dimensional movies of living biological samples[154]. Furthermore confocal microscopes are a valuable tool for measuring fluorescence recovery after photobleaching (FRAP)[156], FRET-AB experiments[157] and fluorescence fluctuation spectroscopy (FFS)-based methods[158].

1.8.3.1. Fluorescence fluctuation spectroscopy and molecular brightness

Fluorescence fluctuation spectroscopy measures the intensity variations of fluorescent particles, when passing through a small observational volume (typically on the order of one femtoliter) and characterizes, based on statistical analysis, their properties[159]. This observational volume can be created by a confocal microscope (**Figure 25a**), which provides the opportunity to conduct such measurements not just in solution but also in living cells or certain regions of interest (ROI). When a fluorescent particle or, as used in this work, a fluorescently labeled protein passes through the observational volume it creates a burst of photons, which is recorded by the detector (**Figure 25b**). The most prominent FFS approach is fluorescence correlation spectroscopy (FCS), which uses the autocorrelation of such fluctuations over time to obtain information such as the concentration, diffusion behavior or the size of the fluorescent molecules[159].

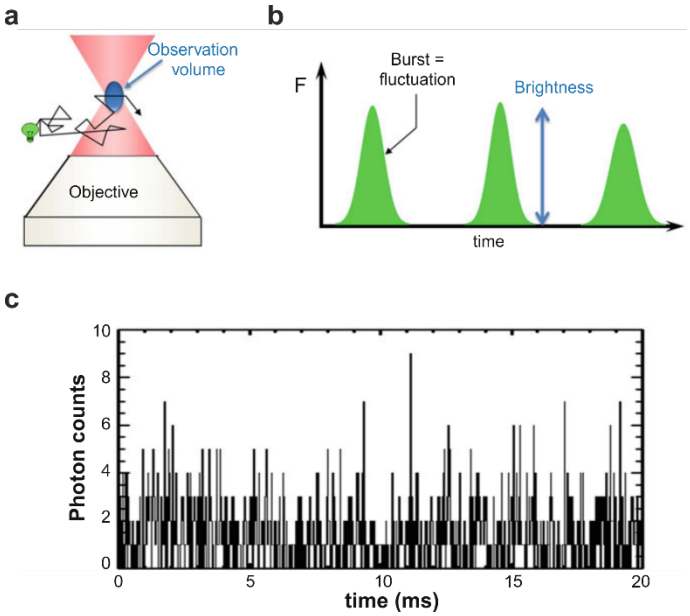

Figure 25: Fluorescence fluctuation spectroscopy
(a), Fluorescent particles can pass through an observational volume provided by a confocal microscope and cause a fluorescent signal. (b), Over time several particles create a photon burst (fluctuation). (c), Experimental data of an FFS measurement.
Adapted by permission from the European Biophysical Societies' Association (EBSA): Springer Nature, Fluorescence Fluctuation Spectroscopy, by Joachim D. Mueller [EBSA] (2013)

Molecular brightness measurements, give based on fluctuations, the average fluorescence intensity of a single-particle[159]. This can be used to investigate the oligomeric state of fluorescently labeled POIs such as GPCRs[160]. Notably, the usage of well proven controls is of high importance for such measurements. In the present work, two slightly different approaches were used to measure the molecular brightness of membrane proteins. What is called within this work (to facilitate terminology) “temporal brightness” relies as described above on measuring intensities and their variance of fluctuations over time. This photon count histogram-based methodology is more commonly also known as “number and brightness mapping”[161,162].

The brightness ε of a single-molecule and the number N of molecules is defined as:

$$\varepsilon = \frac{\sigma^2}{I} \tag{6}$$

$$N = \frac{I}{\frac{\sigma^2}{I}} = \frac{I^2}{\sigma^2} \tag{7}$$

where σ^2 is the variance of the intensity fluctuations and I the measured intensity.

The second method is called “spatial intensity distribution analysis” (SpIDA) and relies on the same conceptual principle with the difference that it compares the variance of intensities in a spatial manner[163]. This enables an analysis based on single images, which reduces bleaching-caused bias and can further be done with live cells as well as with fixed samples[163].

1.8.3.2. FRET acceptor bleaching (FRET-AB)

FRET-AB experiments are a useful tool to proof protein-protein interactions such as dimerization, but require also reliable monomeric and dimeric controls, to allow a comparison of the resulting FRET efficiencies. Furthermore, stable molar ratios of acceptor/donor are required, which was in the present work assured by labelling of the SNAP-tagged membrane proteins with equimolar concentrations of SNAP-dyes. Additionally, such experiments should be conducted over a broad range of expression levels to understand concentration dependencies of the obtained FRET-efficiencies. With regard to dimerization a linear increase of FRET-efficiencies is compared to a purely density driven non-specific interaction of the protomers[41]. In contrast suggests an exponential saturation the occurrence of specific interactions and allows an estimate of the dissociation constant[157]. FRET-AB experiments in this study were conducted at a confocal microscope as described in the methods section (2.2.8) and the principle of this measurements is discussed above in the FRET section (Page:**26** / **Figure 14**).

1.9. Biochemical tools to evaluate GPCR function and signaling

1.9.1. GPCR binding assays

To measure the effects of certain receptor modifications, e.g. insertion of tags or mutagenesis studies, or more commonly for the characterization of newly developed ligands it has for many years been of central importance in pharmacological research to use reliable ligand binding assays. Whereas radioligand binding assays have always been the classical reliable standard, nowadays several fluorescent ligand binding assays, based on BRET or TR-FRET have been developed and show also reliable results. However, they require manipulation of the receptor due to the insertion of a luciferase or SNAP-tag, respectively, and are not an option if the native receptor or a construct which should not be further modified (e.g. for structural research such as crystal structures or Cryo-EM) needs to be investigated.

Three basic types of binding assays are generally used: 1. Saturation binding, to determine the K_d of a new compound or a receptor modification and to evaluate the impact of non-specific binding. (**Figure 26a**) 2. Competition binding as an indirect assay if the investigated ligand is not available in a labelled form or a homologous competition is preferred for K_d estimation. (**Figure 26b**) 3. Kinetic assays, which are association or dissociation experiments to measure k_{on} or k_{off} respectively. (**Figure 26c**)

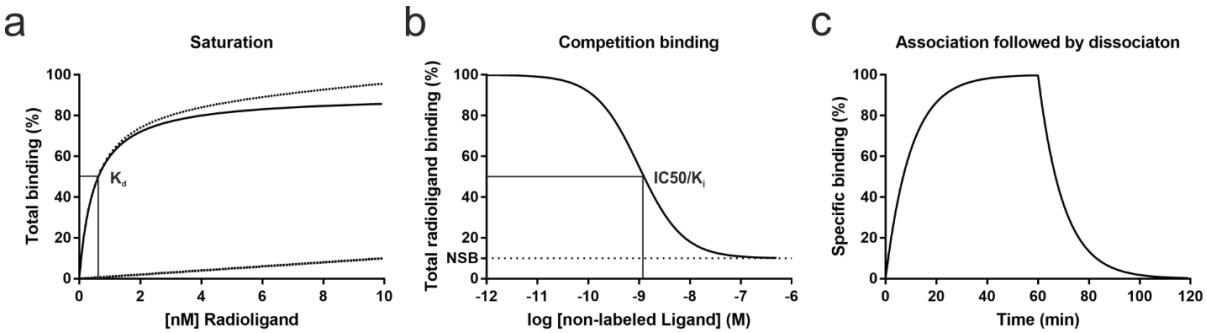

Figure 26: Types of radioligand binding assays
(a), Saturation binding experiment: The linear (squared) line indicates non-specific binding, the dotted line indicates total binding and the solid line is showing (after subtraction of non-specific binding) the resulting specific binding.

(b), Competition binding experiment with depletion of the radioligand, leading to an IC50-value that can be corrected according to the Cheng-Prusoff equation to obtain the K_i-value.
(c), Kinetics of an association-dissociation experiment. At minute 60 the competing ligand was added or the washout started to initiate the dissociation.

To obtain in competition experiments a K_i-value, the measured IC_{50}-value needs to be corrected according to the Cheng-Prusoff equation[164]:

$$K_i = \frac{IC50}{1+\frac{[R]}{K_d}} \tag{8}$$

where $[R]$ is the radioligand concentration and K_d the dissociation constant of the radioligand.

If competition experiments of a radiolabeled antagonist and a non-labeled agonist are conducted in the presence of G proteins, several GPCRs have been shown to expose a G protein-mediated high affinity binding, resulting in bi-phasic binding curves[8]. In this work, i did such experiments to validate that the constructs are not functionally impaired due to the insertion of a SNAP-tag and further to estimate high affinity binding based the G protein coupling of constitutively active and inactive receptor mutants.

1.9.2. Functional GPCR assays

As described above, today numerous RET-based biosensors are available to measure the downstream signaling of GPCRs and related signaling proteins. In this work of central importance was the activation of G_i proteins, the following reduction of cAMP levels due to the inhibition of the adenylyl cyclase, the recruitment of β-arrestins and the receptor internalization.

For G_i protein activation I used a FRET-based sensor, which is – in contrast to previous sensor versions – encoded on a single plasmid for all three G protein subunits and therefore assures that all the transfected cells are also expressing all three subunits. Additionally, the sensor concept is based on improved versions of CFP and YFP, namely it contains the Gαi-subunit tagged with mTurqouise2 and cp173Venus is fused to the $G\gamma_2$-subunit. This enables robust and reliable measurements due to a decrease of the YFP/CFP-ratio, based on βγ-dissociation[165].

To characterize the GPCR mutant's basal activity in this work, I measured apart from the G protein activation also their ability to influence cAMP signaling. To do so, I used an EPAC-based FRET sensor, named in the corresponding publication "H187", which is to my present knowledge the cAMP-FRET sensor with the largest dynamic range[166]. It allows, due to its superior dynamic range, also a robust measurement of G_i-signaling and the related lowering of cellular cAMP-levels.

For the recruitment of β-arrestin, I decided to use a nanoBRET based intermolecular sensor concept. To keep it simple, I measured the increase of BRET-ratios (Halotag-618 Ligand/nLuc) between C-terminally tagged μORs and Halo-tagged β-arrestins as described above (**39**).

The internalization assay in this work was a coincident discovery of a colleague (Hannes Schihada). We initially designed this construct comprising a 60 nm long rigid linker between two Halotags, which are tethered to the membrane, to measure the linker length itself using dSTORM. My colleague wanted to use this construct for bystander BRET with C-terminally tagged β_2AR and saw upon receptor activation within 20 minutes an impressive drop of the BRET-ratio. We assume that due to the long rigid linker, this construct cannot bend with the membrane curvature and can therefore not be co-internalized, which may explain its severe reduction of the BRET-ratio in contrast to a single membrane-tethered Halo-Tag (**Figure 27**).

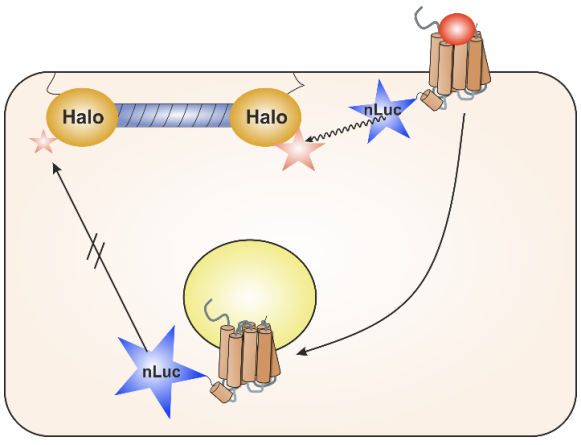

Figure 27: Internalization assay working hypothesis
The assay is based on BRET between the GPCR and the Halo- tags of the rigid 60 nm linker construct. Because of length and stiffness of the linker we assume that it is incompatible with the membrane curvature of endosomal internalization and remains thereby almost exclusively at the outer cell- membrane.

2. Materials and Methods

2.1. Materials

2.1.1. Materials for molecular cloning

NEB® 5-alpha Competent E. coli (High Efficiency) (#C2987H New England Biolabs)

2.1.2. Cell lines

Chinese Hamster Ovary cells (CHO)-K1 cells (ATCC)
Human Embryonic Kidney (HEK)-293 AD cells (Sigma)

2.1.3. Cell culture media and additives

Dulbecco's modified Eagle's medium F12 mixture, phenol red free (DMEM-F12) (#21041-033 Gibco)
Dulbecco's modified Eagle's medium (DMEM) (#21969-035 Gibco)
L-Glutamine (200 mM) (#25030-081 Gibco)
Fetal bovine serum (FBS) (#S0115 Biochrom AG)
Penicillin/Streptomycin (#P4333 Sigma-Aldrich)
Trypsin / EDTA solution (P10-023100 PAN Biotech)

2.1.4. Plasmids

Encoding transcript	Vector	Origin
Murine μ-opioid receptor (μOR)	pcDNA3.0(+)	Institute of Pharmacology Würzburg
SNAP-μOR	pcDNA3.0(+)	This work (Ulrike Zabel)
SNAP-μOR (T279K)	pcDNA3.0(+)	This work (Jan Möller)
SNAP-μOR (T279D)	pcDNA3.0(+)	This work (Ulrike Zabel)
SNAP-μOR (11S/T-A mutant)	pcDNA3.1(+)	Gene synthesis (Genscript)
SNAP-μOR (T279K-11S/T-A mutant)	pcDNA3.1(+)	This work (Jan Möller)
SNAP-β1AR	pcDNA3.0(+)	Institute of Pharmacology Würzburg
SNAP-CD28	pcDNA3.0(+)	This work (Ulrike Zabel)
μOR-mYFP	pcDNA3.0(+)	This work (Ulrike Zabel)
β1AR-mYFP	pcDNA3.0(+)	This work (Ulrike Zabel)
CD28-mYFP	pcDNA3.0(+)	This work (Ulrike Zabel)
Lifeact7-Halo	pcDNA3.1(+)	Gene synthesis (Genscript)
sigma2-EGFP	pEGFP-N1	Addgene (Plasmid #53610)
sigma2-mNeonGreen	pcDNA3.0(+)	This work (Jan Möller)
$G_{\alpha i2}$ FRET sensor (Gβ-2A-$_{cp173}$Venus-$G\gamma_2$-IRES-$G\alpha_{i2}$-mTurquoise2-Δ9)	Customized Vector	J. Goedhart (University of Amsterdam, NL)
H187 cAMP sensor (mTurq2-$_{\Delta}$DEPCD(Q270E)-$_{tdcp}$Venus EPAC-S^{H187})	Customized Vector	K. Jalink (The Netherlands Cancer Institute, Amsterdam, NL)

2.1.5. Transfection reagents

Effectene Transfection Reagent (#301427 QIAGEN)

Lipofectamine 2000 Transfection Reagent (#11668027 ThermoFisher Scientific)

Opti-MEM™ Reduced Serum Medium, no phenol red (#11058021 ThermoFisher Scientific)

2.1.6. Labeling reagents

SNAP-Surface® 549 (#S9112S New England Biolabs)

SNAP-Surface® Alexa Fluor® 647 (#S9136S New England Biolabs)

Halo-JF646 (Gift from Luke Lavis, Janelia Research Campus, Ashburn, Virginia)

2.1.7. TIRF- microscope

The microscopes essential parts are summarized in the following depiction, followed by a list of incorporated parts and devices.

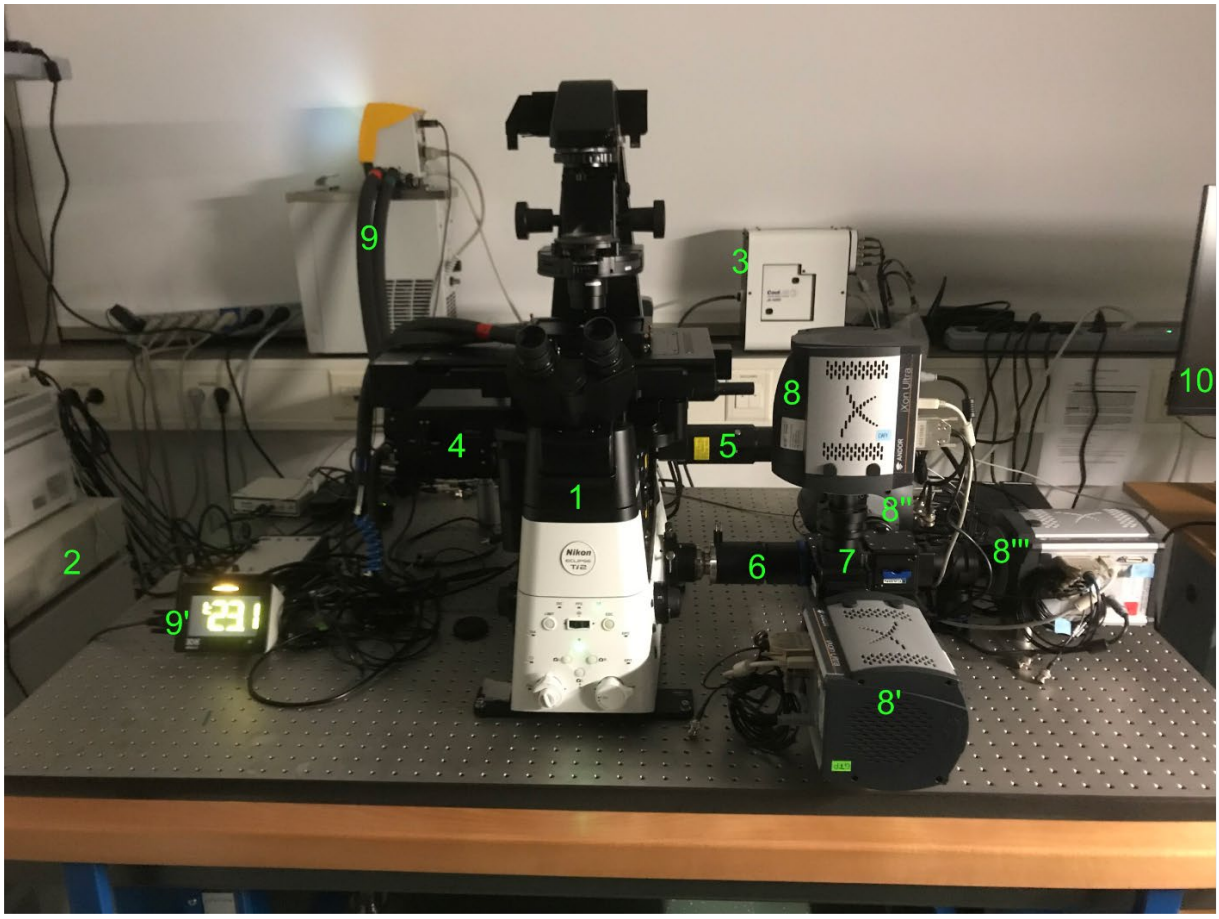

Figure 28: TIRF-microscope and its components
1) Microscope body (Nikon ECLIPSE Ti2)
2) Lightsource 1: Laserbox containing 405 nm, 488 nm, 561 nm, 647 nm wavelength Laser-diodes (Nikon)
3) Lightsource 2: LED-based light source with 16 different wavelengths reaching from 405 nm – 770 nm (CoolLED)
4) N-STORM module to control laser emission, angle, illumination field and intensity fine-adjustment (Nikon)
5) Manual TIRF module for angle control in multiple color imaging with different layers/ penetration-depths (Nikon)
6) Extension Tube connected to optical beam-splitter (Twincam, Acal BFi)
7) Combination of three Twincams to divide the emission signal in 4 different wavelengths (Acal BFi)
8) 4 iXon Ultra 897 EMCCD cameras (Andor) with filter sets for (8=DAPI, 8'=GFP, 8''=Cy3, 8'''=Cy5)
9) Temperature control unit (Okolab) with control display (9')
10) Computer system for control and acquisition of microscope data (Dell)

Other microscope features:

Objectives:

CFI Apochromat TIRF 60x Oil/ NA:1.49/ WD:0.13 (Nikon)
CFI HP Plan Apochromat TIRF 100x Oil / NA:1.49/ WD:0.12 (Nikon)

Microscope body configuration:

TI2-N-NDA-P Perfect Focus System (Nikon)
TI2-F-FLT-E motorized filter-revolver (Nikon)
QuadLine rejectionband (ZET405/488/561/647) (AHF)

Emission filters/dichroic mirrors:

ET Bandpass 450/50 (Filter) (AHF)
ET Bandpass 525/50 (Filter) (AHF)
H Bandpass 595/50 (Filter) (AHF)
ET Bandpass 700/75 (Filter) (AHF)
H 488 LPXR (Dichroic mirror) (AHF)
H 560 LPXR (Dichroic mirror) (AHF)
H 643 LPXR (Dichroic mirror) (AHF)

Software:

NIS-Elements -Advanced Research (Nikon)

2.1.8. Other microscopes used in this study:

SP5 confocal laser scanning microscope equipped with an argon laser-box (Leica)
SP8 confocal laser scanning microscope equipped with a white-light laser (Leica)

2.1.9. Microscope equipment

Attofluor™ cell chamber for 25 mm coverslips (#A7816 Invitrogen)
25 mm coverslips round (#631-1583 VWR)

2.1.10. Platereader & equipment

Synergy Neo2 platereader with quad-monochromator module and dual-PMT detection (#NEO2M Biotek)
Injection system with 2-channel dispenser (#8040030 Biotek)
NanoBRET-Filtercube: EM 450/50, 610LP / DM 550 (#1035074 Biotek)

2.1.11. Radioligand-Binding

Mach III Cell Harvester 96 (Tomtec)
[15,16-^{3}H]- Diprenorphine (#NET1121250UC PerkinElmer)

2.1.12. Buffer Solutions

dSTORM Imaging Buffers:

For fixed cells: 790 µL Buffer B + 200 µL MEA (mercaptoethylamine) Stock + 10 µL GLOX Stock
For living cells: 990 µL Buffer F + 10 µL GLOX Stock

Buffer A: 10 mM TRIS (pH=8) + 50 mM NaCl
Buffer B: 50 mM TRIS (pH=8) + 10 mM NaCl + 10 % glucose
Buffer F: DMEM-F12 Medium + 9.6 % glucose
MEA Stock: 1M MEA (77mg MEA + 1.0 mL 0.25 N HCl)
GLOX Stock: 56 mg/mL Glucose Oxidase + 3.4 mg/mL Catalase in Buffer A

Dulbecco's phosphate buffered saline (DPBS) (#14190-094 Gibco)
Hanks' balanced salt solution (HBSS) (#H9269 Sigma)

2.1.13. Other reagents/Kits:

Plasmid Plus Midi Kit (# 12945 QIAGEN)
QIAprep® Spin Miniprep Kit (#27106 QIAGEN)
NEB 5-alpha competent E. coli (#C2987U New England Biolabs)
SOC Outgrowth Medium (#B9020S New England Biolabs)
LB-medium (selfmade - 10 g/L peptone, 5 g/L yeast extract, 10 g/L NaCl)
LB-agar plates (selfmade - LB- medium and 15 g/L agar in petri dishes)
Mercaptoethylamine (#30070 Sigma)
Glucose oxidase (#G2133 Sigma)
Catalase from bovine liver (#C40 Sigma)
TRIS hydrochloride (#10812846001 Sigma)
NaCl (#9265.1 Carl Roth)
Peptone (#68971 Sigma)
Yeast extract (#Y0375 Millipore)
Agar (#05040 Sigma)
Ampicillin (#A0166 Sigma)
Kanamycin sulfate (#60615 Sigma)
DMSO (#A994.2 Carl Roth)

2.2. Methods

2.2.1. Molecular biology

2.2.1.1. Molecular cloning

All plasmids used in the present work were either created by restriction-enzyme cloning or purchased through gene-synthesis (Genscript). Sequences were verified after plasmid preparation through Sanger sequencing (LGS genomics sequencing service).

2.2.1.2. Plasmid preparation

Bacterial transformation:

A tube with 50 µL competent E. coli (DH5-α NEB) stored at -80°C was thawed on ice for 10 minutes. After addition of 10 ng of plasmid DNA or 1 µL ligation reaction mixture the tube was kept on ice for another 30 minutes, heat-shocked at 42°C for 30 seconds and returned on ice for another 5 minutes. 950 µL SOC-medium was added to the mixture and incubated at 37°C for 45 minutes while assuring constant agitation (300 rpm). Meanwhile selection plates were prewarmed to 25°C. The mixture was then mixed thoroughly by flicking the tube and 50 µL were spread on a selection plate. After incubation at 37°C overnight the plates were checked for bacterial colonies.

Plasmid purification:

An overnight culture grown from a single bacterial colony in LB- medium, using the corresponding selection antibiotics, was pelleted by centrifugation at 6000 x g for 15 min at 4°C. For plasmid purification of retransformed plasmids, the Plasmid Plus Midi Kit (QIAGEN) was used according to manufacturer's protocol. For purification of plasmids from cloning reactions (to screen for successfully obtained constructs) bacterial colonies were purified using the QIAprep® Spin Miniprep Kit (QIAGEN) according to manufacturer's protocol.

2.2.2. Cell biology

2.2.2.1. Cell culture

All experiments in this work were performed with either transiently transfected CHO-K1 cells (ATCC) or transiently transfected HEK 293 cells (Sigma). CHO-K1 cells were cultured in Dulbecco's modified Eagle's medium (DMEM)-F12 (Gibco) supplemented with 10 % fetal calf serum (FCS) (Biochrome), 100 units/mL penicillin and 0.1 mg/mL streptomycin at 37°C with 5% CO_2. For experiments performed with transiently transfected HEK 293 cells (Sigma), HEK 293 cells were cultured in (DMEM) (PAN Biotech), supplemented with 4,5 g/L glucose, 2 mM L-glutamine 10 % FCS (Biochrome), 100 units/mL penicillin and 0.1 mg/mL streptomycin, at 37°C with 5% CO_2. To split cells, growth medium was removed by aspiration and cells were washed once with a 10mL of phosphate-buffered saline (PBS) (Sigma), followed by trypsinization for 1-2 minutes in 2mL of trypsin 0.05 %, EDTA 0.02 % (PAN Biotech) solution and resuspended in the desired amount of cell culture medium. Cells were routinely tested for mycoplasma infection using the MycoAlert Plus Mycoplasma Detection Kit (Lonza GmbH).

2.2.2.2. Transfection

For single-molecule experiments CHO-cells were seeded 24 hours before transfection. Transfection was done 4-6 hours before TIRF-imaging using Lipofectamine 2000 (Thermofisher). For each single well of a 6-well cell culture plate (Brand) 2µg of the desired DNA were diluted in 500µL Optimem (Thermofisher) and mixed with another dilution containing 6µL Lipofectamine 2000 transfection reagent in 500µL Optimem. After incubation at 25°C for 20 minutes this mixture (total= 1mL) was added to a single well of cell culture plate, containing 1mL of DMEM- F12 medium. After 4-6 hours expression levels were sufficient for single- molecule experiments and the medium got exchanged with new DMEM-F12 medium.

For nanoBRET®-based 96-well experiments (β-arrestin2 recruitment, receptor internalization assay, receptor/receptor interaction), CHO-K1 cells were transfected in 10 cm dishes using 10 µg DNA mixture, 30 µL Lipofectamine 2000 (Thermofisher), 5 mL Optimem and 5 mL DMEM-F12 medium (Gibco). This mixture was exchanged 5 hours after transfection with fresh DMEM-F12 cell culture medium (Gibco) to avoid cell- toxicity. 24 hours after transfection cells were washed once with PBS, trypsinized, resuspended in medium and seeded homogeneously in white 96 well plates (Brand) with a density of 40,000 cells/well.

In FRET-AB experiments cells were seeded on 25 mm coverslips 24 hours before transfection. After that cells were transfected with SNAP-tagged receptor-constructs by usage of Effectene® transfection reagent (QIAGEN). Per well 0.4 µg DNA, 3.2 µL Enhancer solution and 10 µL Effectene® Transfection Reagent were used. 24-48 hours after transfection cells were used for experiments.

To perform FRET assays in 96- well plates ($G\alpha_{i2}$- activation sensor[165]; H187 cAMP sensor[166]), 10 cm cell culture dishes with HEK293 cells at 60 % confluency were co-transfected with the desired receptor construct and one of the above mentioned FRET sensors using Effectene® Transfection Reagent (QIAGEN). Per 10 cm dish 2 µg DNA, 16 µL Enhancer solution and 50 µL Effectene® Transfection Reagent were used. 24 hours after transfection, cells were washed once with PBS, trypsinized, resuspended in DMEM cell culture medium and seeded homogeneously in black 96 well plates (Brand) with a density of 40,000 cells/well.

In Effectene® based transfections the above-mentioned DNA amounts were diluted in EC-buffer, supplied with the transfection-kit. After addition of enhancer the mixture was vortexed for 1 second and incubated at 25°C for 5 minutes. Subsequent addition of the Effectene® Transfection Reagent was followed by vortexing for 10 seconds. To allow transfection complex formation another incubation at 25°C for 10 minutes was followed. While complex formation was taking place, cell culture medium was aspirated, cells were washed once with PBS and new medium was added. Afterwards transfection mixture was added dropwise to the cells and dishes were gently swirled to assure uniform distribution.

Transfection for preparation of cell membranes was done in 15 cm cell culture dishes with a confluency of 50 %. Before transfection the medium was exchanged and 20mL fresh DMEM was added. Transfections were set up using 10 µg empty vector (pcDNA 3.0) mixed with 10 µg pcDNA3.0 encoding for the desired murine µ-opioid receptor construct in 450 µL milliQ water. Afterwards 50 µL of 2.5M

$CaCl_2$ solution was added and mixed well. To this mixture 500 µL of 2xBBS-buffer (pH 6.95) were added, vortexed and incubated for 20 minutes at 25°C. The mixture was added dropwise on the cell culture dishes and those were gently agitated until equal distribution was assured. Cells were kept for 48 hours in cell culture before harvesting. If cells were treated with PTX (Sigma), it was added 24 hours before harvesting at a concentration of 100 ng/mL.

2.2.2.3. Cell fixation

For dSTORM imaging experiments of individual receptors the cells were fixed using methanol. To do so, the samples were washed three times with PBS after labeling and methanol of -20°C was added. Subsequently the samples were kept in a -20°C refrigerator for 30 minutes. Afterwards they were washed 3 times with PBS of 4°C and kept in the fridge at 4°C in PBS until imaging.

2.2.3. TIRF Microscopy

All TIRF-imaging experiments were performed with transiently transfected CHO-K1 cells as described above. Transfected cells were labeled with 1 µM SNAP-Surface 549® Dye (New England Biolabs), diluted in DMEM-F12 medium, for 20 minutes followed by three times washing with fresh medium for 5 minutes to reduce unspecific binding of the dye[167]. For dSTORM imaging experiments of actin- fibers, the sample was co-transfected with a Lifeact-Halotag construct (Genscript) and labeled with Halo-JF-646 under the same conditions as the SNAP-dye. JF-646 Dye was a generous gift by Luke Lavis (Janelia). To image clathrin coated pits, the receptor constructs were co-transfected with adaptor protein 2, C-terminally tagged with mNeongreen (AP2-mNG). After labeling cells were washed once with PBS and taken for imaging to an Attofluor™ Cell Chamber (Invitrogen) in sterile filtered HBSS (Sigma). For single-molecule imaging, a TIRF illuminated Nikon Eclipse Ti2 microscope (Nikon) equipped with a 100X 1.49NA automated correction collar objective and 405, 488, 561, 647 nm laser diodes coupled via an automated N-Storm module and four iXon Ultra 897 EMCCD cameras (Andor) was used. A more detailed description of the microscope can be found in **Figure 28**. Objective and sample were kept at 20°C during imaging. The automated objective collar was on and hardware auto-focus activated. For simultaneous and fast image acquisition (below 30 ms) of all detected channels the cameras were used in crop-mode.

2.2.4. Single-molecule microscopy

The imaging of individual receptors on the cell surface as well as dSTORM imaging belong both to the term of “single- molecule microscopy”, since they are both based on imaging of individual fluorophores.

To obtain movies for single-particle tracking of SNAP-tagged receptors, live cells expressing the desired receptor constructs, were imaged after labelling with SNAP-Surface 549® Dye on the above described TIRF-microscope. For standard movies with a temporal resolution of 30 ms, the 561 nm laser-line was kept at low power (2% of 70mW) during search for suitable cells. For acquisition of 30 ms interval movies, laser-power was raised to 70% (of 70 mW) and movies of desired length were recorded. For fast acquisition with a temporal resolution down to 10 ms the laser power was raised to 100% (of 70 mW) and a motorized 2x magnifying lens was inserted in the excitation light path to focus the laser-power onto a smaller area. The SNAP-Surface 549® Dye was recorded in the Cy3-emission channel of the microscope as described above. If subsequent dSTORM imaging of actin was conducted, acquisition was continued under activation of the 647 nm laser line at 100% (125mW) for ≈ 6,000 further frames as previously mentioned (2.2.3). The SNAP- Surface Alexa Fluor 647® signal was recorded using the Cy5-emission channel.

For more precise dSTORM imaging of individual receptors as in (**Figure 58** - **Figure 62**), cells were labelled with SNAP-Alexa Fluor 647® (New England Biolabs) 6 h after transfection as described above and fixed with methanol. Signal was recorded using the Cy5-emission channel with activation of the 647 nm laser line at 100% (125mW) and addition of GLOX-buffer, for >10,000 frames or until loss of signal. dSTORM movies were afterwards processed and analyzed in Fiji[168] (ImageJ[169]) using the plugin Thunderstorm[170].

2.2.5. Single-particle tracking and image analysis

Image analysis of the obtained TIRF-movies was done by first cropping the image to the desired size, region and frame-number using Fiji[169]. Thereafter, the movie was loaded in the Matlab environment (Mathworks) using u-Track[171] and requested parameters (e.g. wavelength of used dye, pixel size, bit-depth of the camera) were adjusted according to imaging parameters. Spot-Detection, Tracking and Motion-Analysis modules were then applied and executed. The appearing result files and variables were then analyzed with regard to intensity distributions, diffusion analysis, bleaching kinetics and merge/split events of individual receptor tracks[29,126] and by application of a code written particularly for this purpose which is mentioned here under the term "Polytracker".

The diffusion analysis with u-Track was conducted based on:

$$MSD = 4Dt^{\alpha} \tag{9}$$

Here D is the diffusion coefficient, t is time and α is the anomalous diffusion exponent. The diffusion classes were defined based on previous results in other works of the lab[29,126]. This means that particles with D < 0.01 μm^2/s were assigned to the immobile fraction. For D ≥ 0.01 μm^2/s and α<0.75 tracks were defined as confined. Brownian motion was defined as D ≥ 0.01 μm^2/s and 0.75 ≤ α ≤ 1.25. Categorization as directed diffusion was defined by D ≥ 0.01 μm^2/s and α ≥ 1.25.

To quantify the actin crossing events, localizations of Thunderstorm-processed actin-images were multiplied with corresponding Thunderstorm-processed images of the receptor-channel (based on the 400 first frames, used for the single-particle tracking) (**Figure 29**). Due to this procedure, just cases in which localizations were found in both channels at the same position lead to a major signal amplification[172]. The maxima of the resulting product-images were detected and quantified using ImageJ, since those indicate simultaneous localizations in both images. To indicate the percentage of tracks overcoming actin-fibers, the number of all detected maxima was divided by the number of receptor-tracks detected in u-Track for the corresponding movie. For control purposes the product image was overlaid with the actin-image, highlighting areas with crossing events.

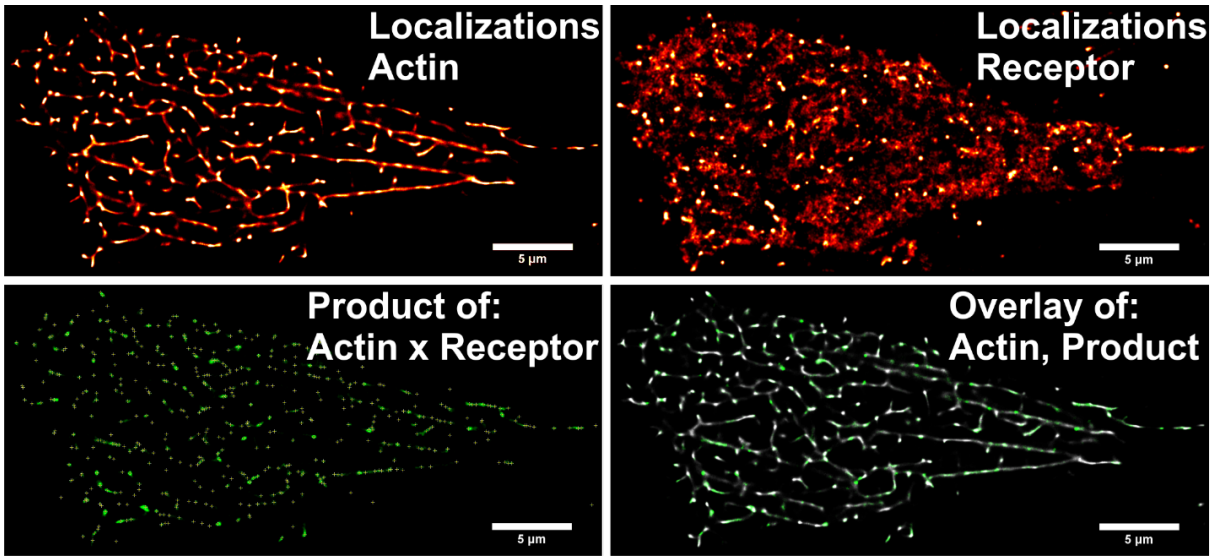

Figure 29: Quantification of actin crossing-events:
Upper panels: Thunderstorm processed localizations of the individual detection channels.
Lower panels: Product image of the localizations including maxima detection (left) and for quality control/illustration purposes the overlay of the product-image with actin (right).

2.2.6. Super-resolution microscopy for quantification of receptor organization

Single-molecule localization microscopy to quantify receptor organization and stoichiometry as conducted in (**Figure 60** - **Figure 62**) was performed by a colloborating lab (AG Heilemann, Institute of Physical and Theoretical Chemistry, Frankfurt am Main) using dSTORM on a home-built microscope with TIRF illumination[146]. Alexa Fluor 647® was excited using an LBX-638-180 laser (Oxxius) (0.56 kW/cm^2), photoswitching was induced by UV light ranging from 0 – 1.4 W/cm^2 using LBX-405-50-CSB-PP (Oxxius). Both laser lines were directed into a 100x oil immersion objective (PLAPO 100x TIRFM, NA ≥ 1.45), (Olympus), mounted on an inverted IX71 microscope (Olympus). Emission light passed an ET 700/75 filter (AHF) and was detected by an iXon Ultra X-10971 EMCCD camera (Andor). Imaging was performed with an exposure time of 30 ms, a pre-amplifier gain of 1 and an electron multiplying gain of 200. Image stacks between 25,000 and 50,000 frames were recorded until no more fluorescence signal was detected.

Super-resolved images were generated from the image-stacks using rapidSTORM[173] and LAMA[174]. Localizations of the same fluorophore that were detected in consecutive frames were linked to one localization. Quantitative analysis was performed by generating histograms of fluorescence emission events which were analyzed with theory-derived model functions as described previously[175] for fluorescent proteins and organic fluorophores[153]. Super-resolved spots which showed a brightness lower than 278 photons, an asymmetrical shape, or were in too close distance to other fluorescent clusters (less than 150 nm) were excluded from analysis.

2.2.7. Molecular brightness measurements

2.2.7.1. Temporal molecular brightness measurements

For temporal brightness imaging a SP5 confocal laser-scanning microscope (Leica) was used. The imaging mode was XYT and 50 frames were taken with a scanning speed of 400 Hz using the following parameters: pinhole-size: 67.93 µm/ zoom-factor: 30.3 X/ resolution 256x256 pixels. The Hybrid detector window was set between 525 and 600 nm. YFP-tagged constructs were imaged using a 514 nm argon laser at a power of 2.5 %. Data were analyzed using Igor Pro routine as described previously[176,177] . The brightness values were calculated based on the average of the brightness values from each pixel within the region of interest.

2.2.7.2. Spatial intensity distribution analysis

For spatial brightness imaging an SP8 confocal laser-scanning microscope (Leica) was used. Samples were SNAP-labeled with SNAP-Surface 549® dye as described above. Cells were imaged with a 40x / 1.25 NA oil immersion objective, using excitation with 560 nm line at 10 % (of a 1.5 mW white light laser), and a photon counting hybrid detector within 570-700nm emission band. Image size was 512x512 pixels format with 50nm pixel size, and pixel dwell time was 4.88 µs. Image analysis was performed applying the SpIDA function (one-population mode) using a MATLAB routine, as described previously[160,176]. The ROIs for image analysis using SpIDA were drawn carefully in free area selection mode, implemented to the original SpIDA routine, in order to avoid vesicles and inhomogeneously distributed membrane areas more effectively[32,33].

2.2.8. FRET acceptor photobleaching

Dual-color samples with SNAP-Surface 549® and SNAP-Surface Alexa Fluor 647® (New England Biolabs) were labeled as described above and placed into an Attofluor™ Cell Chamber (Fisher Scientific GmbH) and filled with 400µL HBSS. The chamber was mounted onto a SP8 confocal laser-scanning microscope (Leica). Cells were imaged using the Leica FRET-AB wizard with a HC PL APO CS2 40x / 1.3 NA oil immersion objective. A 1.5 mW white light laser was set to 85 % and a 560 nm laser line was used at 5 % power for donor imaging. For acceptor imaging a 647 nm laser line at 2 % was used and for the bleaching step power got increased to 50 % over 10 frames. 512 x 512 pixels images of the bottom cell membrane expressing SNAP-tagged receptor constructs were acquired with a hybrid detector in Standard mode. Emission of donor channel was recorded within 575-640 nm and acceptor channel was acquired between 658nm and 776nm. The zoom factor was set to 5.5 x resulting in a pixel-

size of 0.103 µm and the laser scanner speed was set to 400 Hz. There were at maximum 2 cells taken for analysis per image. FRET-efficiencies were calculated in the Leica FRET-AB wizard tool[178] according to:

$$FRET_{efficiency} = \frac{Donor_{post} - Donor_{pre}}{Donor_{post}} \quad (10)$$

Potential vesicles close to the cell surface were excluded from analysis by the drawing of the ROI.

2.2.9. Platereader FRET measurements

Cells transfected as described above were seeded in black 96-well plates (Brand). 24 hours later cells were washed once with 90 µL PBS/well, and 90 µL HBSS/well was added. After 5 minutes incubation at 37°C baseline measurement was conducted in a Neo2 plate reader (Biotek) using CFP/YFP filter-settings. Afterwards the desired dilution series with increasing concentrations of DAMGO was added (10 µL/well of a 10x concentration in HBSS) and the plate was measured again. The percent change in acceptor/donor-ratio was plotted against logarithmic concentrations of DAMGO using PRISM 7.0 and the “Dose-response Inhibition Fit” was applied.

2.2.10. Platereader BRET measurements

Cells transfected as described above were seeded into white 96-well plates (Brand). After 24 hours cells were labelled overnight (at least 16 hours) with Halotag 618 Ligand (Promega), a labeling dye which does not require a wash-out protocol. Therefore, the labeling is just performed by medium exchange with DMEM-F12 cell-culture medium containing a 1:1000 dilution of the Halotag 618 Ligand. Before measurement cells were washed twice with 90 µL PBS/well, and 90 µL HBSS/well was added containing a 1:1000 dilution of Nano-Glo-substrate (Promega). After 5 minutes of incubation at 37°C baseline measurement was conducted in a Neo2 plate reader (Biotek) using a nanoBRET filter-set (Biotek). Afterwards the desired dilution series with increasing concentrations of ligand was added (10 µL/well of a 10x concentration) and the plate was measured again. For BRET measurements between receptors the µOR was C-terminally tagged with nanoLuc (Promega) and the corresponding protomer C-terminally tagged with Halotag (Promega). For β-arrestin2 recruitment measurements the nanoLuc tagged µOR was co-transfected with Halo-tagged β-arrestin2. For the internalization measurement two Halotags, separated by a repetitive rigid linker sequence of approx. 60 nanometers, were targeted to the plasma membrane N-terminally using a Lyn -derived sequence (GCIKSKRKDK) and C-terminally using a farnesylation sequence (KKKSKTKCVIM). Also here the µOR was C-terminally tagged with nanoLuc. After measurement the percent change in acceptor/donor ratio was plotted against logarithmic concentrations of applied ligand using PRISM 7.0 and the “Dose-response Stimulation Fit” was applied.

2.2.11. Radioligand Binding

2.2.11.1. Membrane preparations for radioligand binding

Transfected HEK 293 cells from 15 cm dishes were grown until 90 % confluency and harvested in buffer (5mM TRIS, 2mM EDTA, pH 7.4) using a cell scratcher. Cells were spun down by 10 min centrifugation at 800xg. The resulting pellet was resuspended in 15mL phosphate-buffered saline containing 20mM HEPES and 10mM EDTA at pH 7.4. The following steps were all carried out at 4°C. Cells were resuspended and homogenized with two 15-second bursts of an Ultra-Turrax Homogenizer TP 18-10 (IKA). After 10 minutes centrifugation at 3,200rpm and 4°C (JA-17 rotor, Beckman Coulter GmbH, Krefeld, Germany) the supernatant was transferred to ultracentrifuge-tubes. Ultracentrifugation was performed at 37,000rpm and 4°C for 40 minutes (70 Ti rotor, Beckman Coulter GmbH, Krefeld, Germany). The pellet was resuspended in buffer (50 mM Tris, 100 mM NaCl, 3 mM $MgCl_2$, pH 7.4) and the ultracentrifugation step was repeated once. The resulting suspension was homogenized with a Dounce tissue grinder to ensure homogeneous dispersion. The product was transferred in aliquots and frozen using liquid nitrogen. Aliquots were stored at -80°C. Protein concentration was determined using a BCA-kit (Pierce BCA Protein Assay Kit, Life Technologies GmbH).

2.2.11.2. Binding experiments and analysis

A mixture of cell membranes (10 µg protein) and 0.3 nM [15,16-^{3}H]-diprenorphine (PerkinElmer) was incubated with increasing concentrations of DAMGO (Sigma) in a binding buffer (50 mM Tris, 100 mM NaCl, 3 mM $MgCl_2$, pH 7.4) on 96-well round bottom plates. Unspecific binding was determined with 10 µM naloxone (Tocris Bioscience, Bristol, UK). Binding reactions were incubated for 4 h at 25°C assuring constant agitation. Free radioligand was separated from bound fraction by fast filtration and 3 times washing with 4°C binding buffer on a 96-well filtermat (GF/C–Filtermat A, PerkinElmer) using a 96-well MachIII-Harvester (Tomtec Inc.). Radioligand activity was measured by scintillation counting with a melt-on MeltiLex scintillator (PerkinElmer). Competition binding data were fitted using the comparison of fit function of GraphPad PRISM 7.0. Selected comparison method was Akike's information criteria (AICc) and selected fits were "One site-Fit Ki" and "Two sites-Fit Ki".

2.2.11.3. Coding of the “Polytracker”

The polytracker software package was coded by a collaborator (Brendan Osberg, see acknowledgements) and streamlines the processing of receptor-tracking data obtained through u-Track. It is publicly available at: https://github.com/Blosberg/polytracker/

In addition to rendering position-vs-time data more easily accessible for individual tracks, the software also determines, for control purposes, additional metrics of the track state, such as densities and fluorescence intensities. In the case of oligomerization bonding. Lifetimes are inferred without any assumption as to the state of the track (i.e. monomer, dimer, etc.). Rather, for any merger event that is followed by a splitting event (ignoring concurrent events of other tracks) the intervening time is recorded. Ignoring potential higher-order biases (e.g. a trimer formation, and breaking apart through different bonds, or the undetected splitting of photo-bleached particles), the resulting histogram shows the distribution of bond lifetimes.

2.2.11.4. In silico simulations for measurement of random collision events

The in-silico simulations were conducted by a collaborator (Vikram Sunkara, see acknowledgements).

The diffusion trajectories were generated using the Reaction Diffusion Dynamics software package ReaDDy[179]. In ReaDDy, a square region was generated, and the prescribed number of particles were uniformly distributed over it. Then for a given diffusion rate, these particles were simulated forward undergoing pure diffusion and their positions were recorded at 10 millisecond intervals for a duration of 10 sec. The positions of the particles at each timepoint were then rendered using OpenCV (Python). The particle locations were projected onto an image which was 200 pixels by 200 pixels. For each timepoint, the corresponding particles were rendered as circles with a radius of 2 pixels. To simulate observational noise, white noise with a standard deviation of 15 % of the intensity of the particles was added to the image. Then, to blend the particle signals with the background noise, a Gaussian smoothing filter of 3 by 3 pixels was run over the image to imitate individual PSFs. In Fig. The particles undergoing confined and directed diffusion were modelled using different potential fields. Confined particles were modelled with a potential well. The depth of the well was calibrated to produce mean diffusion speeds matching the observed range of receptor diffusion. Directed particles were modelled with a concave potential field, with the gradient of the field giving the particles their directed characteristic. Like in the confined case, the height of the potential field of the directed particles was calibrated to produce matching diffusion speeds. The immobile particles were modelled with a very small diffusion coefficient ($D < 0.01\ \mu m^2/s$). For each simulation, the Brownian and immobile particles were positioned using a uniform random variable over the domain. The confined particles were initialized inside the potential well with uniform random perturbation. The directed particles were initialized near the peak of the potential field with uniform random perturbation. The diffusion coefficients and distribution of different diffusion classes were adapted to the ones obtained from real TIRF- movies and particle populations of 25, 50, 75, 100, 125, and 150 were generated. The simulations were repeated 20 times. The code and all the simulated movies for this study are available at: https://github.com/vikramsunkara/Receptor-PSF-Diffusion-Simulator.

2.2.11.5. Other methods or protocols

Coverslip cleaning:

For microscopy experiments coverslips were cleaned in a coverslip holder that assured separation of individual coverslips. The holder was placed in a beaker and filled up with chloroform until coverslips were covered. After one hour in a bath sonicator at 25°C the coverslips were dried and the sonification was repeated in 5 M NaOH solution. Afterwards the coverslips were transferred to a new beaker and washed three times with distilled water. Coverslips were stored until usage in a tube containing particle free filtered 96.5% ethanol.

Preparation of LB-medium / Agar plates:

The above-mentioned amounts of peptone, yeast and NaCl were dissolved in 1 L of distilled water and the pH-value was adjusted to 7.0 Afterwards the LB-medium was filled in glass bottles and autoclaved for 2 hours at 121°C using a pressure of 2 bars. For solid medium, used in selection plates, 15 g of agar were added before autoclaving. For agar plate generation solid LB-medium was melted in a microwave oven, mixed with the desired selection-antibiotic and poured into petri- dishes (20 mL per dish).

3. Results

3.1. The μ-opioid receptor is compartmentalized by actin fibers and gains mobility upon receptor activation

To localize and track individual μORs on the surface of living cells using TIRF-microscopy, a SNAP-tag[124] was fused N-terminally to receptors and labeling was done with SNAP-Surface 549® dye. For single-molecule experiments the constructs were transiently expressed in CHO-cells with post-transfection times between 4 and 6 hours to ensure a low expression level suitable for single-molecule detection (< 0.3 particles per μm^2).

Essentially complete labeling was obtained as described in (2.2.3) and as previously described[167]. Labeling conditions and efficiency were assessed with the help of a double-tagged control construct (**Figure 30a**), which – in addition to the N-terminal SNAP-tag – contains the photostable GFP variant mNeonGreen at the C-terminus.

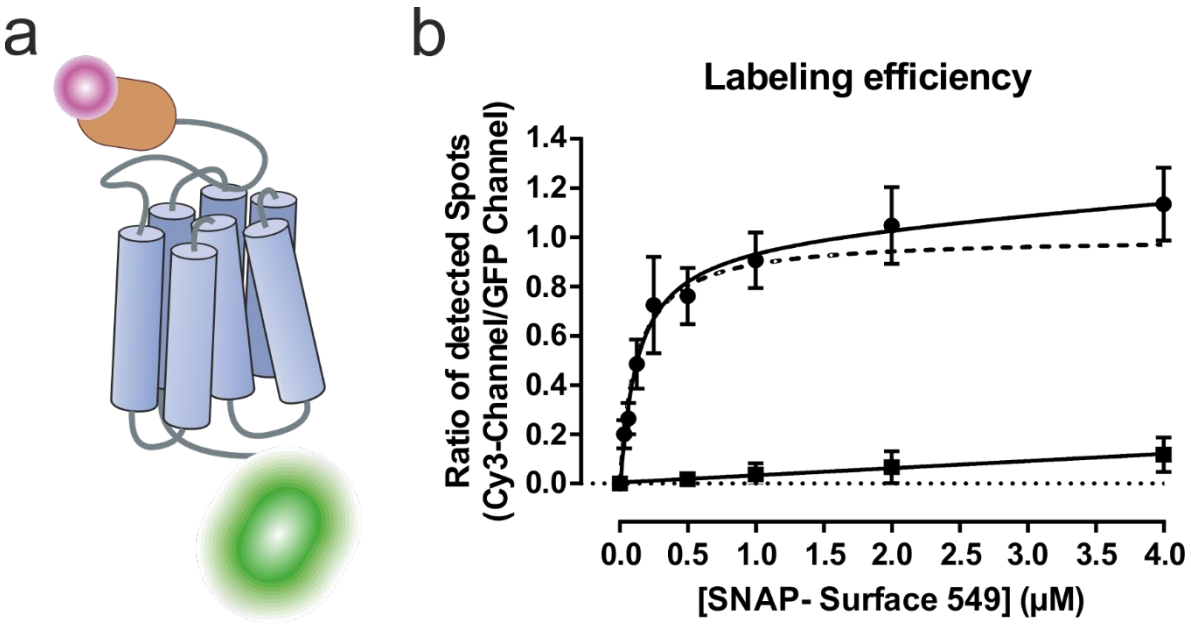

Figure 30: Labeling efficiency
a) Illustration of the control construct comprised of μOR, N-terminally labelled with SNAP-Surface 549® and C-terminally tagged with mNeongreen.
b) Plotted are ratios based on the number of detected molecules in each detection channel against the dye concentration used. Detection channels were controlled by a GFP filter for mNeonGreen and a Cy3-Filter for SNAP-Surface 549®. Dotted datapoints are total binding and squared datapoints are non-specific binding (evaluated by an exclusively C-terminally with mNeonGreen tagged receptor construct). The dashed line indicates specific binding of the dye, which is obtained by subtraction of non-specific binding from total binding. Data are mean ± SD. of n = 42 cells and n = 14 cells for specific binding and non-specific binding, respectively.

Co-localization of the two colors in both detection-channels showed that, using 1 µM SNAP-Surface 549® dye, essentially quantitative labeling (≥90 %) of the receptors' SNAP-tag with negligible non-specific labeling was achieved (**Figure 30b**;**Figure 31**). Higher concentrations of dye such as 4 µM are leading to less satisfactory results due to the contribution of non-specific labeling.

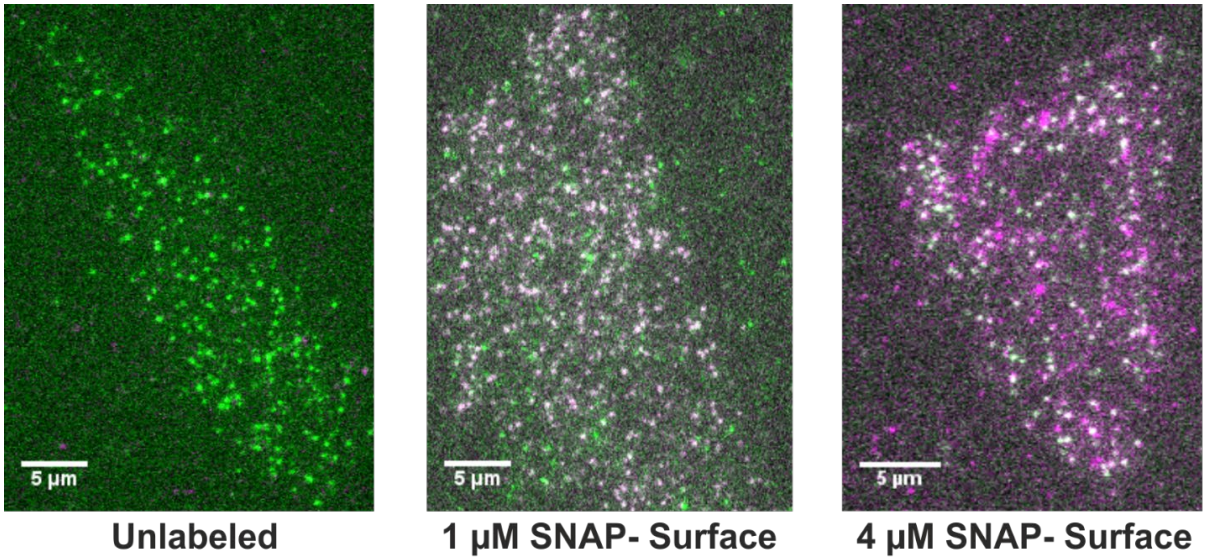

Figure 31: Dual-color TIRF-images of the µOR control-construct
Green corresponds to mNeongreen and magenta to SNAP-Surface 549® labelled receptors. Constructs carrying both labels appear due to the image overlay as white spots, while green spots represent receptors which are not labeled at their SNAP-tags and magenta spots correspond to unspecific binding of the SNAP-Surface 549® label to other cell-surface structures. The representative image of too much unspecific binding (4µM) shows 24.4 % unspecific labelling. Images are representatives of at least n = 3 independent experiments

To assure that the ligand-binding of the μOR was not affected by the N-terminal SNAP-tag addition, I compared the SNAP- tagged construct (**Figure 32a**) with the wildtype receptor (**Figure 32b**) in radioligand-binding assays and showed that K_i- values were impaired neither for low- nor for high-affinity binding states. The pK_i-value of DAMGO at the high-affinity state of the SNAP-tagged μOR was 8.83 ± 0.12, which does not differ significantly from the value for the untagged, wildtype receptor (8.96 ± 0.13).

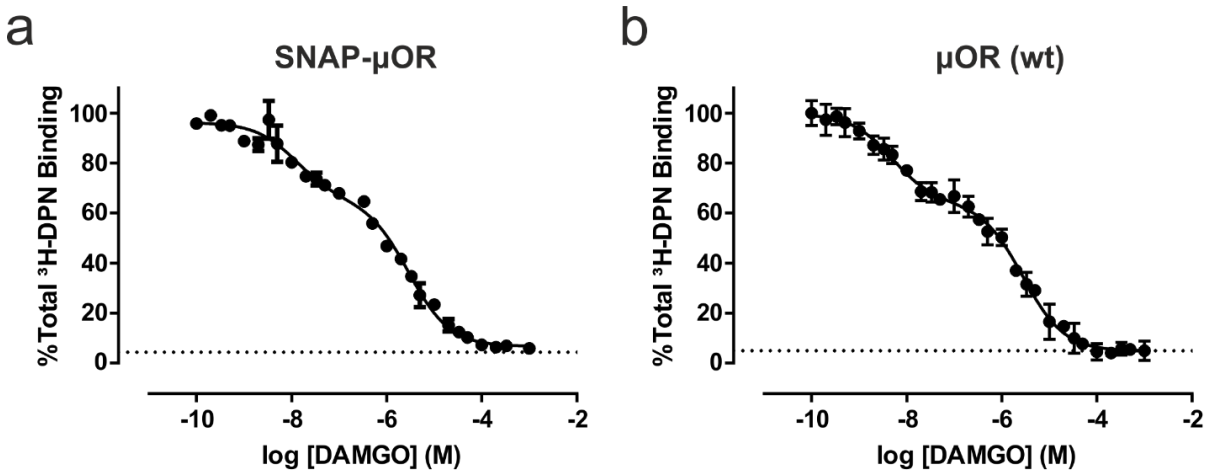

Figure 32: Radioligand binding for construct validation

Biphasic binding curve of the SNAP-tagged μOR (pKi(high)= 8.83 ± 0.12, pKi(low)= 5.85 ± 0.06) does not differ significantly from the values for the untagged, wild-type receptor (pKi(high)= 8.96 ± 0.13, pKi(low)= 5.87 ± 0.06) shown in b. The dashed line indicates unspecific binding. The radioligand used is [15,16-^{3}H]- diprenorphine (DPN). Shown numbers are means ± SEMs and experiments were repeated independently n = 3 times on 3 different experimental days.

To further exclude an influence of the tags on the signaling behavior I compared G protein coupling (based on high-affinity binding) and G protein activation (using a FRET-based G protein activation sensor[165]). Based on this I could show that the addition of the SNAP-tag does not impair the G protein-mediated signaling (**Figure 33a,b**). First, G_i protein-recruitment indicated by high affinity binding (receptor/G protein coupling) was not impaired by SNAP-tag insertion (SNAP-tagged= 37.3 ± 2.5% vs. wildtype= 34.3 ±1.9%) (**Figure 33a**). Also, G_i protein activation occurred at essentially the same DAMGO concentrations for SNAP-tagged and wildtype receptors (pIC_{50}-wildtype = 9.2 ± 0.1 vs. pIC_{50}-SNAP-tagged = 8.9 ± 0.2) (**Figure 33b**).

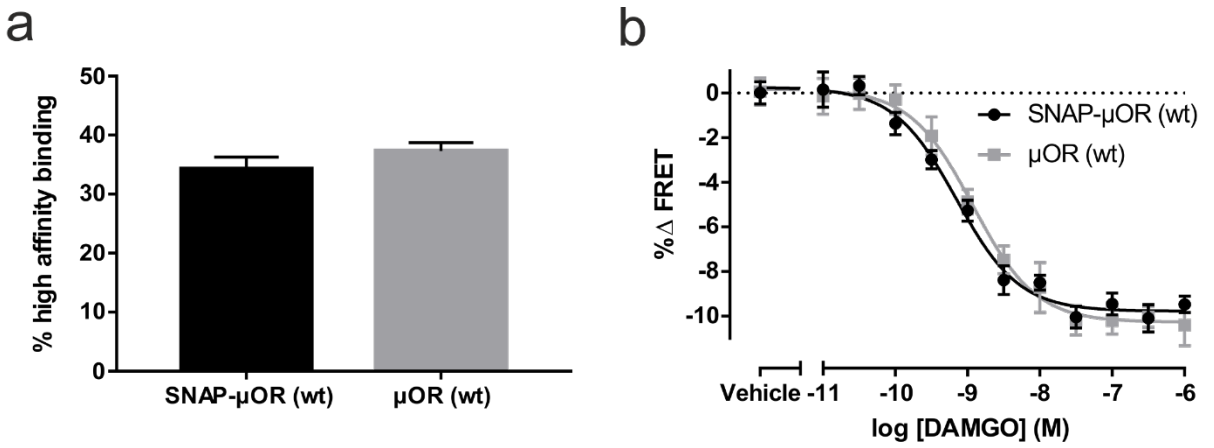

Figure 33: G protein recruitment and activation of the untagged vs. SNAP-tagged μOR wild-type constructs

a) High affinity binding indicating receptor/G protein coupling is not impaired by the SNAP-tag insertion. b) G_i activation FRET assays further confirm that G protein activation is not impaired (pIC50-wild-type= 9.2 ± 0.1 vs. pIC50-SNAP-tagged= 8.9 ± 0.2). The y-axis shows the differences between stimulated and basal FRET-ratios (YFP/CFP), relative to the basal FRET-ratio (termed within this work as ΔFRET). Shown numbers are means ± SEMs of at least n = 4 independent experiments.

Detection, tracking and motion-analysis of single labelled μOR particles was done with single-molecule TIRF microscopy and the Matlab-based tracking-software u-Track[171]. Spatial localization with an accuracy down to ≈25 nm was achieved via fitting of single point-spread functions (PSFs) ;(**Figure 34a**).

For most applications (apart from experiments for the analysis of dimerization kinetics) the temporal resolution in the recorded movies was between 30 and 40 ms. Using this approach, individual μORs on the surface of living cells were tracked by linking of the obtained coordinates from frame to frame (**Figure 34b**). Subsequent motion analysis further allowed us to classify receptor tracks according to their diffusion behavior[171], given by their confinement radius and diffusion coefficient[126]. The classification ranges from immobile receptors over confined and Brownian to directed diffusion (**Figure 34b**), according to the above mentioned parameters (Section 2.2.5).

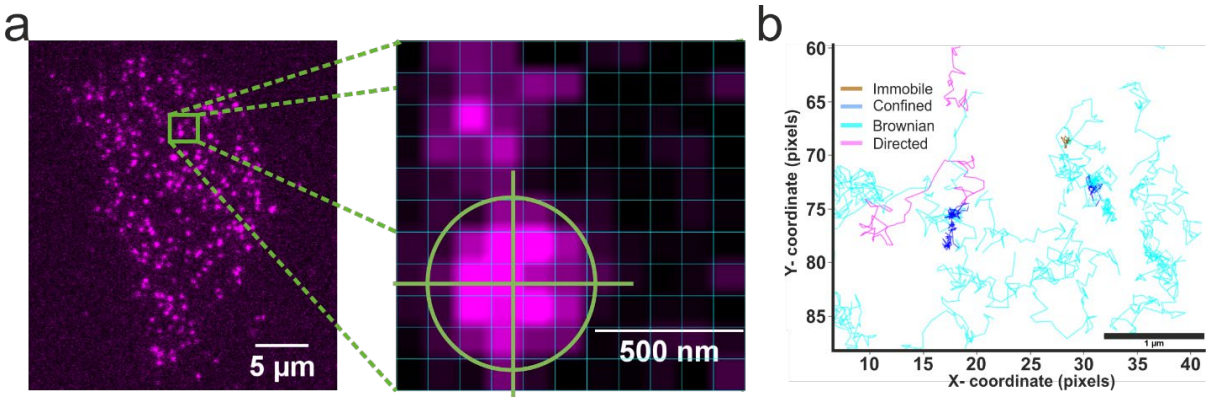

Figure 34: Fitting of individual point-spread functions and single-particle tracking of μORs
a) Diffraction limited single-molecule image (left) of SNAP-tagged receptor labeled with SNAP-Surface 549® Dye. Fitting of individual PSFs (right) allows a localization with sub-pixel precision of approx. 25 nm. Camera pixels are depicted as cyan grid (pixel-size 107 nm).
b) Tracks of single-molecule movies classified by u-Track based on their confinement radius and diffusion coefficient.

Simultaneously to the movie-acquisition of individual receptors, I imaged endogenous actin fibers with direct stochastic optical reconstruction microscopy (dSTORM) by co-expressing a Lifeact7-Halotag construct labeled with Janelia Fluor 646[180,181] (**Figure 35**). The super-resolved image was reconstructed from the acquired movies using the Thunderstorm ImageJ-plugin [170] and overlaid with the tracks obtained in u-Track[171] (**Figure 35b**). This kind of image-processing revealed that the μORs are compartmentalized on the cell surface within meshes formed by actin fibers.

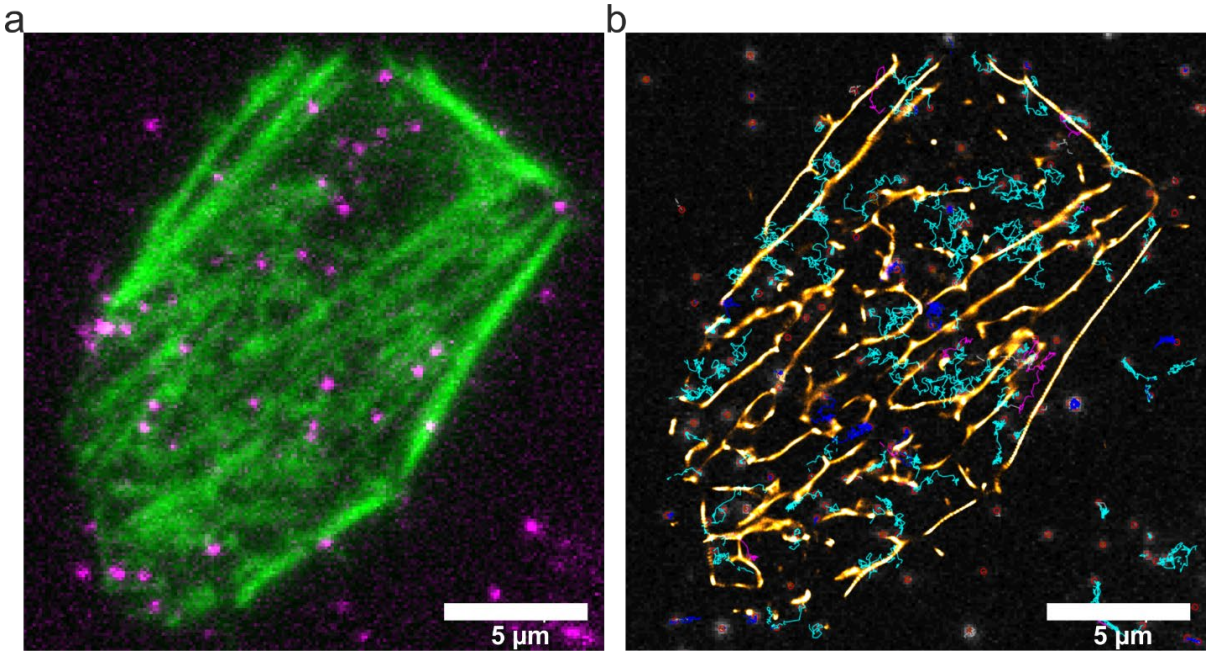

Figure 35:Simultaneous imaging of receptors and super-resolved actin
a) Diffraction limited image of representative live cell with dual-color acquisition of μORs (magenta) and actin (green). b) Super-resolved image of the cell in (a) showing that the μOR is compartmentalized by actin fibers. The track-color corresponds with the type of diffusion (magenta = directed diffusion, blue = confined diffusion, cyan = Brownian motion and brown = immobile). Shown images are representative of at least n = 5 independent experiments.

Receptor activation by 10 µM DAMGO accelerated the overall diffusion speed of the µORs and allowed an increased fraction of receptors to overcome actin barriers (**Figure 36** upper panels). After 5 minutes of DAMGO stimulation, receptors became increasingly immobile and compartmentalization was restored. The immobile fraction and compartmentalization further increased after 10 minutes and remained so after 15 minutes of DAMGO stimulation (**Figure 37**). The obtained distribution of diffusion coefficients (**Figure 36** lower panels) was shifted to higher values one minute after receptor stimulation with 10 µM DAMGO. Five minutes after stimulation, the diffusion coefficients returned to initial values, and the fraction of fast-diffusing receptors was reduced. This effect continued and stabilized after 10 minutes at a lower value.

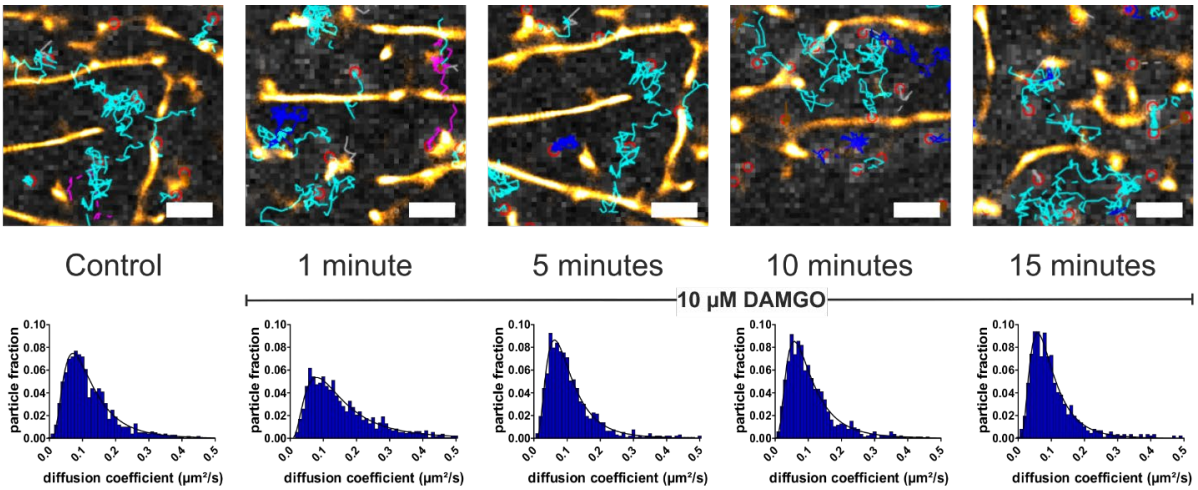

Figure 36: Receptor compartmentalization and diffusion after activation by DAMGO
Timeline of representative super-resolved images after application of 10 µM DAMGO (top) and corresponding diffusion coefficient distribution (bottom). After 1 minute, the receptors gain in mobility and cross more frequently actin-fibers. After 5 minutes the percentage of immobile tracks increases and remains stable after 10 minutes. Furthermore after 10 minutes the receptors show increased compartmentalization. (Scale bars in the shown images are 1 µm). Experiments were repeated independently n = 7 times on different experimental days. Images are representatives of five independent experiments with similar results.

For quantification of these observations I analyzed the distribution of diffusion classes (**Figure 37a**), totaled the number of tracks and calculated their percentage of crossing events (**Figure 37b**). The fast diffusion components (Brownian and directed) were significantly increased 1 minute after receptor activation. At later time-points the relative size of those components became smaller, accounting for an increase of the confined and immobile diffusion components. Interestingly, the percentages of tracks crossing actin-fibers were correlating with the receptor's mobility as derived from their diffusion behavior, suggesting that the increased compartmentalization at later timepoints is at least partially caused (due to an increase of confined diffusion) by these changes in the diffusion behavior.

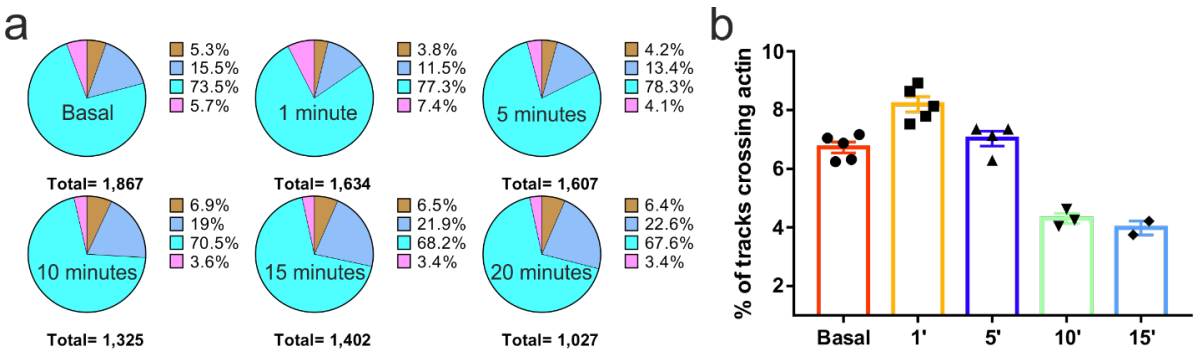

Figure 37: Distribution of diffusion classes and quantification of actin-crossing events after receptor activation

*a) Fractions of the diffusion classes shown in **Figure 36** over time assigned to the corresponding color-code (magenta = directed diffusion, blue = confined diffusion, cyan = Brownian motion and brown = immobile). b) Percentages of tracks undergoing actin-crossing events at different time-points after receptor activation with 10 µM DAMGO. Shown are mean ± SEM of n = 5 cells for basal and 1 minute, n = 4 for 5 minutes, n = 3 for 10 minutes, and n = 2 for 15 minutes.*

To further investigate the diffusion behavior, after receptor activation with DAMGO, I analyzed the diffusion coefficients within the individual diffusion classes (**Figure 38**). After 1 minute of stimulation, the diffusion coefficient of the immobile fraction was significantly reduced, whereas the diffusion coefficients of all three mobile fractions were increased. The directed diffusion underwent the most substantial increase and then decreased progressively until 15 minutes of stimulation. Conversely, the diffusion coefficients of the immobile, confined and Brownian motion class returned to basal levels after only 5 minutes of DAMGO stimulation.

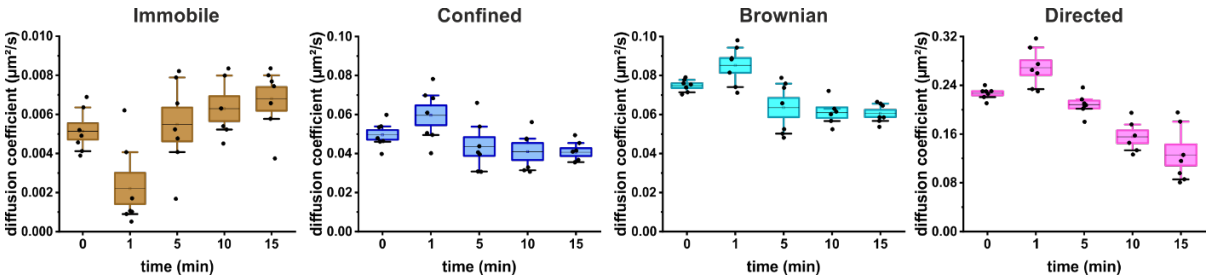

Figure 38: Diffusion coefficients of individual diffusion-classes after receptor activation with DAMGO
Expanded diffusion analysis by classification of receptor-tracks based on their diffusion behavior (classification defined in methods). After 1 minute the diffusion speed of the immobile fraction is reduced, whereas the speed of all mobile fractions is increased. After 5 minutes diffusion of the immobile fraction increases again, and mobile fractions slow down again. The line indicates the mean, boxes show SEM and whiskers are the IQR..

3.2. Basal receptor dimerization occurs fast and the homodimer population is low

3.2.1. Intensity distribution analysis

To evaluate the oligomeric status of the μOR, I analyzed individual PSFs from single-frame TIRF images. To avoid bias towards the monomer population caused by photobleaching, only the first frame of each TIRF-movie was used for the intensity distribution analysis. As a monomer control I used an N-terminally SNAP-tagged construct of the β_1-adrenergic receptor (β_1AR), previously shown to be predominantly monomeric [29,157], whereas a SNAP-CD28 construct served as dimer control [157,182]. Application of multi-Gaussian fits (**Figure 39**) indicated that the controls can be reliably used at the receptor densities analyzed. The area under the curve (AUC) of the β_1AR (**Figure 39a**) at a density of 0.148 particles/μm^2 revealed a monomer fraction of 90.4 ± 0.5 % and a dimer fraction 9.5 ± 0.1 %, with negligible trimer and tetramer fractions. The dimer control CD28 (**Figure 39b**) showed 89.8 ± 1.6 % (AUC) dimers at a density of 0.114 particles/μm^2.

For the μOR (**Figure 39c**) I obtained a monomer fraction of 91.9 ± 1.1 % even at expression levels that were somewhat higher than those of the controls (0.271 particles/μm^2). Only a small dimer population of 5.9 ± 1.8 % was suggested by the fit. Trimers and tetramers were not detected.

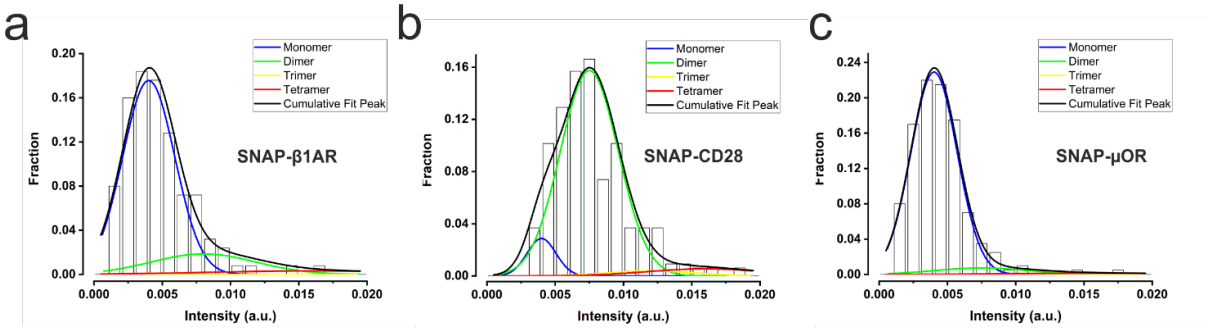

Figure 39: Intensity distribution analysis of monomer/dimer controls and the μOR
Representative intensity distribution analysis based on TIRF images of different receptor constructs labeled with SNAP-Surface 549® dye. The data are fitted by applying a mixed Gaussian fit allowing the detection of monomer, dimer, trimer and tetramer fractions of the receptors. The density of particles was 0.148 particles/μm^2 for β_1AR, 0.114 particles/μm^2 for CD28 and 0.271 particles/μm^2 for the μOR. Plots are representatives of at least n = 11 cells.

To further understand the dependency of these results on the receptor expression level, I conducted analogous experiments at levels ranging from 0.1 to 0.3 particles/µm² (**Figure 40**). The β_1AR showed a mainly monomeric constitution up to a density of 0.3 particles/µm²; above this density, PSFs started to overlap (**Figure 41**) and showed increasingly double or higher-order intensities. Conversely, CD28 showed a dominant dimer population even at very low expression levels; at expression levels above 0.3 particles/µm² also CD28 showed PSFs of higher order. Again, the µOR behaved quite similar to the β_1AR, but with an even higher fraction of monomers.

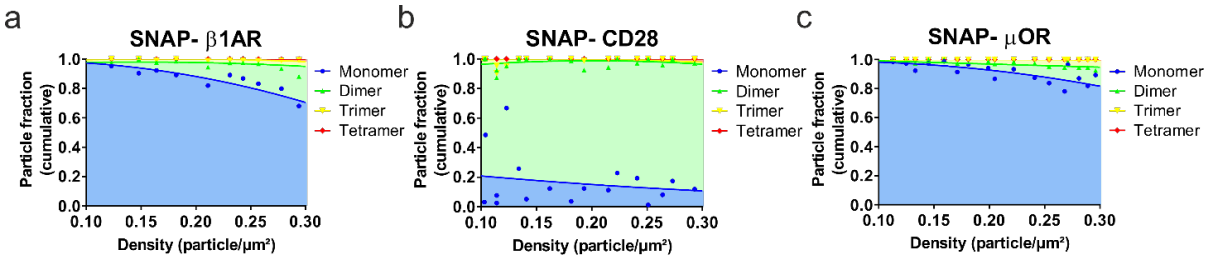

Figure 40: Oligomeric distribution for different particle densities
*Cumulative oligomer-fractions plotted over density of particles, based on analysis as shown in (**Figure 39**). Each data point corresponds to one cell. Each data point corresponds to one cell, n = 11 different cells on three independent experimental days (a), n = 17 different cells on four independent experimental days (b) and n = 18 different cells on four independent experimental days (c). The trend lines are based on a second-order polynomial fit.*

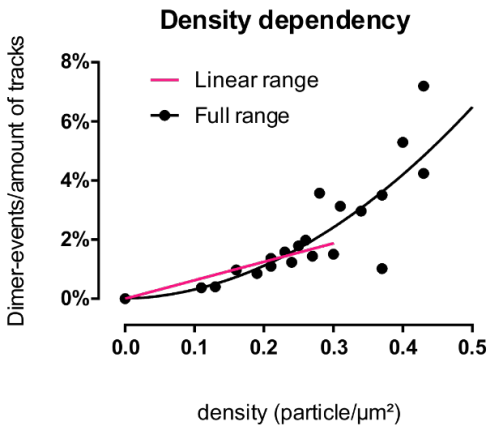

Figure 41: Density dependence of random co-localization events
The linear range (magenta) shows up to which density single-molecule experiments can be conducted without density-driven bias. The polynomic fit (black) indicates the occurrence of dimerization events, which are rather based on random co-localization than true dimerization events.

To investigate if real dimers occur at higher expression levels (up to 50 receptors/µm^2) and to further exclude that the SNAP-tags might influence the dimerization, an entirely different approach was used and the molecular brightness of the SNAP-tagged constructs as well as of the corresponding C-terminally YFP-tagged constructs was measured (**Figure 42a**). These data with YFP-tagged constructs, measured by using number and brightness analysis[183], confirmed the largely monomeric nature of the β_1AR and the µOR, while CD28 was almost perfectly dimeric (**Figure 42a**). Analogous results were obtained with spatial intensity distribution analysis[163] (SpIDA), in which I used again the SNAP-tagged constructs labelled with SNAP-Surface 549® Dye (**Figure 42b**).

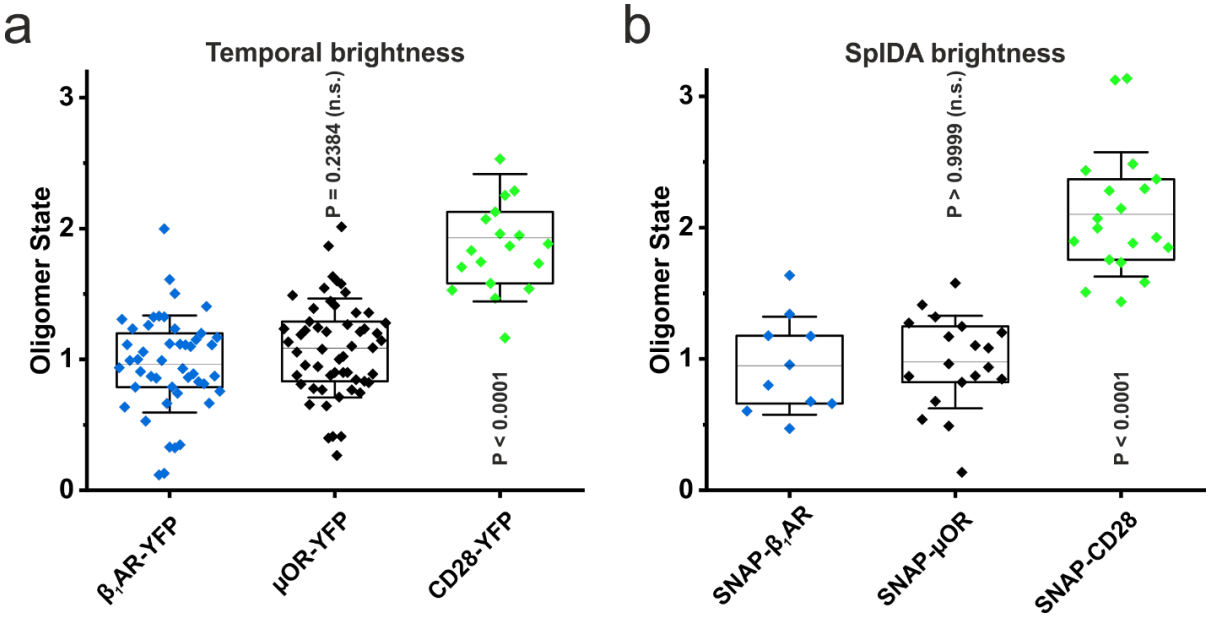

Figure 42: Validation of receptor dimerization with brightness analyses at higher expression levels
(a), Temporal molecular brightness measurements for corresponding C-terminally tagged YFP constructs confirm that the β_1AR and µOR are largely monomeric. In contrast, CD28 results in an almost perfectly doubled brightness. Furthermore, these experiments show that dimerization is not influenced by the N-terminal SNAP-tag used for single-molecule studies.
(b), SpIDA brightness measurements with SNAP-tagged receptor constructs show that results also agree when SNAP-constructs are used in molecular brightness experiments.
(Molecular brightness measurements are normalized to the as monomer control used β_1AR)
The line shows the mean and each datapoint represents one cell. The box shows IQR and whiskers are SD. P values were determined by one-way ANOVA and Tukey's multiple comparison test.

Furthermore, I conducted FRET-measurements between the SNAP-tagged constructs labeled with SNAP-Surface 549® and SNAP-Surface Alexa Fluor 647® dyes. FRET was measured by acceptor photo-bleaching (FRET-AB) on a confocal-microscope[157] (**Figure 43**). Also, this method confirmed the reliability of the used controls as well as the monomeric behavior of the unstimulated wildtype μOR.

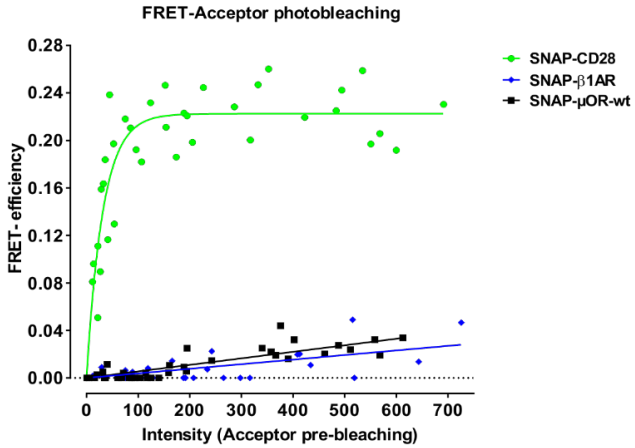

Figure 43: Validation of receptor dimerization using FRET-AB measurements at higher expression levels
(a), Acceptor photobleaching experiments on a confocal microscope with dual-color labeled SNAP-constructs also confirm the monomeric nature of β_1AR and the μOR by linearly increasing FRET-efficiencies at high expression levels. In contrast, the dimer-control SNAP-CD28 shows a steep increase and quick saturation of the measured FRET-efficiencies upon increasing expression-levels. Each datapoint represents one cell and the experiments were repeated independently n = 3 times.

Taken together all results in this section confirmed that the controls are reliable and indicate that intensity-increases at levels above 0.3 particles/μm^2 are caused by overlapping PSFs rather than by dimerization. The wildtype μOR showed with all approaches used a clearly monomeric behavior under basal conditions.

3.2.2. Single particle tracking and dimerization kinetics

To better understand the monomeric behavior of the μOR and to assess the kinetics of possible dimerization/splitting events, I analyzed tracks of single-PSFs using TIRF-movies with very high temporal resolution at 100 frames/second. To catalogue and measure transient co-localization events as in **Figure 44**, a collaborator (Brendan Osberg) created a Matlab software package, which is in this work called "Polytracker" and automated the processing of tracks to achieve sufficient statistical significance for these sensitive measurements. With this algorithm, I obtained the lifetimes of transient co-localization events, among other observables.

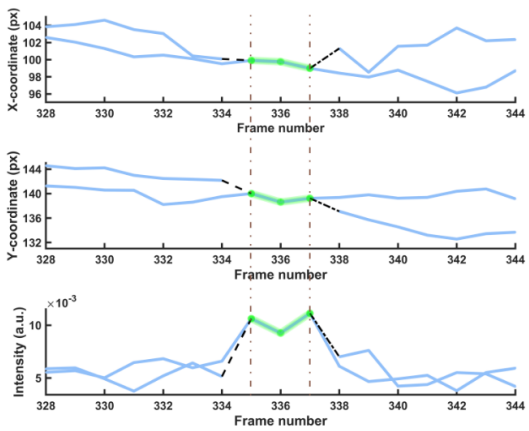

Figure 44: Transient dimerization event
Individual representative tracks, based on experimental data, for a merge/split event of two receptors, showing doubled intensity as evidence for true co-localization as detected by the tracking algorithm (color change from blue (monomeric) to green (dimeric state)).

Using a bi-exponential decay fit starting at the peak of the distribution, I aimed to distinguish the kinetics of plain co-localization by random presence at the same position from true dimerization (**Figure 45**). To obtain the τ-value of random co-localization events a collaborator (Vikram Sunkara), simulated together with me a series of movies comprising the same PSF-size, particle density and diffusion coefficients as captured for the four different mobility fractions and their relative proportions in the acquired real TIRF-movies (**Figure 34b**, **Figure 37**). In a modification to previous investigations of our lab [29] I set the search radius to a minimum (approx. the full width at half maximum (FWHM) of the PSFs), in order to minimize the percentage of random overlaps. I then approximated the distribution of random co-localization times as a mono-exponential decay[184]. A fit of the simulated data (**Figure 45a**) gave a τ-value of 112 ms; this is shorter than found earlier for monomeric controls[29,126] or simulated random collision events[29] in measurements from our lab. Application of a bi-exponential decay fit with a constrained τ- value for the random co-localization component produced a slower component of 459 ± 18 ms, which unveils very transient true receptor interactions with a fast decay of dimers. However, as a technical limitation in this approach, it should be noted, that these experiments can only detect those dimerization/splitting events that are complete within a single tracking movie, i.e. within 5-10 seconds. The reason is that such fast acquisitions require the usage of high laser intensities, which relate to an accelerated bleaching of the fluorophores used. With a random collision only fraction of 87.6 ± 3.8, the percentage of receptors undergoing true interactions under basal conditions is quite low, confirming the essentially monomeric nature of the μOR.

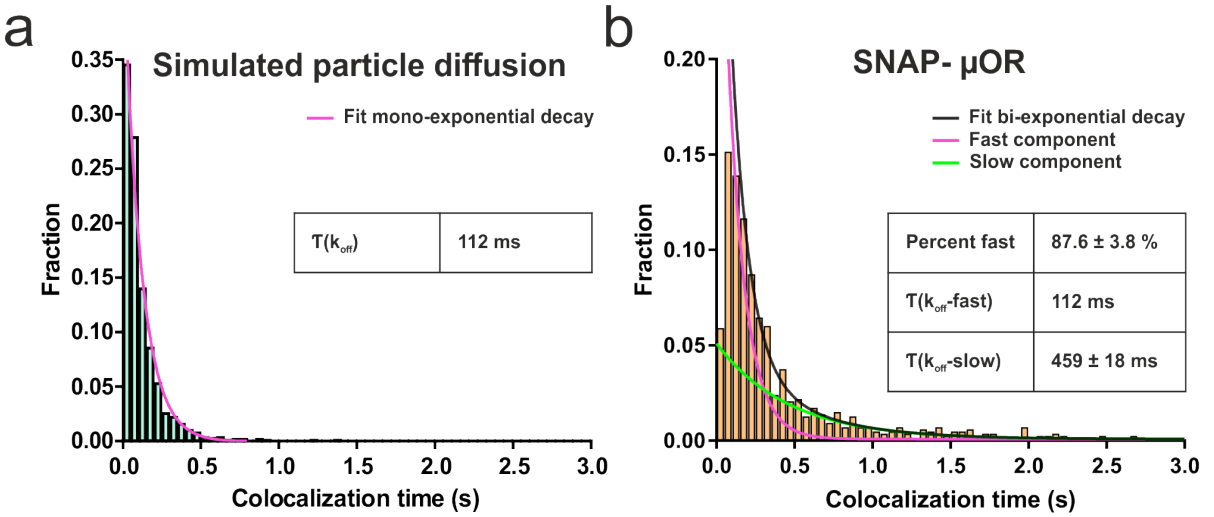

Figure 45: Dimerization kinetics and correction for random co-localization

*(a), Distribution of co-localization times derived from tracks as shown in **Figure 44**, based on simulated movies using diffusion data from **Figure 36** to obtain the τ-value for random co-localization (112 ms with an error below 1 ms).*

*(b), Distribution of co-localization times derived from tracks as shown in **Figure 44**, based on real μOR single-molecule movies. Application of a bi-exponential fit starting from the center of the distribution differentiates the two components of random collision and receptor dimerization. The slow component (green), represents true dimerization events for τ_1 of 459 ± 18 ms. The fast component (magenta) is based on the simulations in (a) constrained to τ_2 of 112 ms. Data are τ value and 95% confidence interval (CI) on the basis of 887 tracks containing merge/split events from n = 31 cells and four independent experiments.*

3.3. μ- Opioid receptor dimerization follows agonist-specific receptor activation

3.3.1. Ligand effects on μ-opioid receptor dimerization and diffusion

To understand how different ligands might affect μOR diffusion and dimerization, I recorded and analyzed single-molecule movies at different time-intervals after application of ligands (**Figure 46**). I used as antagonists the classical, also clinically used, high affinity antagonist naloxone[185] and β-funaltrexamine[186](β-FNA), an irreversible (covalently) binding antagonist, which was used before to stabilize the inactive receptor state in the dimeric crystal structure[34]. As agonists I chose the probably best-known opioid morphine, which poorly mediates internalization of the μOR[187–189], as well as DAMGO, a ligand which promotes fast phosphorylation of the μOR[190,191], followed by β-arrestin2-mediated internalization[192]. To facilitate comparison, I normalized all data to the oligomer distribution of the μOR under basal conditions. Among the 4 prototypical ligands used, DAMGO was the only one that significantly affected μOR oligomerization. It caused a time-dependent increase of dimers by up to 79 ± 4 % (**Figure 46a**). Remarkably, even after longer times of DAMGO stimulation the oligomer size did not exceed a value of 2, indicating that DAMGO induced predominantly formation of μOR dimers, but not of higher order oligomers. In contrast, morphine did not lead to receptor dimerization even after 20 minutes of stimulation (**Figure 46b**). A very similar oligomerization behavior was measured for the antagonists β-FNA and naloxone (**Figure 46c+d**), pointing out that μOR-dimerization in living cells at least requires an active- state of the receptor and furthermore a conformation, modification or interaction which is not occurring upon morphine stimulation. Even though I repeatedly observed a very small fraction of dimers with β-FNA (in average less than 3%), the oligomeric state was overall not significantly different from those in presence of naloxone or morphine. Since furthermore a TM5/TM6- dimer interface is just compatible with an inactive receptor[34,35] the small number of dimers caused by β-FNA might eventually be the dimeric complex observed in the inactive crystal structure[34].

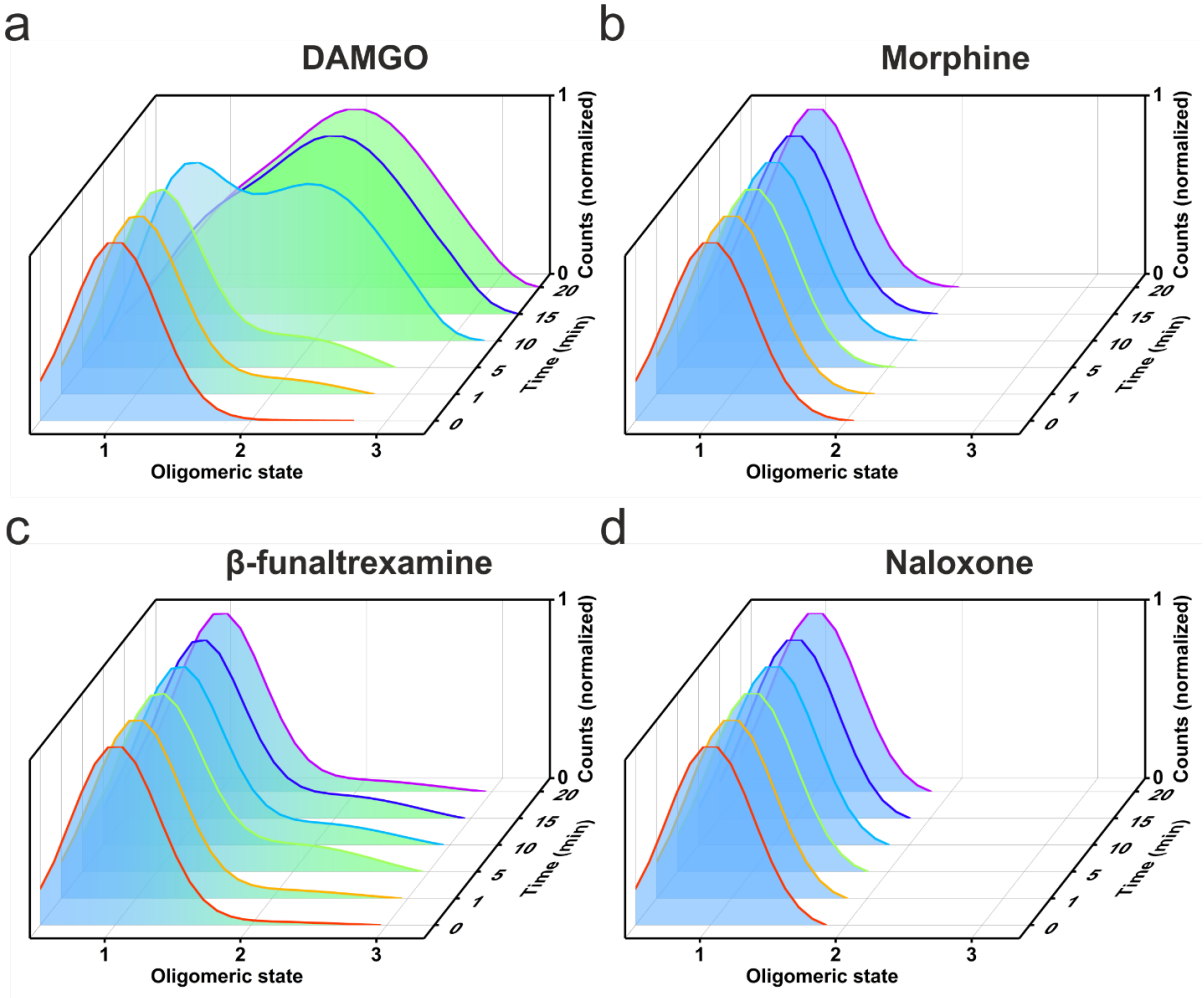

Figure 46: Ligand influence on μOR dimerization over time
Oligomerization state of the μOR normalized to untreated wildtype receptor.
(a), DAMGO leads to a significant increase of dimerization starting 5 minutes after application of 10 μM DAMGO.
(b), The μOR remains in its monomeric state upon application of 10 μM morphine.
(c), β-FNA treatment does not lead to a significant change of the oligomerization state but allows a small number of receptors to form dimers after 10 minutes.
(d), Naloxone treatment does not alter the receptors monomeric constitution.
Data from (a) n = 51, (b) n = 46, (c) n = 38 and (d) n = 27 cells of at least three independent experimental days.
For further statistics and significance of effects see: ***Annex*** .

The distinct agonist effects on receptor dimerization were also confirmed using molecular brightness measurements based on SpIDA (**Figure 50a**). This result shows, that the DAMGO induced dimerization is specific and principally independent of the receptor density (expression levels), as the molecular brightness in DAMGO experiments did not overcome the values measured with the dimer-control CD28.

Ligand effects on μOR diffusion were more complex (**Figure 47**). While naloxone caused no significant alteration, the irreversible antagonist β-FNA progressively reduced the diffusion by ≈ 50 % after 15 minutes. This reduced diffusion after β-FNA treatment cannot be explained by formation of homodimers or higher order complexes of the receptor itself, since the oligomerization state stays predominantly monomeric. Among the agonists, both morphine and DAMGO caused a small increase in the diffusion coefficient after 1 min, but at 15 minutes DAMGO caused a significant reduction by ≈ 25 %.

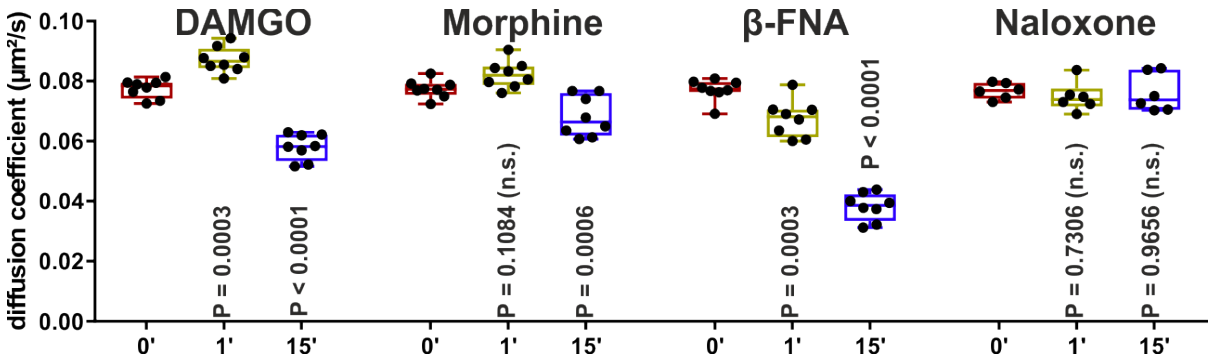

Figure 47: Ligand influence on μOR diffusion

The untreated wildtype receptor has a diffusion coefficient of 0.077 ± 0.002 μm²/s, β-FNA slows down receptor diffusion (1 minute = 0.067 ± 0.003 μm²/s ; 15 minutes = 0.038 ± 0.002 μm²/s). In contrast, administration of 10 μM DAMGO or 10 μM morphine initially accelerate the diffusion of the μOR (DAMGO 1 minute = 0.087 ± 0.002 μm²/s; morphine 1 minute = 0.082 ± 0.003 μm²/s), but just DAMGO leads to a significantly decreased diffusion-coefficient after 15 minutes (DAMGO = 0.058 ± 0.002 μm²/s; morphine = 0.070 ± 0.004 μm²/s). Naloxone has no significant influence on the diffusion of the receptor (1 minute = 0.074 ± 0.002 μm²/s; 15 minutes = 0.077 ± 0.003 μm²/s). P values are from one-way analysis of variance (ANOVA) followed by Tukey's multiple comparison test and each datapoint shows one experiment. The line of the box plots shows the median, the box is the interquartile range (IQR) and whiskers show the minimum and maximum.

3.3.2. Diffusion and oligomerization behavior of receptor mutants

As an independent approach to link receptor activation to their diffusion and oligomerization behavior, I used constitutively active (T279K) and inactive (T279D) variants of the μOR[193]. The effects of these mutations in terms of decreased (T279D) vs. increased (T279K) G_i protein-coupling derived from high affinity agonist binding (**Figure 48a, b**) were confirmed. The PTX-treated wildtype receptor served in these binding experiments as a control for the absence of high affinity binding since it entirely uncouples G_i due to cysteine-351 ribosylation of the α-subunit[194]. To show the functional consequences of these mutants I measured G_i protein-activation (**Figure 48c**) using the above mentioned FRET based sensor[165] and inhibition of cAMP production (**Figure 48d**) with an Epac-based FRET sensor[166]. In both functional assays the pIC_{50}/pEC_{50} was right-shifted for the T279D mutant by approximately three orders of magnitude (towards lower apparent affinities) and close to the K_i-value of low affinity binding (**Figure 48a**). The span of the sensor's response was minimal but not significantly increased over the wildtype μOR, suggesting that a basal activity[195,196] of this receptor is not much altered by the T279D mutation. In case of the T279K mutant the receptor activated the G protein sensor already under basal conditions to an extent under which no further change was detectable due to DAMGO application (**Figure 48c**). The further downstream measurements of a cAMP decrease, mediated through G_i protein activation, had a dramatically reduced span in comparison to the wildtype-μOR, further underlining the high basal activity of the T279K mutant[193,195].

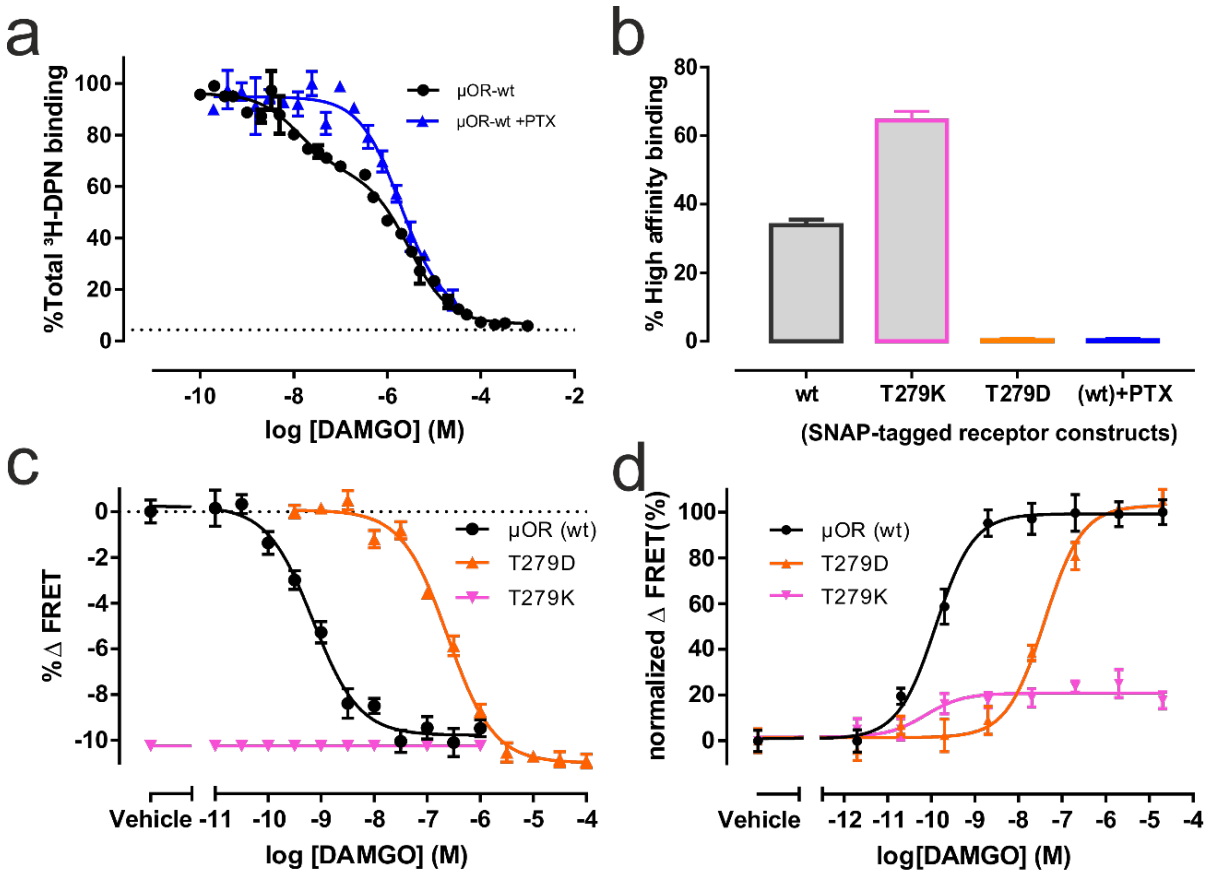

Figure 48: Characterization of μOR-mutants shows high basal activity of the T279K mutant and impaired activation of the T279D mutant

(a), 24 hour pre-treatment with 100ng/mL PTX abolishes high-affinity binding (≤ 1 %) due to $G\alpha_i$ inactivation. (b), Fraction of high- affinity binding is dramatically increased for the constitutively active T279K mutant (64.4 ± 1.6 %). High affinity binding is abolished in the T279D mutant (≤ 1 %) comparable to PTX treated wildtype receptor. (c), For the T279K mutant maximum G protein activation occurs already without DAMGO stimulation, leading to a full activation of the G_i - FRET sensor in the unliganded state.

(d), Measurement of basal receptor activity and its mutants, based on G_i-mediated cAMP decrease, after receptor activation with DAMGO. Cells were prestimulated with 1 μM forskolin to slightly elevate cAMP levels. The pEC_{50} of the constitutively active mutant (10.1 ± 0.1) does not significantly differ from μOR-wildtype (9.9 ± 0.4). Due to the high basal activity of the T279K mutant the amplitude of additional G_i activation via DAMGO is dramatically reduced (20.8 ± 1.7 %), compared to the wildtype receptor (100 %). The inactive T279D mutant shows a pEC_{50}-value right-shifted by 2-3 log-units (7.4 ± 0.1) while the amplitude is slightly but not significantly higher than the one of the wildtype receptor (103 ± 2 %). Data are mean ± SEM from n = 3 independent experiments of each condition.

Compared with the wildtype receptor, the inactive T279D variant showed neither a change in oligomerization nor in its diffusion coefficient (**Figure 49a,b**). In contrast, the constitutively active T279K mutant differed in both parameters: oligomerization was significantly increased, similar as for DAMGO treatment after 15 minutes, to 76 ± 2% of dimers (**Figure 49a**). At the same time, the diffusion coefficient was significantly decreased (**Figure 49b**) underlining an increase of the protein- complex size (e.g. by interaction with other protomers like in dimerization events) as one would expect according to the Stokes- Einstein equation[197].

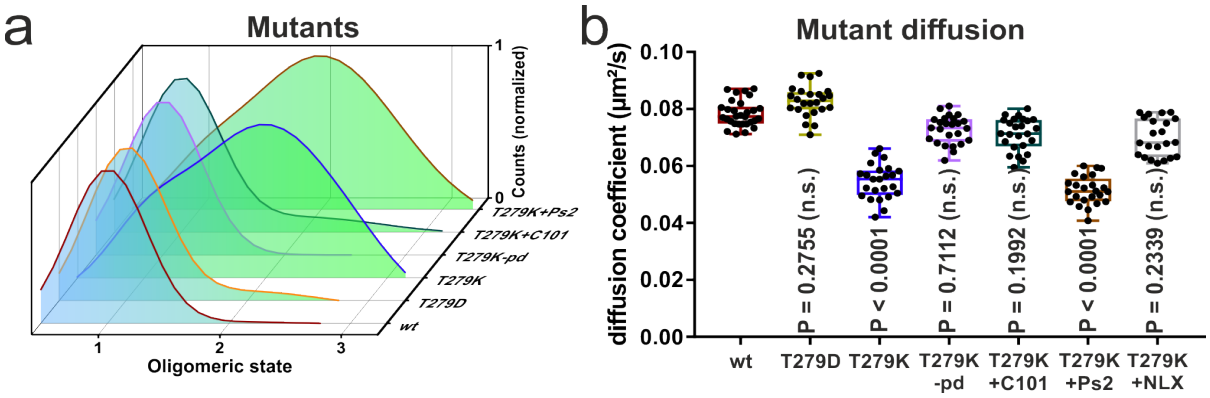

Figure 49: Mutagenesis influence on µOR dimerization and diffusion

*(a), The oligomerization state of the inactive T279D mutant does not differ significantly from the wildtype receptor. In contrast, the constitutively active T279K mutant shows a significant number of dimers, similar to treatment with DAMGO. A phosphorylation-deficient 11S/T-A variant[198] of the T279K mutant is almost as monomeric as the wildtype receptor. Inhibition of receptor internalization by 25 µM of the clathrin inhibitor Pitstop2 does not impair receptor dimerization of the T279K mutant. Naloxone application (**Figure 51**) drives the oligomerization equilibrium towards monomeric receptors. Data are from: T279D n = 7, T279K n = 9, T279K-pd n = 7, T279K+Cmpd101 n = 9 and T279K+PS2 n = 8 cells of at least three independent experimental days. For further statistics and significance of effects see: **Annex***

(b), The constitutively active T279K mutant has a similar diffusion- coefficient as observed for the wildtype receptor treated with DAMGO for 15 minutes (0.054 ± 0.003 µm²/s). The inactive T279D mutant exhibits diffusion similar to the wildtype receptor (0.080 ± 0.002 µm²/s). The phosphorylation deficient T279K mutant diffuses almost as the wildtype receptor (0.073 ± 0.004 µm²/s). Pitstop2 does not significantly influence the diffusion of the mutant (0.052 ± 0.008 µm²/s) and 10 µM naloxone brings the diffusion to values closer to those of the wildtype receptor (0.07 ± 0.004 µm²/s). P values are from one-way analysis of variance (ANOVA) followed by Tukey's multiple comparison test and each datapoint shows one experiment. The line of the box plots shows the median, the box is the interquartile range (IQR) and whiskers show the minimum and maximum.

Based on the Stokes- Einstein equation the diffusion- coefficient is formulated as:

$$D = \frac{RT}{N_A} \frac{1}{6\pi\eta r} \tag{11}$$

Since temperature and viscosity are kept constant in the observed system the relative relation between the diffusion coefficient and the radius of the particle can be formulated as inversely proportional:

$$D = \frac{1}{r} \tag{12}$$

For the observed diffusion coefficients of 0.077 $\mu m^2/s$ (wildtype) and 0.054 $\mu m^2/s$ (T279K-mutant) this results in an increase of the observed particle radius by a factor of 1.426. Based on the two-dimensional diffusion model, which one needs to assume in the conducted two- dimensional imaging, the particle size can be estimated as an area occupied by the receptor.

$$A = \pi r^2 \tag{13}$$

Taking now into account the increased radius by a factor of 1.426, the occupied area increases 2.03 times, resulting in an increase one could expect for a dimerized receptor.

The changes of particle Intensity and diffusion are both very similar to the effects observed after a 15-20 minutes stimulation with DAMGO.

The increased oligomerization of the constitutively active T279K mutant was also confirmed for higher expression levels by SpIDA-based molecular brightness analysis[163] (**Figure 50a**) as well as FRET-AB measurements (**Figure 50**b).

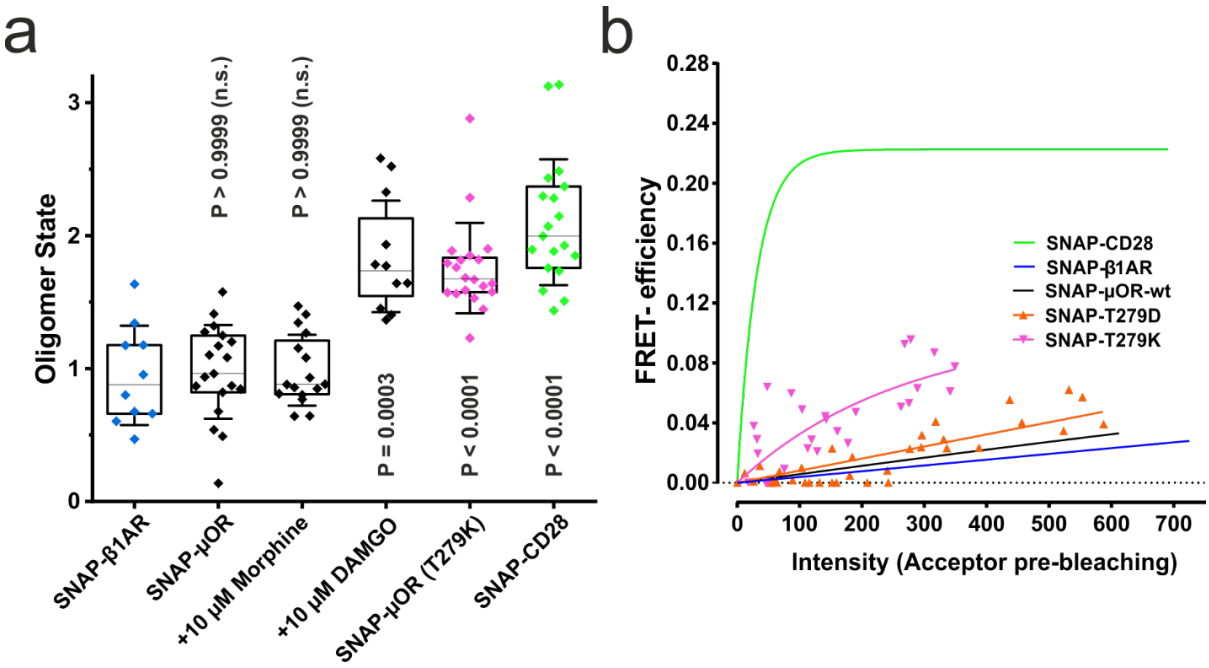

Figure 50: SpIDA and FRET-AB to confirm oligomerization behavior at higher expression levels
(a), SpIDA brightness measurements with SNAP-tagged receptor constructs show that results also agree for the used agonists and the constitutive active mutant. Receptor expression levels used in these experiments are ≈ 50 receptors per μm² and the brightness values are normalized to the as monomer control serving β_1AR. The line shows the mean and each datapoint represents one cell. The box shows IQR and whiskers are SD. P values were determined by one-way ANOVA and Tukey's multiple comparison test.
(b), The inactive T279D mutant of the μOR does not lead to a specific increase of the FRET- efficiency between receptor protomers. In contrast the T279K mutant shows specific, significantly higher FRET-efficiencies over increasing expression. Due to the constitutive activity of this mutant, expression levels higher than depicted could not be achieved. Curves for CD28 (green), SNAP-β_1AR (blue) and SNAP-μOR-wt (black) are taken from ***Figure 43****. Each datapoint represents one cell and experiments and are from n = 3 independent experimental days.*

A relationship between the constitutive activity of the T279K mutant and its ability to form dimers was confirmed by the observation that naloxone was able to antagonize dimer formation in a time-dependent manner, suggesting that inducing an inactive state of the mutant disrupted its dimers (**Figure 51**).

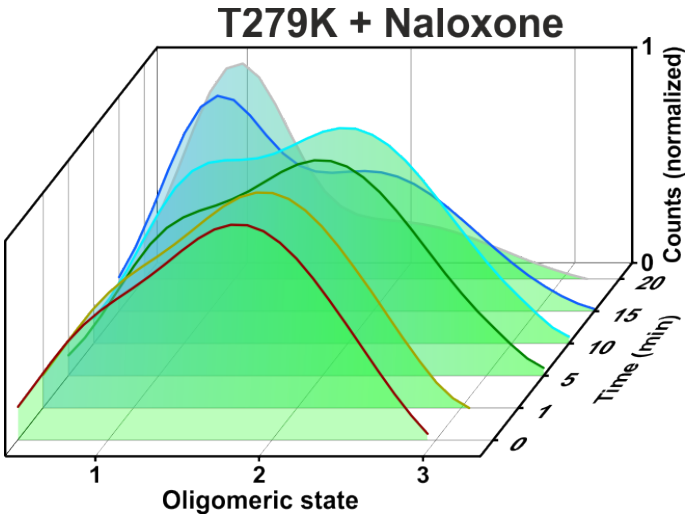

Figure 51: Dimer disruption by antagonist application
Application of 10 µM naloxone drives the equilibrium oligomerization state of the T279K mutant over time towards monomeric receptors, showing the reversibility of the dimerization. Date are from n = 39 cells of at least three independent experimental days. For further statistics and significance of effects see: ***9.Annex***

Naloxone also blocked the ability of DAMGO to induce µOR dimer formation (**Figure 52a**) and disrupted dimers that had already formed after addition of DAMGO (**Figure 52b**).

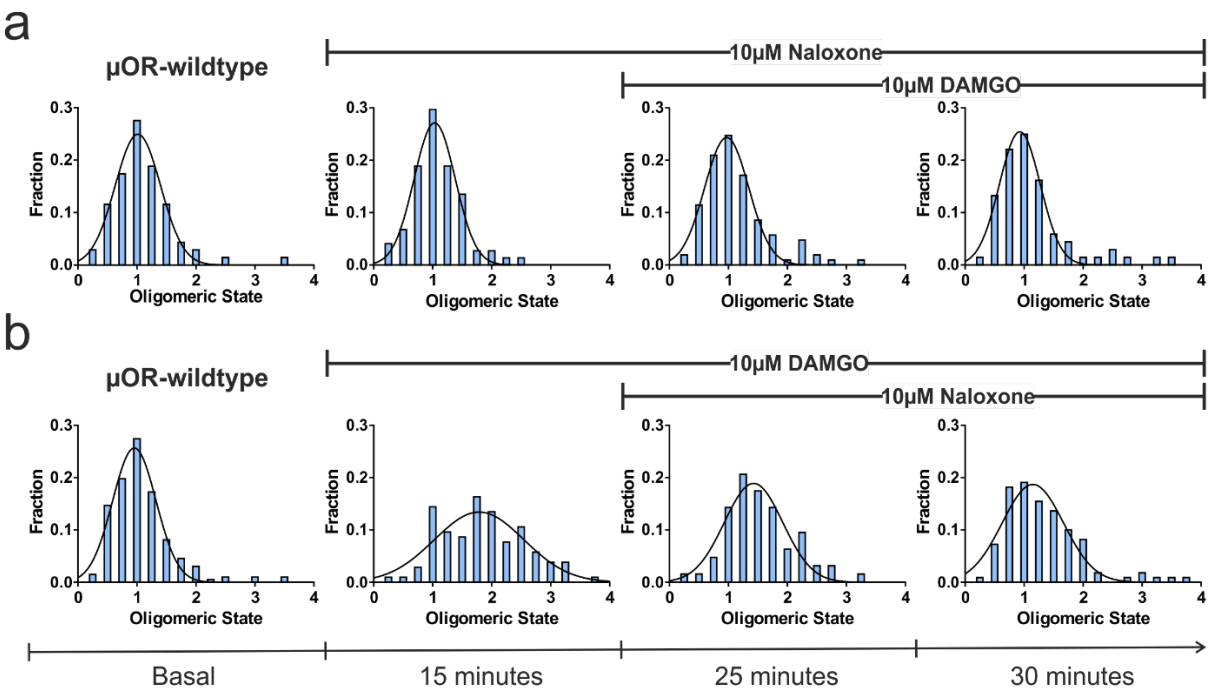

Figure 52: Effects of naloxone/DAMGO competition on µOR dimerization measured via intensity distribution
Representative intensity distribution analyses based on TIRF images of wildtype µOR at different time points, with naloxone and DAMGO (10 µM each) added as indicated: naloxone first (a) or DAMGO first (b). When naloxone is applied first, the µOR intensity distribution remains monomeric even after subsequent addition of DAMGO, indicating that naloxone prevents activation-dependent dimerization. When DAMGO is given first, the µOR intensity distribution indicates dimerization after 15 minutes, and addition of naloxone results in disruption of dimers as indicated by a progressive return to a monomeric distribution over the next 15 minutes. Experiments were repeated independently n = 3 times with similar results.

Since receptor activation by DAMGO is in contrast to morphine leading to prominent β-arrestin mediated signaling, the question about the impact of receptor phosphorylation and following β-arrestin recruitment on dimerization raised. Intriguingly, a variant of the T279K mutant lacking sites for GRK-mediated phosphorylation[198] failed to form dimers and was in fact behaving as monomeric as the wildtype μOR (**Figure 53a,b**). A very similar result was observed when the unmodified T279K mutant was treated with the GRK inhibitor Compound101 (Cmpd101) (**Figure 49a,b**). To distinguish dimer formation from clustering in the process of μOR internalization, I showed that addition of the clathrin inhibitor Pitstop2 to the T279K mutant had no effect on its dimerization (**Figure 49a,b**).

To put the effects observed for the T279K mutant in a more physiological context I conducted analogous experiments on the wild- type receptor (**Figure 53a,b**). The results were fully agreeing with the experiments on the T279K mutant in regards of oligomerization and diffusion behavior, suggesting phosphorylation as an essential requirement for the observed dimerization. I furthermore could hereby show that treatment with Pitstop2 – even though known for several non-specific effects[199–201] – did neither impair the dimerization behavior of the unstimulated receptor nor of the by DAMGO activated dimeric receptor-complex during the experimental time period.

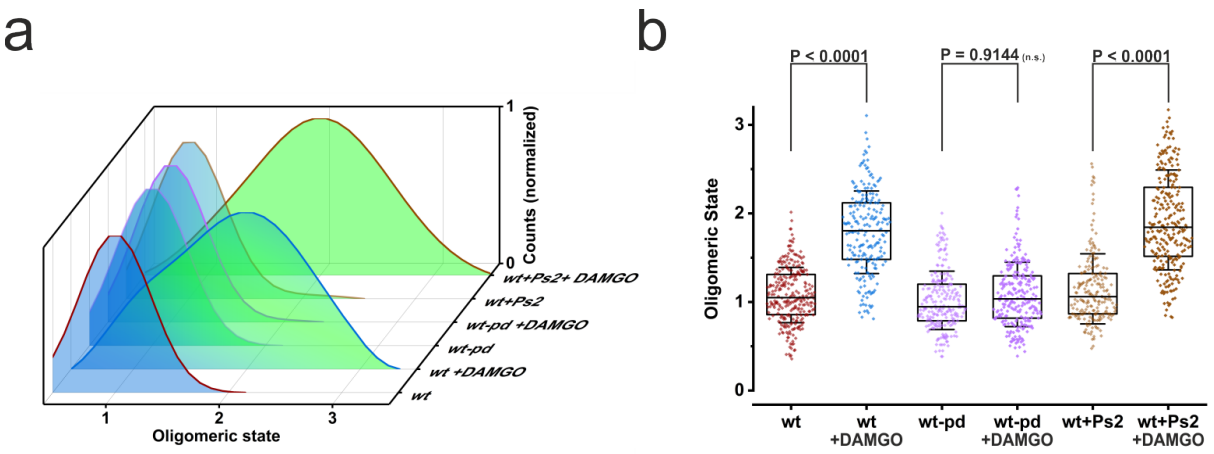

Figure 53: Influence of phosphorylation and relation to dimerization in the wildtype μOR
(a), Waterfall plots of wild-type μOR, its phosphorylation-deficient modification (pd) as well as wild-type μOR treated with Pitstop2 (Ps2) before and after activation with 10 μM DAMGO. The phosphorylation-deficient modification results after activation with DAMGO in a monomeric distribution of intensities. Pitstop2 had within the measurement time window no significant effect on the basal monomeric state of the μOR, nor on the DAMGO-induced formation of dimers. (b), Individual datapoints of the measurements in (a) and statistical significance of the observed effects. P values were determined by one-way ANOVA and Tukey's multiple comparison test.

Since receptor phosphorylation and following β-arrestin mediated receptor internalization can also lead through cluster formation to the occurrence of spots of higher intensities, further evidence was necessary to discriminate the observed dimers from internalization clusters. A difference between μOR dimers and clusters formed before or during internalization was indicated by the observation that the diffusion pattern of the dimers was rather closer to that of monomers and clearly different from more immobile clusters (**Figure 54**).

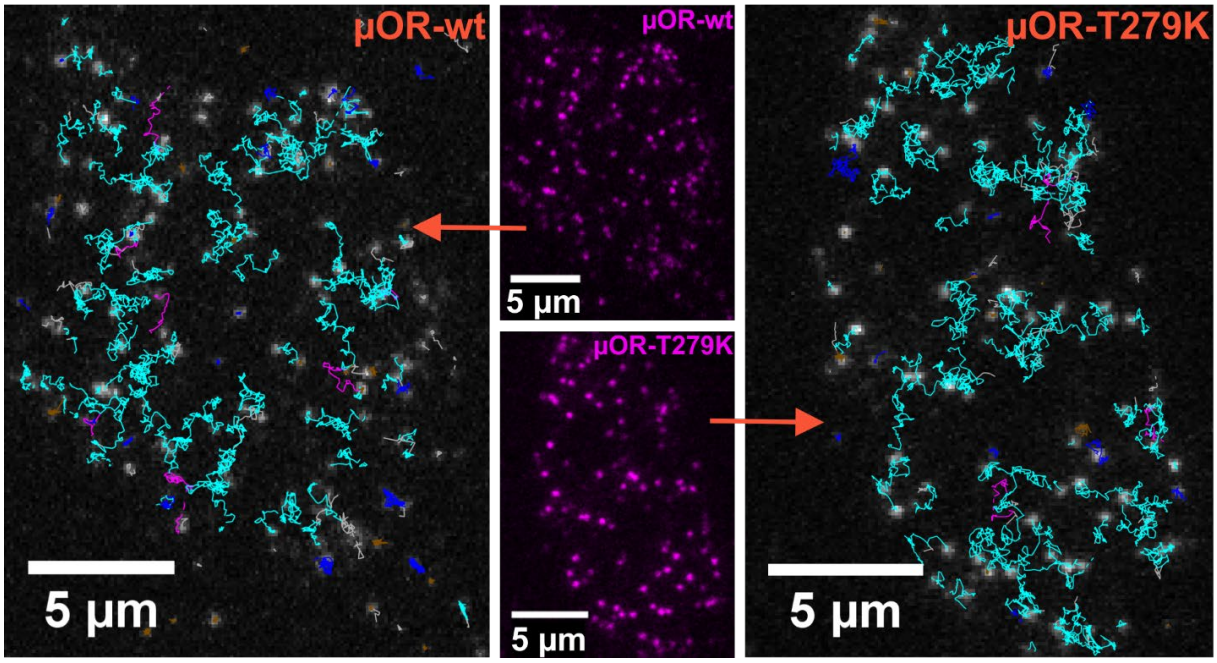

Figure 54: Diffusion pattern of the wildtype receptor vs. its constitutively active T279K mutant
Comparative images of μOR-wildtype and the μOR-(T279K) mutant show that the diffusion- pattern and distribution, of the T279K mutant is also receptor-typical (in contrast to receptors in pits or endosomes).

In addition, DAMGO-induced internalization occurred substantially slower (τ= 11.7 ± 0.3 min) than dimer formation (**Figure 55b**). The internalization assay used is based on the decrease of BRET, between C-terminally nanoLuciferase® tagged μORs and a non-internalizing construct of two Halo-tags, labelled with the HaloTag® NanoBRET™ 618 Ligand.

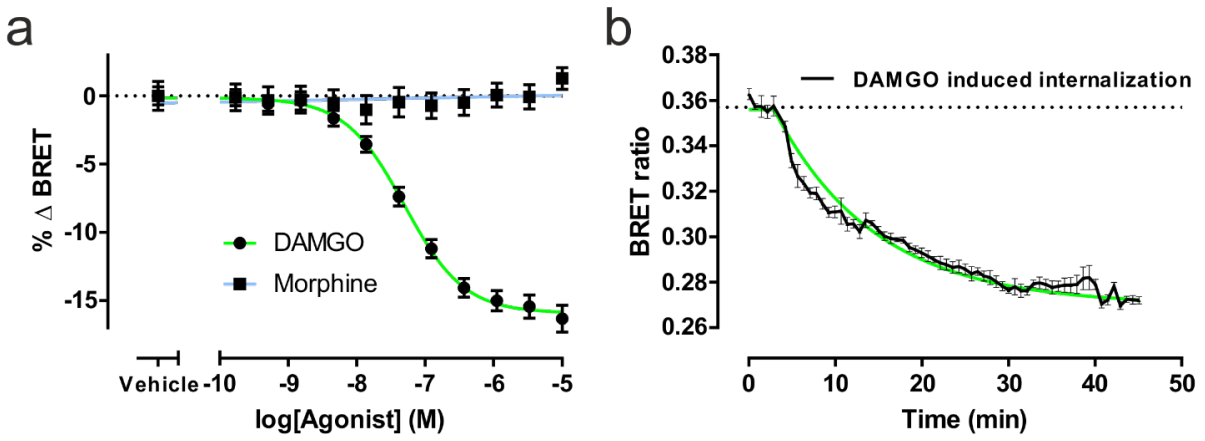

Figure 55: μOR- internalization assessed by BRET
(a), Concentration-response curve of a BRET-based internalization assay showing that DAMGO is leading to receptor internalization with a pIC_{50} of 7.3 ± 0.1. In contrast, morphine is not leading to receptor internalization at any concentration used in this assay.
(b), Internalization kinetics after stimulation with 10 μM DAMGO using the assay shown in (a) reveals a τ-value of 11.7 ± 0.3 minutes.
Datapoints in (a) and (b) are means and errors are given as SEM. Data shown in (a) are n = 3 independent experiments and (b) are n = 4 individual kinetic measurements

Finally, dimers of the T279K mutant did not overlap with clathrin clusters, while there was a clear overlap after prolonged stimulation of μOR with DAMGO, i.e. when μOR internalization was happening (**Figure 56**). It should also be noted that such clathrin-colocalized internalization clusters of multiple receptors and intensities of higher order oligomers were mainly just visible with a deeper penetration depth of the laser.

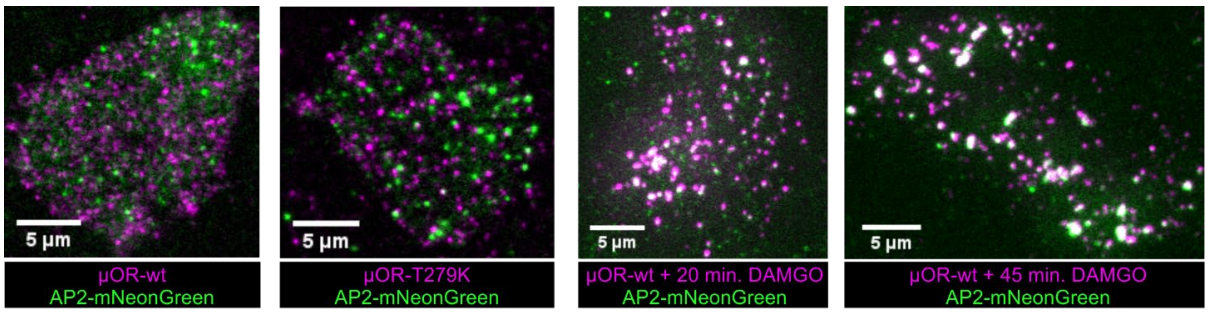

Figure 56: μOR-internalization assessed by clathrin co-localization
Dual-color single-molecule TIRF images illustrate that the unstimulated wildtype receptor as well as the T279K mutant show negligible co-localization with clathrin. Using a steeper TIRF-angle and thereby increasing the penetration depth of the laser shows receptor co-localizations of higher order intensities (up to ten fluorophores per spot) and co-localization with clathrin underneath the plasma- membrane after 20 minutes, and more strongly after 45 minutes, of stimulation by 10 μM DAMGO, illustrating μOR internalization.
Images are representatives of at least five independent experiments.

3.4. Nanoscale visualization clarifies quaternary receptor organization

3.4.1. dSTORM imaging shows that the distance between receptor protomers is below super-resolution level

Next a single-molecule super-resolution method, direct stochastic optical reconstruction microscopy (dSTORM)[146] was used and the μOR and its T279K mutant were imaged on the same TIRF microscope setup, which was also used for the previous single-molecule experiments with near-molecular spatial resolution[202]. Therefore receptors were before cell fixation labelled with SNAP-Alexa Fluor647®, a suitable dye for dSTORM[203], and imaging was conducted over ≈ 20,000 frames for each sample. The settings were calibrated using a DNA origami-based nanoruler® (**Figure 57a**)and showed that the experimental setup was sufficient to resolve fluorophores with a distance of 40 nm (**Figure 57b**).

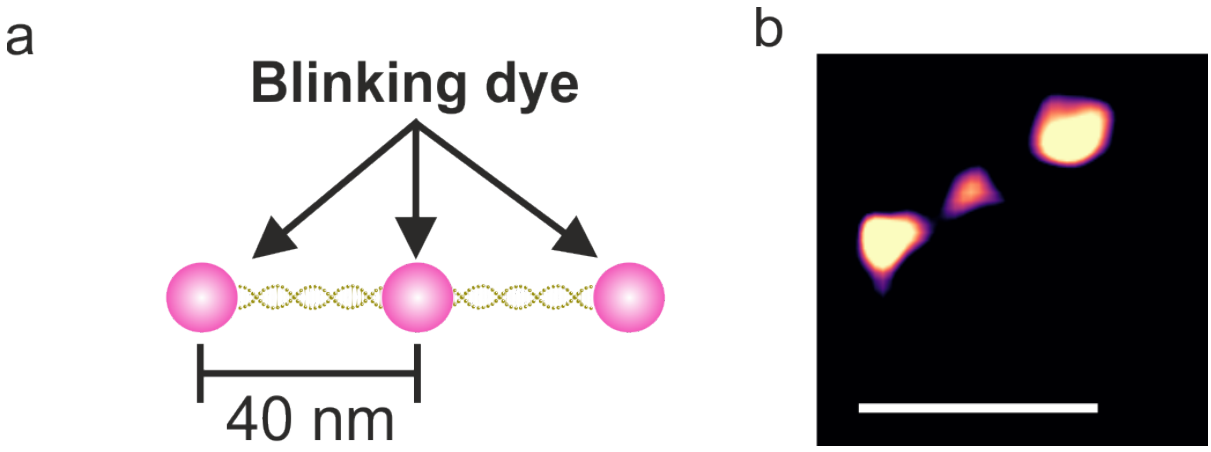

Figure 57: dSTORM imaging of the nanoruler®
(a), Scheme of the GATTA-PAINT 40 nm nanoruler® construct used for calibration and validation of the microscopy settings for dSTORM. The single fluorophores are separated by 40 nm DNA origami.
(b), Representative dSTORM image of the nanoruler construct illustrated in (a). White scalebar is 80 nm

Based on the analysis of the localization density per spot, it was found that the unstimulated wildtype receptor showed – as in the single-molecule experiments with live cells – an essentially strictly monomeric behavior (**Figure 58**, top panels), whereas the T279K mutant revealed rather spots of double intensity (**Figure 58**, lower panels). These spots of double intensity could not be resolved, suggesting that the two protomers of the T279K mutant were much closer to each other than 40 nm.

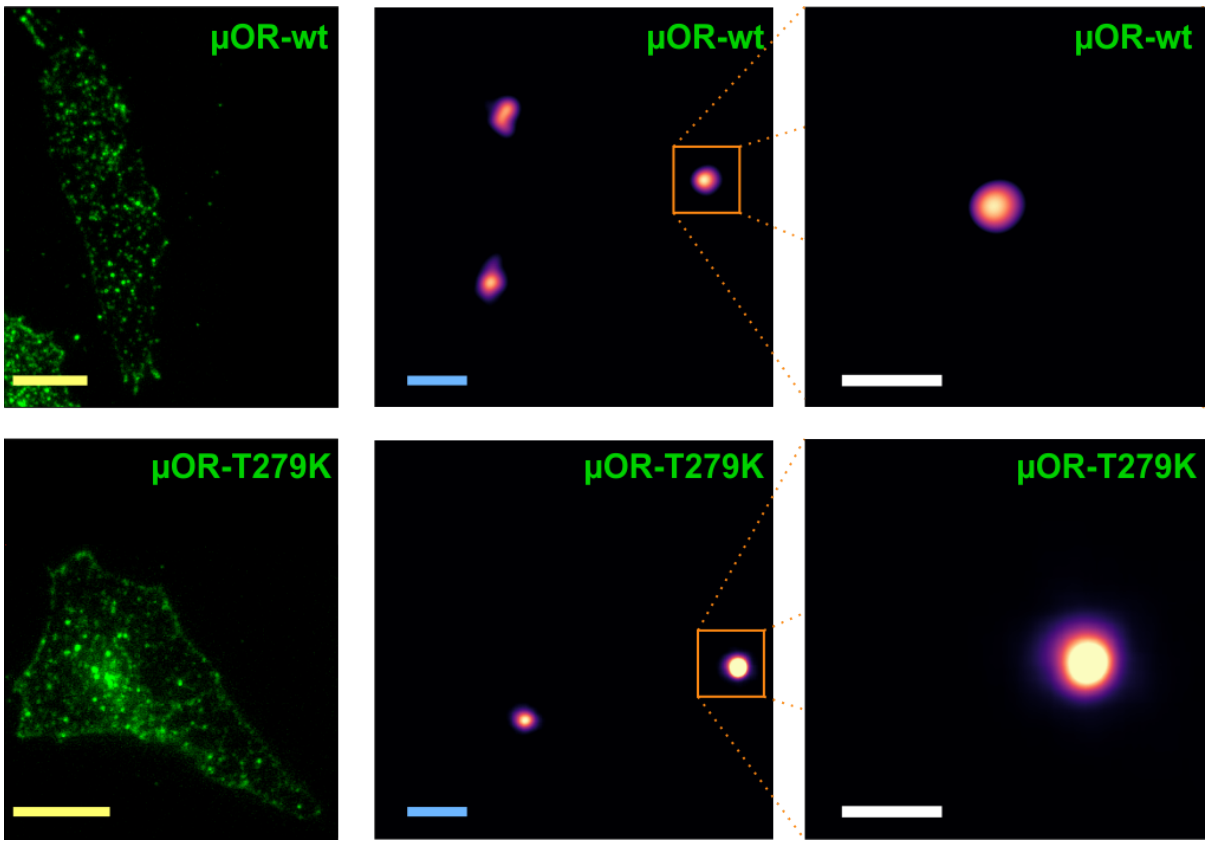

Figure 58: dSTORM images of μOR wildtype and constitutively active T279K mutant
Left panels: Representative diffraction limited images of fixed CHO cells expressing wildtype μOR or its T279K mutant, labeled with Alexa-Fluor 647 (receptors in green). Center panels: Close-ups of the cells shown in the left panel (center and right panels receptors in the Fiji color-code mpl-magma). Right panels: Close-up images of the center-panels showing that double-intensity (dimeric) spots of the T279K mutant could not be resolved as individual receptor protomers, indicating that the distance between them is below 40nm. Scale bars are: yellow= 10 μm, blue = 200 nm, white = 80 nm. Images of each condition are representative of five independent experiments.

Very similar images were obtained for the wildtype μOR in the presence of 10μM DAMGO (**Figure 59**). Taken together, these results provide further evidence for the existence of dimers of the μOR in the active state, induced by either DAMGO or the T279K mutation, where in both cases the distance between protomers appears to be below 40 nm.

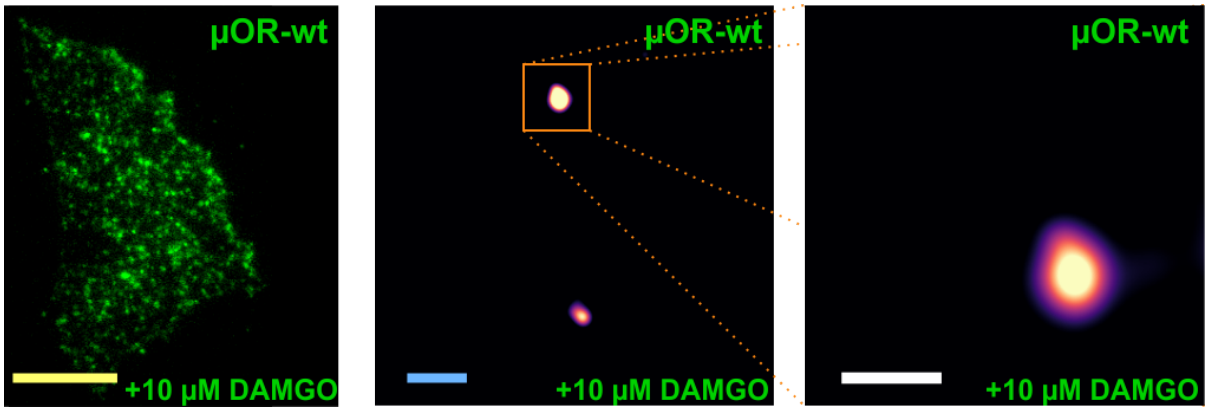

Figure 59: dSTORM images of μOR when treated with 10 μM DAMGO before cell fixation
*Left panel: As in **Figure 58** representative diffraction limited image of fixed CHO cells expressing wildtype μOR, but treated with 10 μM DAMGO for 15 minutes before cell fixation, labeled with Alexa-Fluor 647 (receptors in green). Center panel: Close-up of the cell shown in the left panel. Right panel: Close-up image of the center-panel showing that double-intensity (dimeric) spots of wildtype μOR after DAMGO treatment could not be resolved as individual receptor protomers, as well indicating that the distance between them is below 40 nm. Scale bars are: yellow = 10 μm, blue = 200 nm, white = 80 nm. Images of each condition are representative of five independent experiments.*

3.4.2. Quantitative dSTORM confirms receptor stoichiometry

Single-molecule localization microscopy (SMLM) generates super-resolved images from single emitters that are operated as photoswitches[142], and provides direct access to molecular numbers of these fluorophores[204]. The intrinsic kinetic information of photo switching can be used to determine the number of emitters in a super-resolved spot by analyzing the distribution of blinking events[153,174,205]. To verify the single-molecule and dSTORM measurements and moreover to precisely quantify the stoichiometry of the μOR and its dimeric T279K mutant, collaborators from the Lab of Mike Heilemann conducted dSTORM imaging experiments with their microscope and analyzed the blinking distributions in single receptor spots. Oligomeric spots show an increase in the number of blinking events in contrast to monomers, which is essentially depending on the higher number of fluorophores. In **Figure 60**-**Figure 62** super-resolved and brightfield (inset) images as well as corresponding histograms of the number of blinking events for Alexa Fluor 647® conjugated via SNAP-tag to the respective protein are shown. The blinking histogram was fitted with theoretical model functions reporting on monomer and dimer populations as further described in the methods section. In line with the previous measurements, this technique confirmed the monomeric and dimeric nature of the controls, β_1AR and CD28 (**Figure 60**).

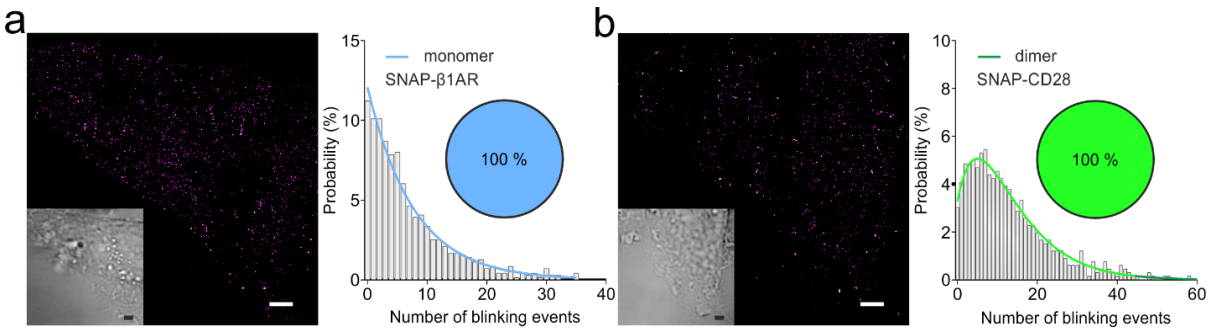

Figure 60: Quantitative dSTORM of the controls
SNAP-β_1AR (a) and SNAP-CD28 (b) serve as calibration standards for monomeric and dimeric proteins, which allows robust extraction of analysis parameters. Analysis reveals 100 ± 3 % monomers for SNAP-β_1AR and 100 ± 3 % dimers for SNAP-CD28. Data are mean ± SD. In total 714 spots for SNAP-β1AR and 661 spots for SNAP-CD28 were analyzed. For both controls, n = 12 cells from three independent experiments were analyzed.

The wildtype μOR was again identified as strictly monomeric (100 ± 3 %) (**Figure 61a**), whereas the constitutively active T279K mutant was composed of just 17 % monomers and 83 ± 2 % dimers (**Figure 61b**).

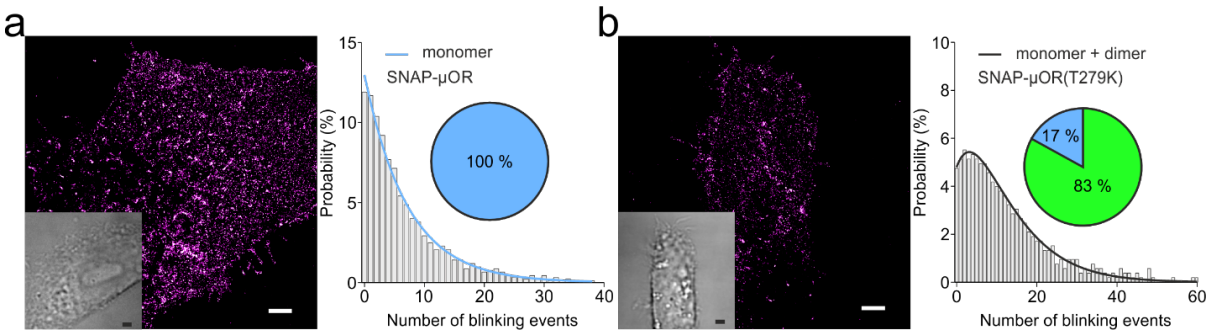

Figure 61: Quantitative dSTORM of the wildtype μOR and T279K mutant
For the wildtype μOR (a) analysis reveals 100 ± 3 % monomers (as for SNAP-β_1AR) and for SNAP-μOR (T279K) (b) 17 ± 2 % monomers with 83 ± 2 % dimers. Data are mean ± SD In total n = 925 spots for SNAP-μOR and n = 526 spots for SNAP-μOR (T279K) were analyzed. For both, at least ten cells from three independent experiments were analyzed.

Wildtype μORs after 10 min of DAMGO stimulation had only 50 ± 2 % monomers (**Figure 62a**), and after 15 min of DAMGO stimulation the monomers represented only 13 ± 2 % of the total receptor population (**Figure 62b**). This confirms again that both, DAMGO stimulation and the constitutively active T279K mutation, induce formation of μOR dimers.

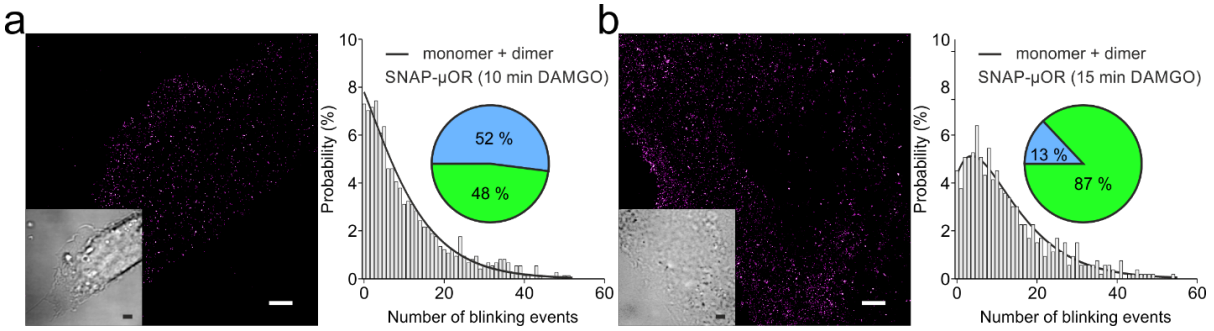

Figure 62: Quantitative dSTORM of the wildtype μOR after receptor activation with 10 μM DAMGO
When the receptors are activated with 10 μM DAMGO before cell fixation the analysis reveals for 10 minutes of stimulation (a) 52 ± 2 % monomers with 48 ± 2 % dimers and for 15 minutes (b) 13 ± 3 % monomers with 87 ± 3 % dimers. Data are mean ± SD In total n = 589 spots for SNAP-μOR (10 min DAMGO) and n = 601 spots for SNAP-μOR (15 min DAMGO) were analyzed. For each condition, at least ten cells from three independent experiments were analyzed.

Such quantitative analysis of photokinetic data goes beyond the spatial resolution of super-resolution SMLM and reports on molecule numbers in single protein complexes[204,205], supporting further the dimeric character of the μOR when either constitutively actively mutated (T279K) or activated by DAMGO.

3.5. β-arrestin2 recruitment but not receptor activation correlates with μ-opioid receptor dimerization

To analyze which steps of signal transmission might be correlated with the dimerization-related observations, the kinetics of receptor activation and β-arrestin recruitment were measured. Since activation of GPCRs can occur on a millisecond timescale[206], this step was measured by using ligand superfusion of single cells expressing a μOR sensor construct that bears a cpGFP in its 3rd intracellular loop[134]. In this for GPCRs relatively new sensor concept the conformational changes during receptor activation, most prominently the outward movement of TM6, are transduced via specialized linkers to the inserted conformational sensitive cpGFP, leading to reconstitution of the GFP barrel and an immediate increase of its fluorescence intensity (more detailed shown in 3.6). Similar to many other class A GPCRs[207], μOR activation by DAMGO is complete within less than a second after agonist activation (τ= 96 ±18 ms) (**Figure 63a**).

This result correlates temporally with the initial increased diffusion speed of the receptor, measured up to 1 minute after agonist treatment, rather than with μOR dimerization (**Figure 47**).

In contrast, recruitment of β-arrestin2 by μORs, measured using BRET between the two proteins, occurred with kinetics in the minutes range (τ = 2.8 ± 0.24 min). This time-course correlates quite well with the time-course that I observed for dimerization, which also occurred over several minutes (**Figure 63b**), and also rather with the slow decrease of diffusion over 15 minutes than its brief 1-min increase (**Figure 47**).

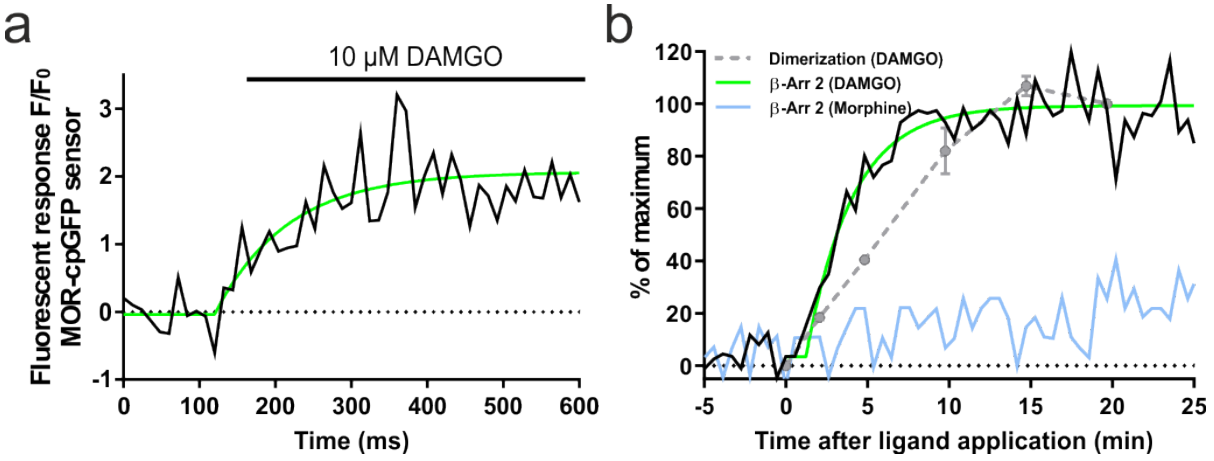

Figure 63: Kinetics of receptor activation and β-arrestin2 recruitment
(a), μOR activation by fast superfusion with 10 μM DAMGO is complete within 300ms (τ= 96 ± 18 ms).
(b), DAMGO-induced dimerization of the μOR in single-molecule experiments (dashed line) follows a comparable time-course as β-arrestin2 recruitment (τ=2.8 ± 0.24 min) in platereader-based BRET experiments. Morphine does not increase the dimerization and the β-arrestin2 recruitment is low.
Shown experiments were repeated independently n = 3 times on three different experimental days.

Moreover, the EC_{50}-values for β-arrestin2 recruitment after DAMGO addition correlated quite precisely with those of the BRET-increase measured between two C-terminally tagged receptor protomers of the μOR (**Figure 64**).

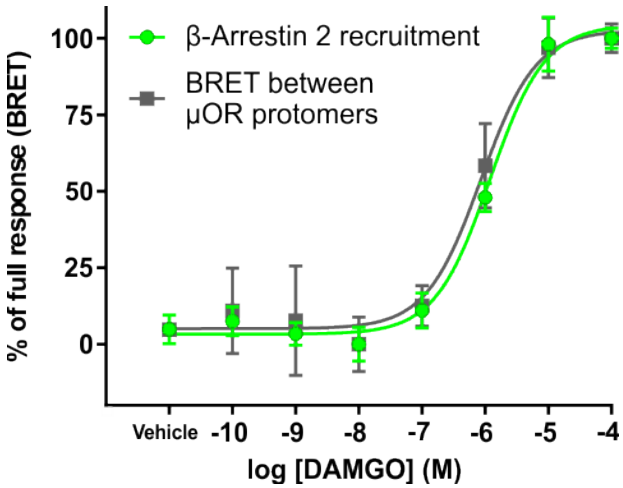

Figure 64: DAMGO concentration dependence *Shown are platerader assay-based concentration response curves. The BRET increase by recruitment of β-arrestin2 (pEC_{50} = 5.9 ± 0.1) to the μOR and the BRET increase between μOR protomers (pEC_{50} = 6.1 ± 0.3) upon DAMGO stimulation show comparable concentration dependencies. Shown experiments were repeated independently n = 3 times on three different experimental days.*

Interestingly, the merge/split analysis of single-particle tracks showed that the dimer-lifetimes measured for the μOR activated by 10 μM DAMGO (**Figure 65**) were not significantly longer than those of the wildtype receptor (**Figure 45**). This suggests that the active-state dimer has a long lifespan (quasi-constitutive) and therefore no complete sequences of dimerization/split-events of this interface could be observed within individual tracks (see **Figure 44**).

Constitutive dimer interfaces cannot be analyzed in this regard since the kinetic analysis requires merge and split events of individual receptor tracks. In other words, constitutive dimers do not display dimerization kinetics in single-particle tracking analyses, since the protomers stay together throughout the entire imaging sequence. The observed dimerization kinetics are therefore possibly occurring on a similar interface as those of the unstimulated receptor, a situation which would then also allow the occurrence of short-lived tetramers, an arrangement which has also been shown for crystallographic results[34] .

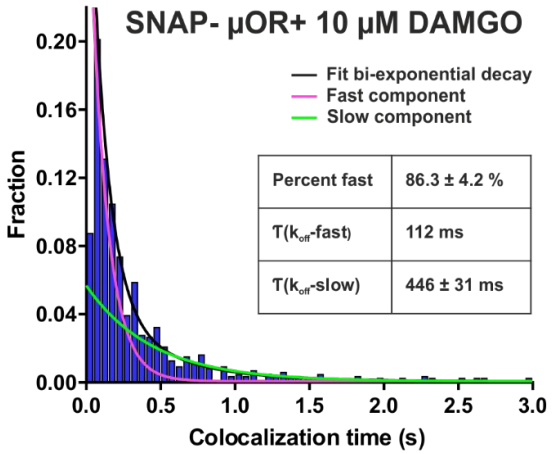

Figure 65: Analysis of colocalization times after receptor activation by 10 μM DAMGO
*Distribution of colocalization times derived from tracks as shown in **Figure 45** reveals that the dimerization kinetics of the μOR activated by 10 μM DAMGO (τ = 422 ± 30 ms) is not significantly different from the untreated receptor, suggesting that the observed dimer is quasi-constitutive. Data are τ value and 95% CI on the basis of n = 870 tracks containing merging events from 29 cells and three independent experimental days.*

Since a stable TM5-TM6 interface is not compatible with the active state of the receptor due to steric reasons[35], I suggest that the dimer observed by us may be mediated by the TM1-TM2-H8 interface, which was also observed in the crystal structures and agrees with an active state[34,35] and might even be stabilized by β-arrestin2 (**Figure 66**).

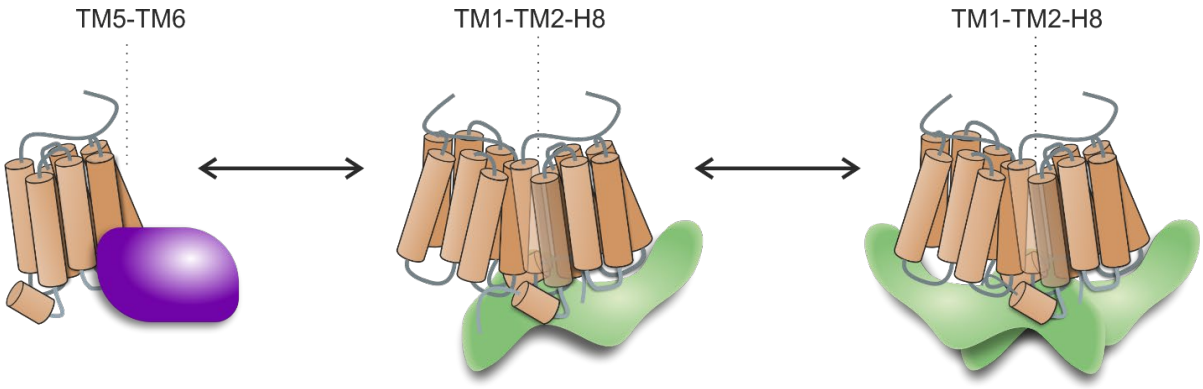

Figure 66: Hypothetical model of beta-arrestin supported receptor dimerization
Hypothetical model of a μOR dimer mediated via the TM1-TM2-H8 interface, which might be eventually stabilized by β-arrestin2 (purple= G protein; green= β-arrestin2).

Involvement of β-arrestin(s) in μOR dimer formation is supported by the observation that the phosphorylation-deficient variant of the constitutively active T279K mutant did not form dimers as revealed by intensity analysis (**Figure 53**, **Figure 67a**) and bleaching kinetics (**Figure 67b**).

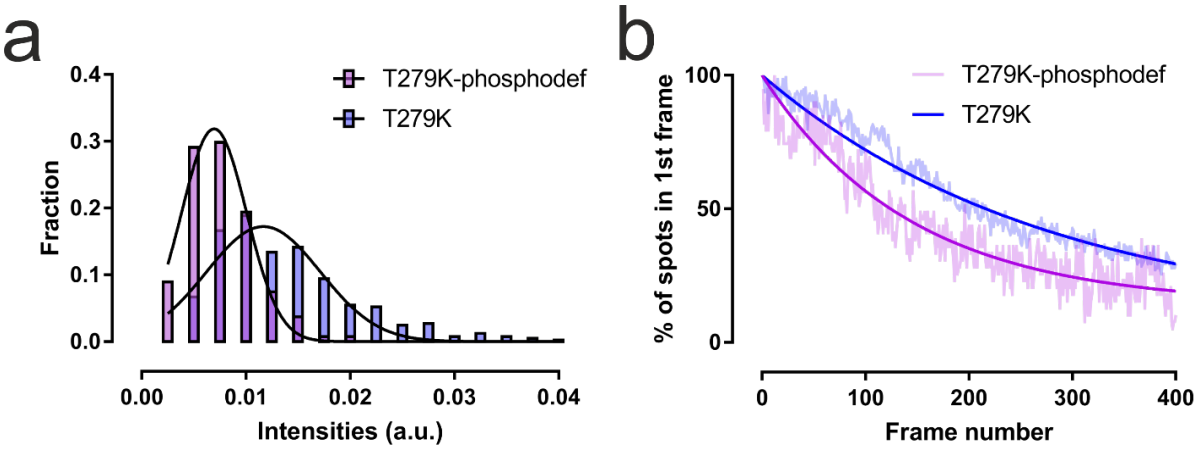

Figure 67: Oligomeric state of the phosphorylation deficient constitutively active T279K mutant
(a), Intensity histograms of the dimeric T279K mutant and its phosphorylation-deficient modification. The phosphorylation-deficient modified mutant shows a monomeric distribution of intensities. (b), Bleaching experiments over 400 frames (sampling-rate= 40 ms) and high laser-power reveal an almost exactly doubled half-life time for the unmodified T279K mutant (8.9 ± 0.3 s) in contrast to its phosphorylation-deficient modification. (4.5 ± 0.2 s). Data in (a) were generated from 347 (T279K-pd) and 287 (T279K) detected PSFs from n = 5 cells tested on three different experimental days. (b) shows a representative bleaching trace over 400 frames extracted from datasets acquired in (a).

Furthermore, I showed above (**Figure 53a**) that dimerization of the T279K mutant is essentials abolished, when pretreated with the GRK inhibitor Cmpd101. To further underline the connection between dimerization and β-arrestin(s) I compared β-arrestin2 recruitment of the T279K mutant before and after treatment with the GRK- inhibitor Cmpd101 (**Figure 68**).

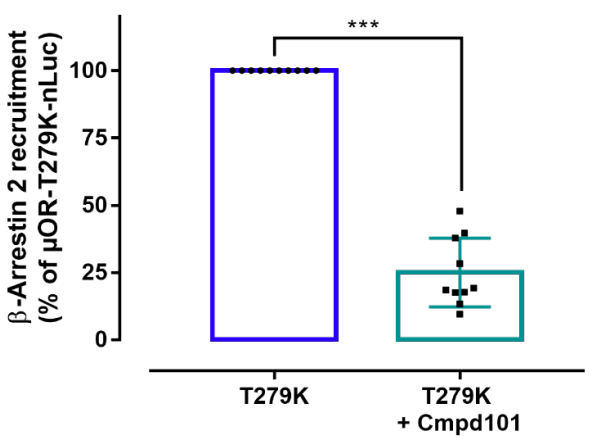

Figure 68: β-arrestin2 recruitment by the T279K mutant after treatment with Cmpd101
Platereader-based BRET measurements between the T279K mutant and β-arrestin2 before and after treatment with the GRK inhibitor Cmpd101. Treated cells show 26.5 ± 2.1 % β-arrestin2 recruitment relative to the untreated T279K mutant. Shown data points are percentages of BRET-ratios normalized to the untreated T279K mutant. Data are mean ± SD and were generated from n = 2 independent experiments.

Overall, these data reveal that GRK-dependent phosphorylation appears to be a minimal requirement for μOR dimerization, and that this effect might precede but is distinct from μOR internalization.

3.6. Optimization of the cp-GFP based μOR-sensor to investigate receptor- crosstalk

The cpGFP based μOR[134] sensor shown in (**Figure 63a**) was sufficient to measure activation kinetics of the μOR. Unfortunately, the amplitude of the sensor was not adequate to measure reliably allosteric effects as for example mediated by receptor crosstalk. In a previous study of our lab it could be shown, using a FRET-based sensor of the α_{2A}-adrenoceptor (α_{2A}AR), that the μOR activated by morphine has negative allosteric effects on the α_{2A}AR[41]. Due to severe difficulties of generating a FRET-based sensor of the μOR, the question remained open if the receptor crosstalk might also occur vice versa from the α_{2A}AR towards the μOR.

To enhance the cell surface expression of the published cpGFP based μOR sensor[134], the sensor was optimized with a combination of several strategies shown before for other membrane proteins[208] (**Figure 69a**). N-terminally an Igκ-leader sequence was inserted, which is cleaved off by a signal peptide peptidase after crossing the ER membrane[209] and enhances the direction of the protein to secretory pathways[210,211]. Additionally, a membrane targeting sequence derived from the Kir2.1 ion channel (KSRITSEGEYIPLDQIDINV)[208], spaced by a triplet of an inert (Gly_4-Ser)-linker, was inserted at the C-terminal end. Moreover, to prevent ER aggregation[208], C-terminally from this sequence another triplet of the (Gly_4-Ser)-linker, followed by another Kir2.1 derived sequence (FCEYENEV) was inserted. Finally, the transmembrane domains of the sensor were exchanged with those from the crystal structure construct of the μOR.

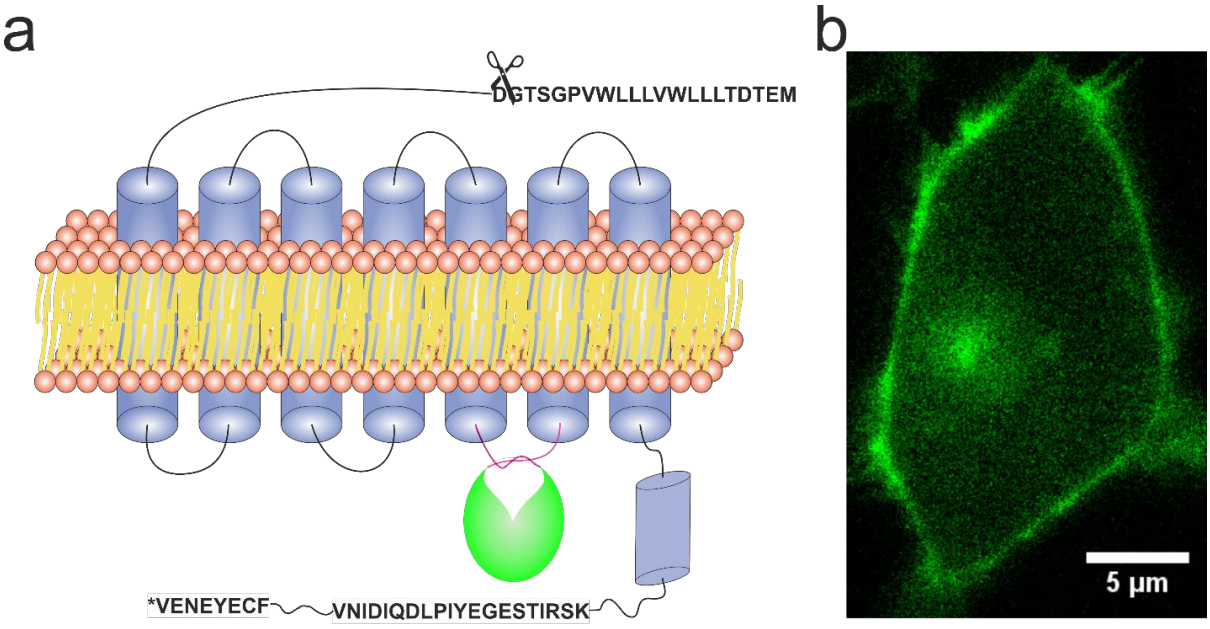

Figure 69: MOR-cpGFP sensor optimization
a), In the sensor concept, previously published by others, the ICL3 of the GPCR got replaced by cpGFP implemented between two special- designed linkers (magenta), which allow a closure of the GFP- barrel due to TM6 outward movement (here just illustrated with a knot).Cell surface expression was improved by us due to a combination of different signaling sequences. The N- terminal Igκ sequence is cleaved by a signal peptide peptidase after surpassing the ER. Sequences on the C- terminal end are separated by triplets of GGGGS linkers.
b) Widefield epifluorescence image to show membrane localization of the optimized sensor.

This sensor showed not just significantly improved cell surface expression (**Figure 69b**), but also an increased and more robust response to perfusion with agonists (see **Figure 82**).

4. Discussion and Outlook

In this work I used single- molecule TIRF microscopy to elucidate the membrane organization, especially dimerization of the μOR as well as the dynamics of such individual receptors on the surface of live cells. I combined single-particle tracking of individual receptors with the super- resolution method dSTORM to investigate μORs down to a nanoscopic level. To understand the kinetics of receptor dimerization I furthermore acquired single- molecule movies with high temporal resolution of 100 frames per second (fps). These experiments revealed with single-molecule approaches an unforeseen effect of agonist-specific receptor regulation due to changed receptor mobility as well as dimer formation of the μOR. To furthermore validate the results over a comprehensive range of expression levels, this work combined single-molecule methods with molecular brightness and FRET-AB measurements.

In line with single-molecule studies conducted on other GPCRs[28,212], also in combination with their cognate G proteins[126], the μOR can likewise undergo different types of diffusion and tends to compartmentalize on the cell surface. Based on the obtained results the compartmentalization is presumably to a large extent caused by actin fibers, which create diffusion barriers underneath the plasma membrane. Activation of the μOR by DAMGO or morphine increases initially the mobility of the receptors due to an increased diffusion speed, an effect which is in line with a very recent observation[213] and applies to all mobile diffusion fractions. Furthermore, a higher number of μORs undergo during this initial time-period crossing-events over the actin fibers. This increased mobility after receptor activation might contribute to the fast signal propagation in neurotransmitter receptors[213–215], as it would allow the μOR to interact more frequently with its signaling partners - a concept for controlling their spatiotemporal distribution and signaling[59,73,212]. Interestingly, this effect is most pronounced for the sub-population of receptors, which undergoes directed diffusion, suggesting that certain receptors move along “signaling highways” parallel to cytoskeletal structures, as for instance, actin. A physiological setting which supports this concept could be the regulation of responsiveness in a postsynaptic neuron, after neurotransmitter release from the presynaptic neuron, via receptor re-arrangement on the cell surface[216–218]. In contrast, the decreased diffusion speed of μORs as well as a lower number of actin crossing events at later time points supports a mechanism of signal termination by decreased receptor mobility. An experimental observation which further supports this mechanism is the severely reduced diffusion coefficient caused by the irreversibly binding antagonist β-FNA.

In our investigations on the molecular organization of the μOR (e.g. receptor stoichiometry/oligomerization) a range of expression levels reaching from 0.1 receptors/μm^2 in single-molecule intensity analyses, to ≈10 receptors/μm^2 in quantitative dSTORM, and up to ≈ 50 - 100 receptors/μm^2 in molecular brightness, and FRET-AB measurements was covered. Over the whole range of expression levels, a predominantly monomeric constitution of the μOR was observed. Actually, even a more monomeric behavior than the largely monomeric β_1ARs[29,157] and CD86, which several studies used as a reference for a monomeric membrane protein[156,219]. In agreement with molecular dynamics simulations from the collaborating Filizola Lab[157], the low amount of μOR dimers, captured in single-molecule tracking experiments, were very transient and of short lifetime. These interaction lifetimes were remarkably shorter than those measured before among β_1ARs[29] or between α_{2A}ARs and

their cognate G proteins[126]. They further contrast with the apparently long-lived functional dimer which the μOR is forming with the α_{2A}AR[41,220], suggesting that the few, highly transient homodimers as formed by the μOR under basal conditions are presumably not comprising a functional consequence for G protein mediated signaling[221]. This doubt is strengthened by studies which showed for prototypical class A receptors that activation of a single monomeric receptor is sufficient to activate G proteins[22,222,223].

However, receptor stimulation with DAMGO led to a progressive increase of μOR dimer formation and the constitutively T279K mutant appeared in the corresponding experiments as a long-lived dimer, maybe even constitutive. Remarkably, the agonist effect of dimerization was limited to DAMGO and did not occur when the receptor was activated by morphine. This adds up to the notion of distinct activation mechanisms that these two ligands might trigger. In particular DAMGO, but not morphine, causes β-arrestin2 recruitment followed by receptor internalization as well as β-arrestin-mediated signaling[188,224].

Focusing on the individual kinetics I observed a time-course for β-arrestin2 recruitment matching with that of μOR dimerization, whereas receptor activation occurred much faster. Additionally, the ligand concentrations for β-arrestin2 recruitment were very similar to those which led to receptor dimerization, raising the probability that the two processes might be associated with each other. This hypothesis is further supported by the experiments with the phosphorylation-deficient variant[191,198] of the μOR, which dimerized neither upon DAMGO application nor due to T279K mutation. Furthermore, treatment with the GRK inhibitor Cmpd101 abolished receptor dimerization of the T279K mutant. Such a scenario could link agonist bias with dimerization, since a β-arrestin biased agonist recruits β-arrestin and in turn β-arrestin strengthens receptor dimerization. This would allow the formation of a complex which executes β-arrestin-mediated signaling from the membrane, before the receptor undergoes internalization and signaling gets terminated.

Comparison of the existing structures of other class A GPCRs together with arrestins[225–227] would sterically allow a scenario in which two receptors can form a dimer in complex with arrestin. Both arrestin orientations observed in these structures would be compatible with an active state μOR dimer at the TM1/TM2/H8 interface. Although it seems to be sterically possible for such a dimer to bind to two arrestins simultaneously and although there is some structural evidence for active β-arrestin2 to form dimers[228,229], more physiological scenarios with other arrestins have been described, in which a receptor dimer binds to a single arrestin[230–232].

Even though β-arrestin2 appears to be involved in both processes and although they are both triggered by DAMGO but not morphine, several lines of experimental evidence in this work indicate that dimer formation and internalization of μORs are distinct processes: (**a**), The number of protomers does not exceed two per resolved spot, neither in intensity based measurements nor in dSTORM experiments, where the number of fluorophores is correlated with the blinking frequency of fluorophores (in contrast, internalized receptors occur in groups up to 10 per spot). (**b**), Dual-color imaging shows that there is no overlap with clathrin clusters. (**c**), Super-resolution microscopy indicates a distance between protomers of well below 40 nm (**Figure 57**-**Figure 59**) and maybe even less (**Figure 60**-**Figure 62**), respectively. Since for early endosomes diameters of 400-600 nm have been reported[233,234], one would expect larger

distances of receptor protomers in such structures as well as a rather clustered distribution of the individual fluorophores within such a diameter. (**d**), The diffusion pattern of the dimers is similar to the one of monomeric receptors and clearly not confined as one would expect for internalized receptors. (**e**), the kinetics of dimerization are faster than those measured for receptor internalization.
However, since I was able to see, after longer stimulation with DAMGO, combined with a deeper penetration depth of the TIRF-laser, receptor clusters that co-localized with clathrin, the obtained data suggests the possibility of a sequence of events, where dimerization of μORs precedes their internalization.

Thus, signaling by μORs appears to be subject to complex supramolecular regulatory mechanisms, which include their spatiotemporal organization as well as receptor/receptor interactions. The obtained data show that GPCR dimerization and β-arrestin2 recruitment may be intricately linked, revealing that dimerization can be a dynamic and even agonist-specific process. Finally, these complex mechanisms may offer new ways of interfering with μOR signaling for example by testing the TM1-TM2-H8 interface as an allosteric drug target to enable a more precise fine-tuning of μOR signaling.

New chemical entities might be capable of disrupting μOR dimers and thereby lead to a reduction of β-arrestin mediated signaling in a tissue-specific manner. This optimistic thought might allow, if further evidence can be raised, to achieve by individual or combined targeting of the TM1-TM2-H8 interface a reduction of opioid side effects in certain tissues. For now, the challenge of an improved opioid therapy remains open until future research shows a successful opioid analgesia with minimized potential of addiction and a reduced series of undesired side effects and interaction potentials.

Since the question is not sufficiently adressed yet, how many β-arrestin2 protomers are involved in the formation of the described dimeric μOR complex, a logical consequence for further investigations are single-molecule experiments on β-arrestin2 after μOR activation. Initial experiments with a Halo-tagged β-arrestin2 construct unveiled several obstacles for such experiments.

The first issue is that β-arrestins are, in contrast to G proteins, due to a missing lipid anchor, not constitutively localized on the cell membrane. Following, I saw an increased recruitment to the membrane after receptor activation, but those appearances of β-arrestin2 were very transient and disappeared quickly from the evanescent field, making reliable intensity comparisons for an estimate of complex stoichiometry impossible. The second issue in such experiments is that endogenous β-arrestins of the used CHO cells are quite abundantly expressed, presumably way higher than the at low single-molecule level expressed Halo-tagged β-arrestin2 construct. Therefore, the likelihood of the labeled β-arrestin2 to interact with the receptor complex is severely reduced, to a level that almost no receptor-β-arrestin2 interactions can be observed. A further point which leaves room for optimization in such single-molecule experiments is the labeling efficiency for intracellular labeling and the minimization of background, resulting from insufficient wash-out of the used dye.

Therefore, our lab started initiatives for optimization and got hands on a recently published β-arrestin1/β-arrestin2 double KO CHO cell line that was created using the CRISPR-Cas9 technology[235].

Additionally, I created a membrane-tethered β-arrestin2 construct (**Figure 70a**), which showed a higher basal BRET-ratio and a higher upper plateau, but no markedly altered EC_{50}-value in β-arrestin2 recruitment assays, compared with the non-tethered construct (**Figure 70b**). Just very recently I also substituted the Halo-tag in this construct with mNeonGreen, which is so far the only fluorescent protein, which showed in my hands enough photostability for single-particle tracking over a few hundred frames (up to 200). I am hoping with this exchange to trade in the reduced photostability for a higher intracellular labeling efficiency and diminished background.

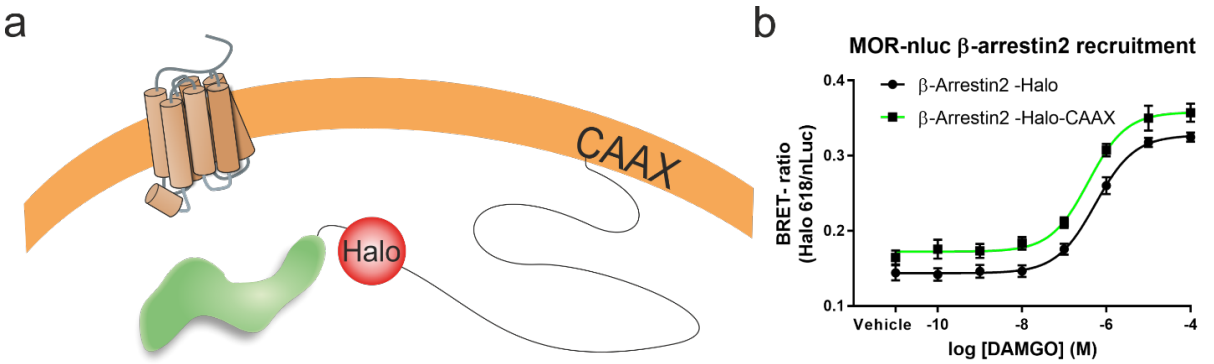

Figure 70: Membrane-tethered β-Arrestin2
a), The illustrated membrane-tethered construct contains after the C-terminal Halo-tag a repetitive sequence of 21 GGGGS-linkers followed by H-Ras derived CAAX box (GCMSCKCVLS) for with single-molecule imaging compatible membrane anchoring[236].
b), The membrane-tethered construct shows a higher basal ratio and reaches a higher upper plateau, whereas pEC_{50} values of the construct (-6.43 ± 0.09) were not markedly different from the non-tethered construct (-6.26 ± 0.12).

Obviously, these modifications distance the experiments further from a physiological setting, but I hope that they are still sufficient to get a mechanistic insight into the stoichiometry and function of β-arrestin2 in the dimeric complex, which was observed for the μOR.

A deeper understanding of the constitution and function of such a complex might also facilitate the above discussed research on an allosteric targeting of the μOR, which might ultimately help for the development of safer opioid therapeutics - a scientific issue which will for sure keep challenging for several more years but can probably just be improved ever if addressed by adequate research on the molecular understanding of the μOR.

5. Summary

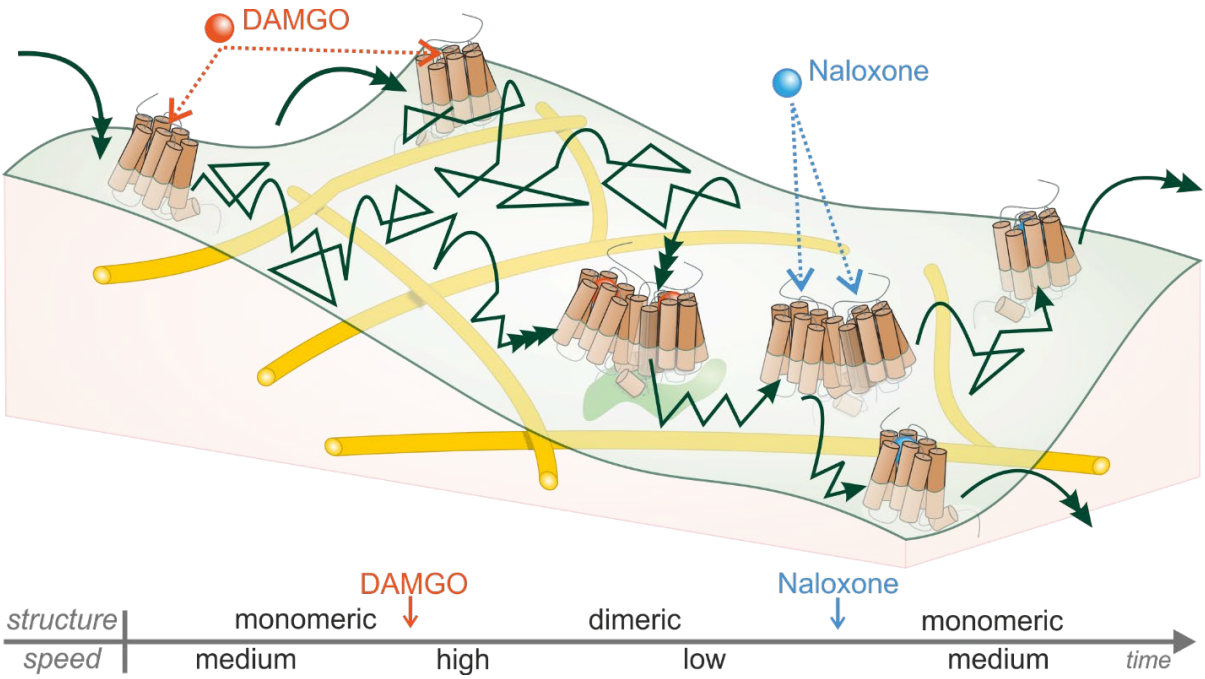

Figure 71: Graphical summary
The μOR is displays a certain compartmentalization by cytoskeleton structures, gains mobility subsequently after activation and is simultaneously more often crossing such actin-fibers. Later on in time, matching with β-arrestin recruitment, the receptor can form a long-lived dimer which is significantly reduced in its mobility. The dimer can be broken by antagonist application and thereby basal receptor dynamics are restored.

Being the prime target for the treatment of severe pain, activation of the μOR is responsible for a latter of undesired side effects as respiratory depression, constipation and drug-dependence. To support medicinal chemists in drug development, the understanding of the molecular function and activation vs. deactivation mechanism of the μOR gained increasing importance. The most prominent downstream signaling partners of the μOR are G_i proteins, and subsequent to GRK-mediated phosphorylation, β-arrestin2. Most recent structure-based efforts to design safer opioid analgesics were focused on the generation of biased agonists with a high selectivity for G_i protein mediated signaling to surpass side-effects caused by β-arrestin[237]. Indeed, it has been shown, using knock-in mice with phosphorylation-deficient μORs, that analgesic effects were improved and tolerance development was reduced when the receptor was biased to G protein. Unexpectedly, the other side-effects,such as respiratory depression, constipation and opioid withdrawal, seemed to be worsened by this[238]. An attempt to explain this ongoing issue during the development of safer opioid-analgesics is based on the lower efficacy of these G protein biased compounds[239]. However, it is so far poorly understood if, how and under which circumstances dimerization of the μOR occurs and whether it shows potential for shaping the described signaling profile of these receptors.

Here I show that the μOR is underlying a certain compartmentalization on the cell surface and that its mobility is changed by receptor activation. Furthermore, I observed the agonist-specific formation of a dimer equilibrium in correlation with β-arrestin2 recruitment. Using single-molecule microscopy, I tracked individual μORs on the surface of living cells and revealed that actin fibers serve as diffusion

barriers, contributing to the compartmentalization of μORs. Receptor activation partially dissolves this compartmentalization and leads to an increased diffusion speed of μORs, and thereby an increased percentage of receptors can overcome actin fibers. However, at later time points receptor compartmentalization increased and in parallel, for μORs activated by DAMGO, dimer formation as well as β-arrestin recruitment occurred.

Results with different inhibitors and mutations demonstrated how μOR activation, by a β-arrestin biased ligand, is related to a dimer formation that is reversible by antagonist application and distinct from receptor clustering that precedes internalization. I anticipate that these findings have potential for the development of safer opioid drugs. For example, by addressing the dimeric interface as potential allosteric target to decrease receptor dimerization and thereby alleviating β-arrestin signaling without completely abolishing it. The individual and combined targeting of orthosteric and allosteric sites (possibly at the TM1-TM2-H8 Interface) of the μOR could be tested and might allow a more concise fine-tuning of μOR agonists. Furthermore, since different tissues contain deviating cytoskeleton structures, the involvement of the cytoskeleton on receptor compartmentalization, localized signaling and receptor re-arrangement on the cell surface might help to understand different tissue specific effects, side effects as well as interaction potentials of the μOR.

6. Zusammenfassung

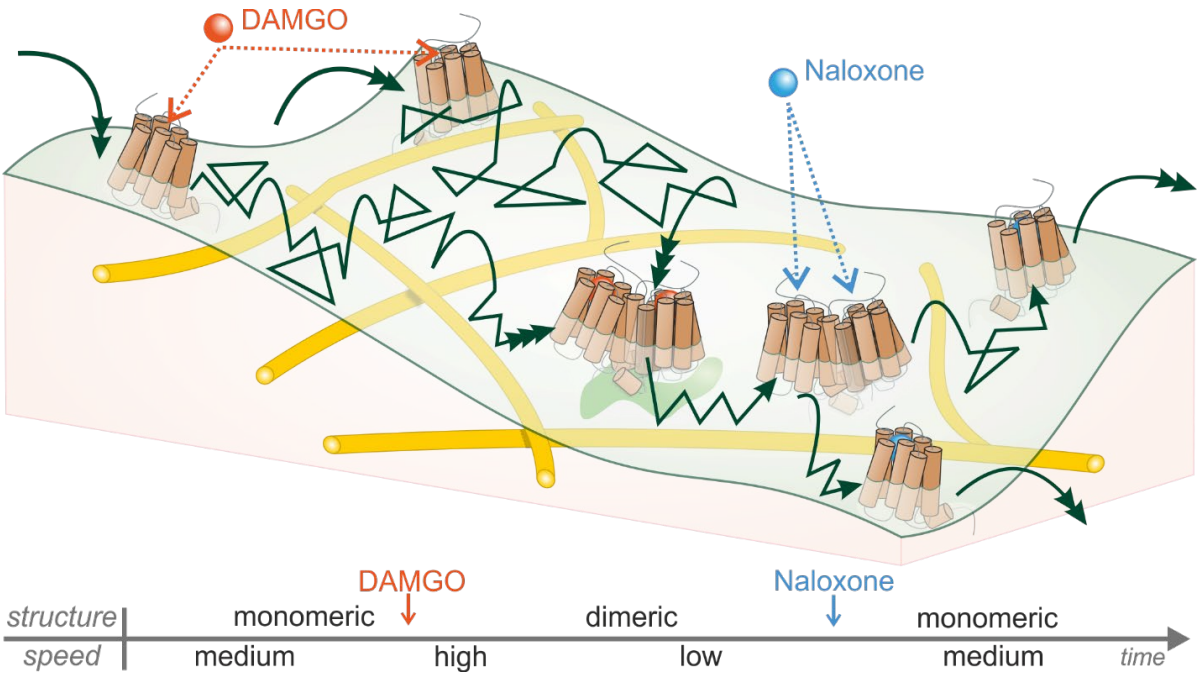

Figure 72: Graphische Zusammenfassung
Der μ-Opioid-Rezeptor unterliegt durch Strukturelemente des Cytoskeletts einer bestimmten Kompartmentalisierung auf der Zelloberfläche. Zudem ist seine Mobilität unmittelbar nach der Rezeptoraktivierung erhöht und Strukturen des Cytoskeletts wie Aktin-Filamente werden häufiger vom Rezeptor überwunden. Zu späteren Zeitpunkten, übereinstimmend mit β-Arrestin Rekrutierung, bildet der Rezeptor ein langlebiges Dimer, das erheblich in seiner Mobilität eingeschränkt ist. Dieses Dimer kann durch Zugabe von Antagonisten wieder in den monomerischen Rezeptorzustand überführt werden, wobei die dynamischen Eigenschaften des monomerischen Rezeptors wiederhergestellt werden.

Abgesehen davon, dass der μ-Opioid-Rezeptor das primäre Zielprotein zur Behandlung schwerer Schmerzen ist, führt die Aktivierung dieses Rezeptors zu einer Reihe von unerwünschten Nebenwirkungen wie Atemdepression, Obstipation und Drogenabhängigkeit. Um die medizinischen Chemiker bei der Entwicklung neuer Arzneistoffe zu unterstützen, ist das Verständnis der molekularen Funktion insbesondere der Aktivierungs- und Deaktivierungsmechanismen des μ-Opioid-Rezeptors von voranschreitender Bedeutung. Die prominentesten Signalpartner des μ-Opioid-Rezeptors sind G-Proteine des Typs Gi, sowie nach vorheriger Phosphorylierung durch G-Protein-gekoppelte Rezeptorkinasen, β-Arrestin2. Die neusten strukturbasierten Bemühungen zur Entwicklung sicherer Opioid-Schmerzmittel waren auf die Herstellung von Signal-selektiven konzentriert, die eine hohe Präferenz für G-Protein-Signalwege aufweisen und somit die β-Arrestin-vermittelten Nebenwirkungen umgehen sollen. In der Tat konnte, durch Knock-in-Mäuse mit phosphorylierungs-defizienten μ-Opioid-Rezeptoren gezeigt werden, dass die analgetischen Effekte verbessert wurden und die Toleranzentwicklung abgeschwächt wurde, wenn der Rezeptor eine Präferenz für den G-Protein Signalweg zeigte. Unerwarteterweise wurden die anderen Nebenwirkungen, wie Atemdepressionen, Obstipation, sowie Entzugssymptome jedoch dadurch verschlimmert. Ein Erklärungsversuch für dieses andauernde Problem bei der Entwicklung sicherer Opioid-Medikamente basiert auf der verminderten intrinsischen Aktivität dieser G- Protein Signalweg-betonten Arzneistoffe. Trotz allem ist es bislang

immer noch wenig verstanden ob, wie und unter welchen Umständen der μ-Opioid-Rezeptor dimerisiert und ob dies Potential zur Veränderung des beschriebenen Signalprofils aufweist.

Ich zeige in dieser Arbeit, dass der μ-Opioid-Rezeptor einer gewissen Kompartmentalisierung auf der Zelloberfläche unterliegt und dass seine Mobilität durch Rezeptoraktivierung verändert wird. Zudem sehe ich eine Korrelation zwischen der durch den Agonisten vermittelten Dimerisierung und der Rekrutierung von β-Arrestin2. Unter Anwendung von Einzelmolekülmikroskopie habe ich einzelne μ-Opioid-Rezeptoren auf der Oberfläche von lebenden Zellen verfolgt und entdeckt, dass Aktinfilamente als Diffusionsbarrieren fungieren und somit zur Kompartmentalisierung des μ-Opioid-Rezeptors beitragen. Rezeptoraktivierung löst diese Kompartmentalisierung teilweise auf und führt unmittelbar zu einer erhöhten Diffusionsgeschwindigkeit des μ-Opioid-Rezeptors. Dabei können eine erhöhte Anzahl von Rezeptoren die Aktinfilamente überwinden. Jedoch erfolgte zu späteren Zeitpunkten eine verstärkte Kompartmentalisierung des Rezeptors und damit einhergehend für jene μ-Opioid Rezeptoren, die durch DAMGO aktiviert wurden, die Ausbildung von Dimeren, sowie die Rekrutierung von β-Arrestin2.

Ergebnisse mit verschiedenen Inhibitoren und Rezeptor-Mutationen zeigen wie die μ-Opioid-Rezeptoraktivierung durch einen β-Arrestin bevorzugenden Liganden zur Ausbildung eines Dimers führt, welche durch Antagonist Zugabe reversibel ist und sich von Rezeptorakkumulation vor der Internalisierung unterscheidet. Ich hoffe, dass diese Ergebnisse Potential für die Entwicklung sicherer Opioid-Medikamente aufweisen. Ein Beispiel wäre es, durch Adressierung der Dimerisierungs-Grenzfläche als potenzielle allosterische Zielstruktur die Rezeptordimerisierung zu vermindern und hierüber den β-Arrestin-vermittelten Signalweg zu verändern, ohne ihn komplett abzuschalten. Das individuelle und kombinierte Adressieren von orthosterischen und allosterischen Zielstrukturen (möglicherweise die Grenzfläche zwischen den Transmembrandomänen 1 und 2, sowie der Helix 8) des μ-Opioid-Rezeptors könnte untersucht werden, um darüber eventuell eine präzisere Feineinstellung von μ-Opioid-Rezeptor Agonisten zu erwirken. Da unterschiedliche zelluläre Verbände aus unterschiedlichen Geweben abweichende Cytoskelett-Strukturen enthalten, könnte der Einfluss des Cytoskeletts auf die Kompartmentalisierung des Rezeptors, sowie die lokale Signalaktivierung und die Umverteilung des Rezeptors auf der Zelloberfläche dazu beitragen gewebeabhängige Wirkungen, Nebenwirkungen und Interaktionspotentiale besser zu verstehen.

7. Outlook

This chapter deals with side works and tools which developed along with the thesis project, during the time course of my doctoral studies. It addresses GPCR research topics that I would like to investigate more intensively in the future, additionally to the ongoing opioid receptor-oriented research.

7.1. Generation of improved cAMP sensor

The second messenger molecule cAMP is essential for signal propagation of those G protein coupled receptors, which couple to heterotrimeric G proteins comprising α-subunits of Gi or Gs. Driven through the large interest of measuring cAMP in living cells for drug discovery and pharmacological research a series of biosensors have been developed[166,240–242]. Since the initial development of a Epac-based cAMP sensors in our laboratory[240], a series of improved sensors with different fluorophores and partially modified Epac-based response elements enriched the scientific community up to the fourth generation of Epac-based FRET sensors[166]. So far, most of these sensors are based on fluorescent proteins, entailing besides the problem of photobleaching and insufficient protein-maturation also inflexibility regarding the desired wavelength at which the assay can be conducted. Whereas the usage of short-wave-length light close to the UV range in FRET-measurements can cause radiation damage, auto-fluorescence from cellular background and insufficient tissue penetration, usage of wavelengths close to the infrared spectra usually results in poor signal to noise ratios, due to the low energy of emitted photons. Furthermore crosstalk between channels, both excitation and emission, requires non-trivial corrections especially in image based measurements[86]. This becomes even more challenging if more than two colors are desired for the measurement/imaging process[86]. To address these problems, we developed a tool, which allows flexibility regarding the choice of wavelength for imaging and robust signal to noise ratios over a large spectral range, even in measurements on a sub-cellular level.

Initially, we used the Epac-based H187 FRET sensor (**Figure 73a**), which was published by others before[166] and tested it for its capability for FRET-measurements in 96-well plates[87]. Co-expression of the β_1AR and stimulation with isoproterenol showed a maximum response by this sensor of 60.3 ± 0.8% Even though this is already an outstanding dynamic range (**Figure 73c**), we used a concept (**Figure 73b**) which was previously applied to a series of GPCR sensors and led to an improved dynamic range[132]. Replacement of the CFP/YFP variants by nanoLuciferase/Halo-tag-618 ligand resulted in a BRET-sensor with a dynamic range of 68.5 ± 0.7%, while IC_{50}-values were not significantly affected. Emission spectra of both sensors show that the donor and acceptor signals are more separated in case of the BRET-sensor (**Figure 73d**), which simplifies the spectral separation by filters or monochromators.

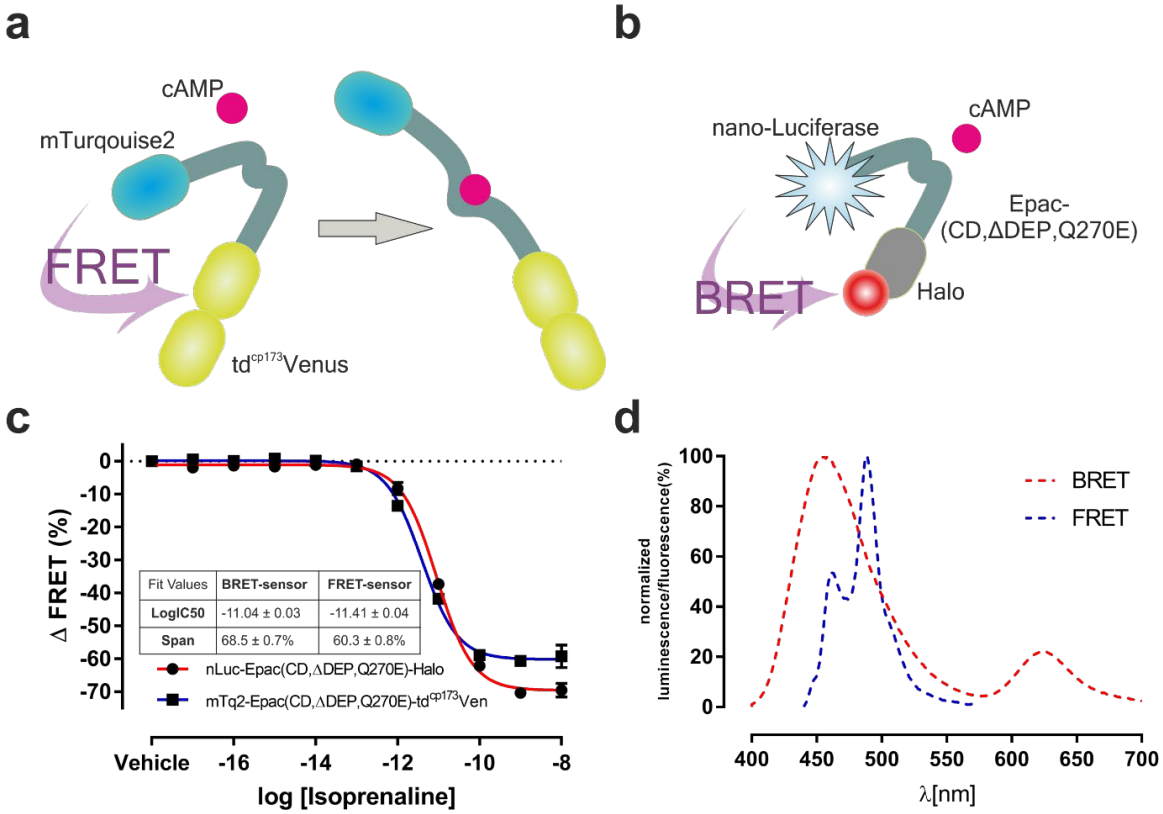

Figure 73:Development of nanoBRET-based sensor for cAMP

a), Illustrated working principle of the previously by others published FRET sensor: Upon cAMP binding the response element undergoes a conformational change causing an increased distance between donor (mTurqouise2) and acceptor (td-cp173-Venus) causing reduced resonant energy transfer b), Combining the response element of (a) with nanoLuciferase (donor) and Halotag-608 (acceptor) results in a BRET-sensor c), Comparison of the sensor shown in (a) versus the sensor shown in (b) reveals an increased span of the BRET-sensor d), Normalized emission spectra of both sensors show more separated peaks for donor an acceptor signal.

Next, we used again the previously mentioned cAMP response-element and added N-terminally a SNAP-tag[124] and C-terminally an Halo-tag[128]. As mentioned before, these tags allow, due to an entirely different working mechanism, a simultaneous and selective self-labelling in the corresponding position of the sensor (**Figure 74a**). Using fluorophores with increased photostability[243], covalently attached to the reactive groups for SNAP- and Halo-tags[181], we were able to conduct simultaneous dual-color labelling. This strategy allows furthermore to switch the position of donor and acceptor just by addressing the desired tag with the chosen color. For initial validation of the sensor, we labeled the SNAP-tag with JF-549 Dye and the Halo-tag with JF-646 Dye as well as vice versa. In both combinations the IC_{50}-value did not differ noticeably from the above-mentioned sensor constructs. However, when the SNAP-tag was used for the donor-position, the dynamic range was significantly larger in contrast to the use of Halo-tag as donor position (**Figure 74b**). To investigate the full spectra and flexibility of this sensor we used a series of 7 different JF-dyes[243] with excitation peaks reaching from 424nm up to 646nm. We tested all 42 possible combinations to measure the dynamic range of the sensor at the used excitation wavelength and obtained in the red/far-red range (JF635-JF646) still a response of approximately 5% (**Figure 74c**). As one would expect in a sensor which uses small fluorophores to achieve different color-combinations the log-IC_{50}-values were not affected by labelling with different colors.

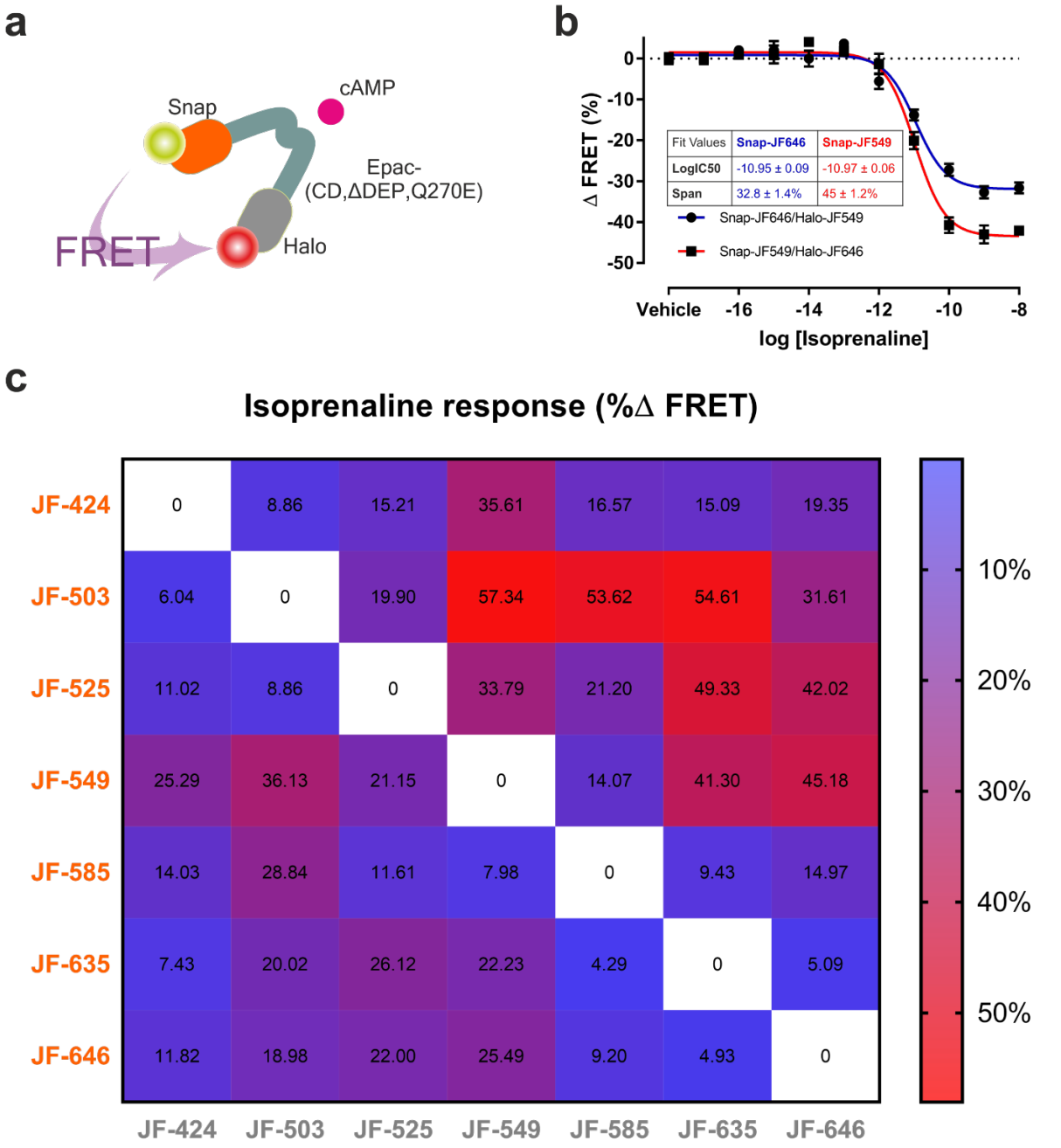

Figure 74: Flexible multicolor cAMP sensor based on self-labelling tags

a), Sensor concept as in (Figure 73a) but nanoLuciferase was replaced by SNAP-tag. b), Span and log-IC_{50}-values of the sensor labelled with JF-549 and JF-646. Using the SNAP-tag as position for labelling with donor dye resulted here in a bigger span. c), Comparison of 42 different dye combinations. A generally observed trend is, that the sensor provides a larger span if the SNAP-tag is used as donor-position.

To allow cAMP measurements in a sub-cellularly localized manner we inserted Lifeact7 N-terminally as a targeting sequence for actin (**Figure 75a**). The log-IC_{50}-value of this construct, labelled with SNAP-JF549 and Halo-JF646, does not differ significantly from the non-targeted sensor (**Figure 75b**). The span is reduced in comparison to the ubiquitously expressed sensor by≈10%, presumably due to a less global signal. Using FRET-based dual-color TIRF-images (just the donor-channel was excited using a 561nm laser-line) we were able to show a successful targeting to actin (**Figure 75c**). Since the emission channel of the acceptor (magenta) is corrected for bleed-through and direct excitation, the remaining signal is a result of FRET. The overlay image of both emission channels shows furthermore specific labelling for both channels.

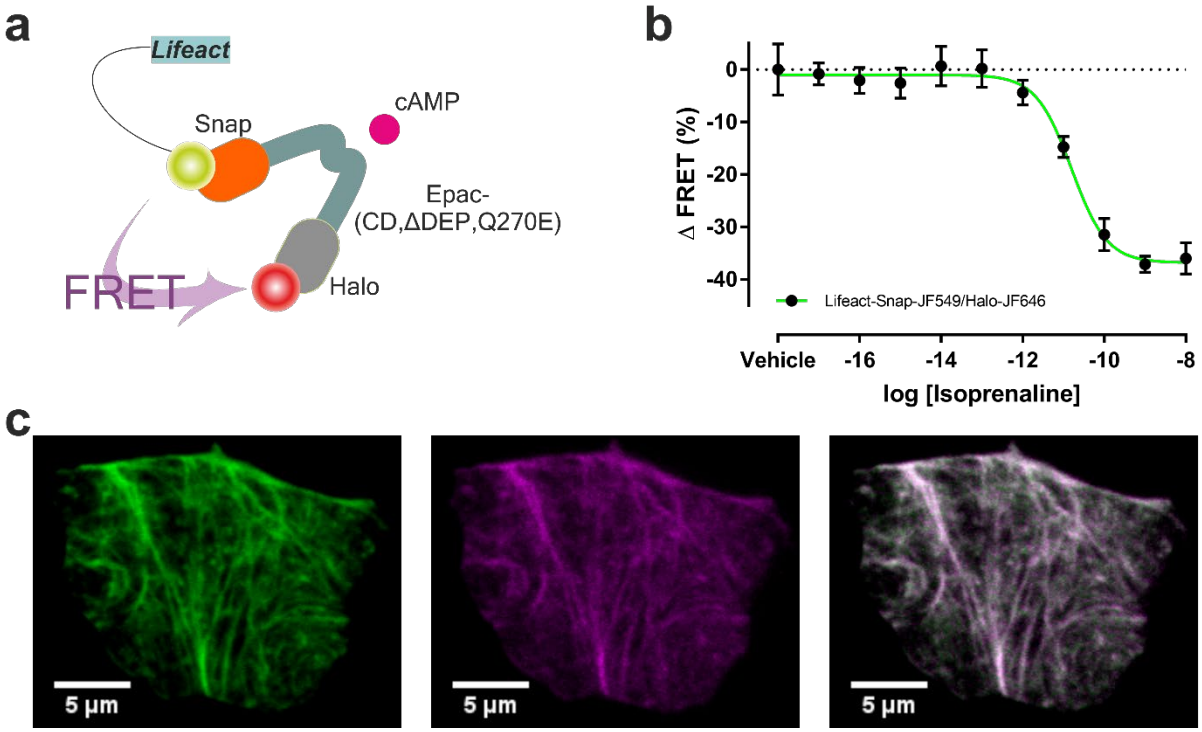

Figure 75: Localization of the FRET sensor to actin
a), N-terminal insertion of the LifeAct-sequence was used to target the FRET-sensor to actin. b), Whereas the span is reduced (35.8±1.9%), the log-IC_{50}-value (-10.8±0.12) does not differ significantly from the non-targeted sensor. c, TIRF-images show successful targeting to actin and specific labelling of both tags. SNAP-tags are labelled with JF549 (green) and Halo-tags are labelled with JF-646 (magenta).
Green and magenta result in white in the corresponding overlay image.

The combination of site-specific labelling[124,128] and chemical-fluorophores with enhanced photostability[243], minimizes a loss of signal due to photobleaching. A large dynamic range of the used sensor element[166] allows a crosstalk reduction between donor and acceptor channels by selection of dyes with narrow excitation/emission spectra. This sensor concept enables live cell measurements of cAMP at various desired wavelengths of light and can be further used to quantify cAMP signaling in different cellular compartments. We anticipate that this can serve as a helpful tool for simplified simultaneous imaging of multiple colors, studies in tissue and might even enable a super-resolved imaging of cAMP.

7.2. Investigation of the β_1AR-autoantibodies and the related weak cAMP signal

Receptor autoantibodies, more concisely GPCR autoantibodies, are associated with a number of highly diverse diseases, and the understanding of the mechanisms and consequences on GPCR signaling are reaching from quite well established in Grave's disease, over a more diffuse knowledge about their role in pre-eclampsia, to a still insufficient understanding in dilated cardiomyopathy (DCM)[244]. Several studies have pointed out the importance of β_1AR-autoantibodies in the development of DCM but are lacking conclusive explanation of the molecular mechanism[245–248]. Resulting from the lack of understanding, there is a challenge for the development of a reliable diagnostic assay for DCM patients that has been going on since decades.

A quite elucidating study by Marshall et al. could show for the turkey β_1AR that receptor activation by autoantibodies that target the ECL2 is predominantly resulting in G protein mediated cAMP signaling and might furthermore be linked to receptor dimerization due to the bivalent nature of full IgGs[249]. This was further underlined by data which showed that monovalent Fab fragments of receptor antibodies failed in receptor activation. We addressed this observation with single-molecule microscopy and found some preliminary data which underlines these previous results.

We expressed and labeled SNAP-tagged β_1ARs in CHO cells as previously described for the acquisition of single-molecule TIRF images. We observed 15 minutes after the application of the ECL2 targeting monoclonal 23-6-7 antibody[250] an increase of dimeric β_1ARs of ≈ 40 ± 5 % (**Figure 76**).

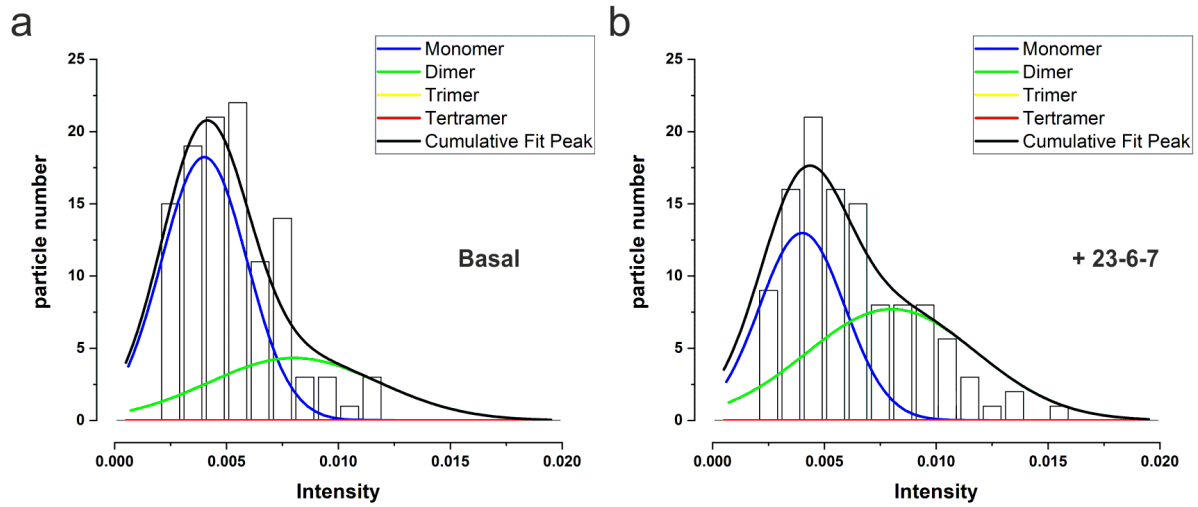

Figure 76: Intensity Histograms of SNAP-β_1 and treatment with the monoclonal β_1AR antibody 23-6-7

Treatment with the monoclonal 23-6-7 antibody leads to an increase of the dimeric receptor fraction.

Furthermore, we observed a largely reduced diffusion coefficient after treatment with the monoclonal antibody (0.083 ± 0.004 $\mu m^2/s$ vs 0.047 ± 0.003 $\mu m^2/s$), as one might suspect for a complex of two receptors and presumably one antibody (**Figure 77**).

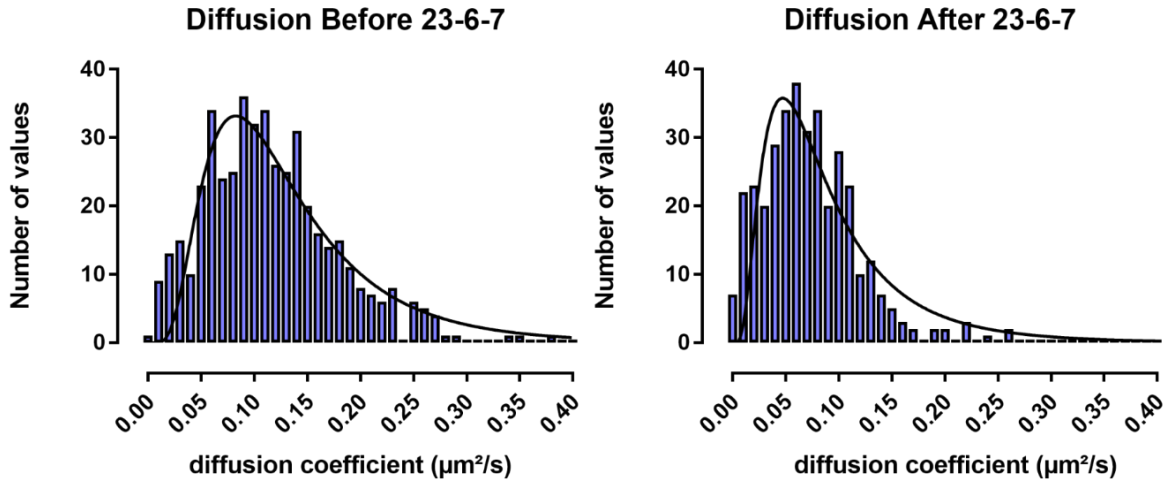

Figure 77: Receptor diffusion before and after treatment with the monoclonal β_1AR antibody 23-6-7
Application of the monoclonal antibody reduces the diffusion coefficient from 0.083 ± 0.004 $\mu m^2/s$ to 0.047 ± 0.003 $\mu m^2/s$, suggesting further the formation of an oligomeric receptor complex.

Since the receptor antibody itself showed repetitively stability problems in our hands, we tested its functionality before each experiment with a cAMP-based assay (**Figure 78**), relying on stable co-expression of the β_1AR wildtype receptor and the previously discussed H187 FRET sensor[166].

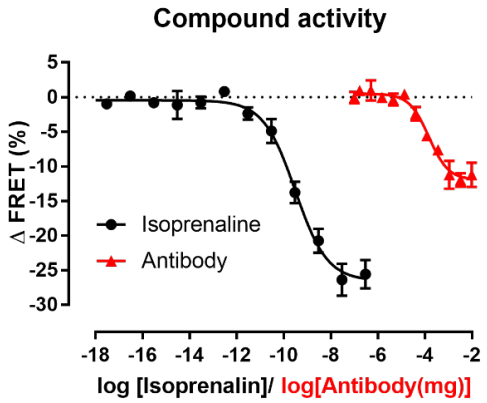

Figure 78: Test for activity of 23-6-7
To validate the activity of the monoclonal antibody it was tested immediately before the microscope experiments in a FRET-based cAMP assay. This assay also confirms the partial agonism of the antibody.
As positive control the full agonist isoprenaline was used.

Taken together, these results show that the partial agonism of the antibody coincidences with receptor dimerization of the β_1AR. Even though we do not entirely understand yet whether the partial agonism causes a conformation that facilitates dimerization or if dimerization leads to the partial agonism, several lines of evidence favor the second hypothesis. This originates initially from the data by others which showed that monovalent Fab-fragments failed in receptor activation and just the full IgG lead to dimeric elution fractions in size exclusion chromatography experiments[249]. In our own hands also just purified antibodies which led to receptor activation, showed increased receptor dimerization in single-molecule experiments. Due to the repetitive stability problems with the 23-6-7 antibody, our attempts with Fab fragments of this antibody are not sufficient for a fundamental statement, but they suggest that antibodies which did not cause a cAMP response, did also not cause receptor dimerization. Interestingly

collaborators (Wallukat G. et al. unpublished data), who relied on a different antibody, were able, in a bioassay on isolated cardiomyocytes, to restore the response of Fab fragments by application of a secondary full IgG antibody targeting these Fab fragments. However, from a structural point of view, a feasible mechanism for the partial activation of the β_1AR might be that bivalent IgG antibodies bring two receptor protomers in a proximity, incompatible with an inactive receptor state and lead thereby to distortion of the receptor conformation. This might cause that the TM6 of the receptor gets displaced by a few angstroms outward, adapting a pose with partial similarity to an active receptor state[251] (**Figure 79**), and facilitating G protein coupling. This mechanism could perhaps also explain the partial agonism of the antibody, mediated by targeting the allosteric ECL2, in contrast to full activation through the orthosteric binding site.

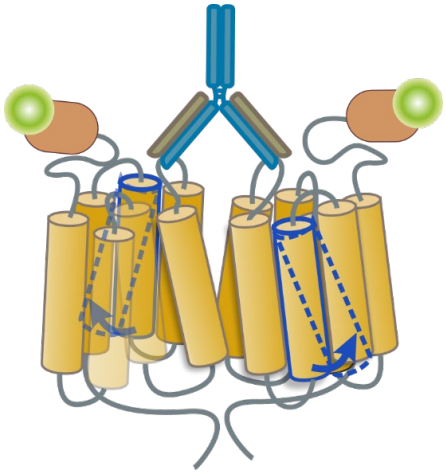

Figure 79: Illustration of a hypothetical partially active β_1AR dimer
The full IgG antibody might by targeting the ECL2 of the β_1AR for steric reasons cause a distortion of the receptor protomers conformation, including an outward displacement of TM6 (blue dashed TMs). This conformation might comprise similarity with the active state of the β_1AR and cause G protein mediated signaling. (The depicted receptor illustrations are shown as N- terminally SNAP-tagged to facilitate comparison of TM orientations)

We were lacking for a while an explanation for the described stability problems of the purified antibody. Since we obtained in acrylamide gels with inactive antibody batches exclusively 150 kDa size bands, reflecting the size of the full IgG, we excluded a protease mediated degradation. We realized just very recently during a discussion with Andrew Kruse, (Harvard Medical School) that the stability problems of our 23-6-7 antibody might be caused by a DG-motif in the complementarity-determining region 3 (CDR3) of the antibody. While CDR3s are often important for antigen binding[252], a DG-motif in this region can due to a nucleophilic attack by the backbones nitrogen lead to a conformational rearrangement, and the following reaction of DG to isoaspartate (**Figure 80**) can lead to a loss of the antibodies activity[253].

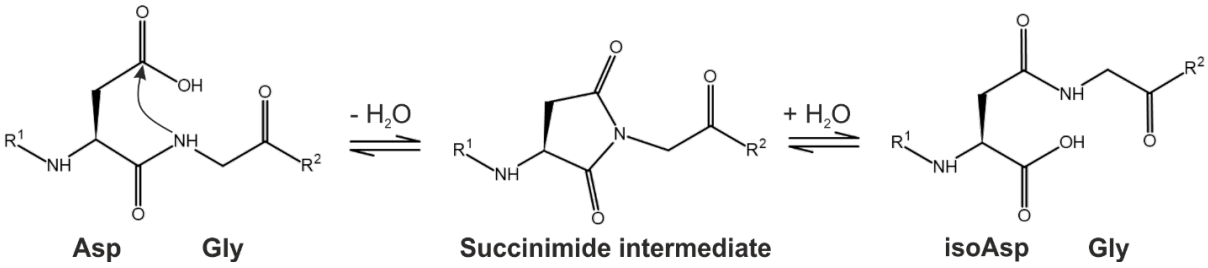

Figure 80: Isoaspartate formation by DG-motifs
In a DG-motif (Asp-Gly) the nucleophilic attack of a nitrogen from the backbone can lead to a succinimide intermediate which is able to hydrolyze to isoaspartate-Gly.

Following this, we will now attempt to solve the stability problem by inserting a mutation in our expression vector that causes the substitution of the aspartate residue by glutamate, and we hope to obtain a more reliable tool for our experimental approaches. In parallel, the collaborating Kruse lab will try to obtain structural data to further elucidate the relation between antibody binding and its influence on conformational changes in the receptor. If these optimizations and structural experiments will be successful, this may enable a better understanding of receptor activation by β_1AR-autoantibodies and their involvement in DCM.

7.3. Setup of a versatile FRET microscope optimized for kinetic measurements

The increasing demand to measure receptor activation kinetics requires reliable fast and sensitive readout methods. Since our lab is mainly based on fluorescence-based readouts, microscopes are the instruments of choice for such measurements. Moreover, due to the increasing number of fluorescent biosensors with various fluorescent markers, flexibility regarding the excitation and emission wavelengths is desirable. A previous study of our lab comprised a microscope optimized for receptor activation kinetics to conduct fast photo-activation experiments of chemically caged ligands[206]. We further optimized this microscope to make it applicable to a broader set of experimental requirements and users.

The initial change was just a small optimization by using more sensitive PMTs (**Figure 81**-1) and reducing readout noise by installing a digitizer with noise silencing technology (**Figure 81**-2). Triggered by growing interest to measure receptor activation and downstream signaling kinetics in an image-based manner, to eventually visualize subcellular activation patterns, we decided to install on the second (left) emission port of the microscope body an optical image splitter (**Figure 81**-3) and two sCMOS cameras with fast sampling capabilities (**Figure 81**-4-4'). In addition to the 100x objective we installed 63x and 40x objectives (**Figure 81**-5) to also allow simultaneous measurements of several cells in the chosen field of view. Since the original microscope was just equipped with CFP/YFP filters for excitation and emission channels, we decided to take advantage of the installed, wavelength variable, LED-based, excitation light source (**Figure 81**-6) and installed also easily exchangeable filter cubes for GFP/RFP as well as Cy3/Cy5 (**Figure 81**-7). To enable also kinetic measurements with ligand super-fusion, we installed an eight-channel perfusion system (**Figure 81**-8) and an electronic micro-manipulator (**Figure 81**-9) that allows precise fine adjustment of the perfusion needle tip relative to the cell of interest. To finally simplify the system's operation for multi-user requirements, we installed a commercial imaging software that is able to control all main elements of the microscope through one application (**Figure 81**-10).

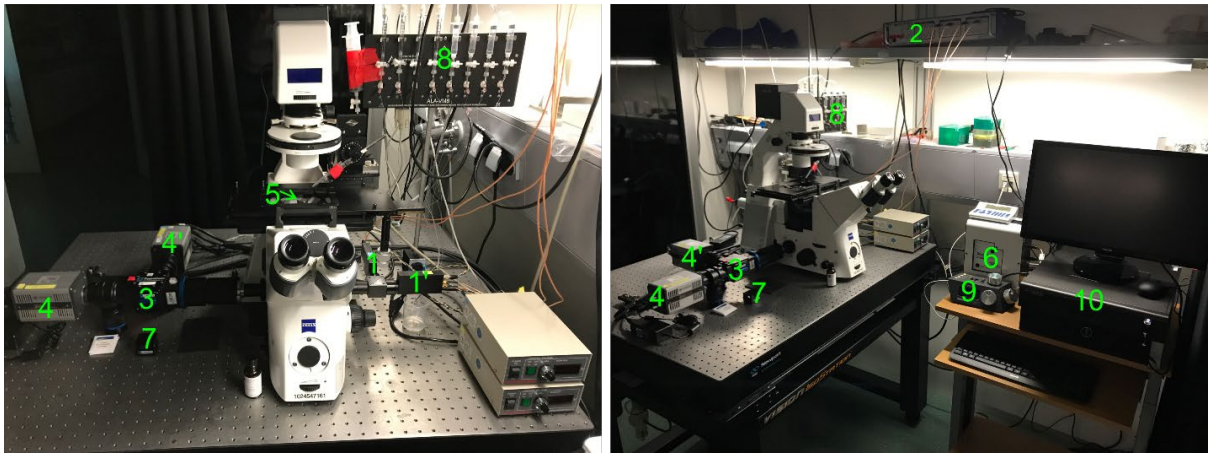

Figure 81: Modifications of the FRET-microscope
1) Hamamatsu photonics PMTs, 2) Digitizer: Axon Digidata® 1550B Low-Noise Data Acquisition System with HumSilencer™, 3) Image Splitter: CAIRN Research Twincam, 4) sCMOS camera: Andor Zyla 4.2, 4') sCMOS camera: Andor Zyla 4.2 , 5) Objective revolver with 40x/63x/100x objectives (Zeiss), 6) LED-based light source with 16 different wavelengths reaching from 405 nm – 770 nm (CoolLED), 7) CAIRN Research Filtercube for simple filter exchange in the Image splitter (3), 8) Perfusion system: ALA Scientific instruments Octaflow, 9) Micromanipulator: 10) Microscope computer with Metafluor as global microscope control software.

For initial test measurements we used the optimized version of the cpGFP based μOR sensor (**Figure 69**) and were able to resolve its activation and deactivation kinetics (Figure **82**). The activation kinetics of the new sensor (τ= 74 ± 8 ms) are in line with previous measurements, which were based on the initial version of the μOR-cpGFP sensor (τ= 96 ±18 ms).

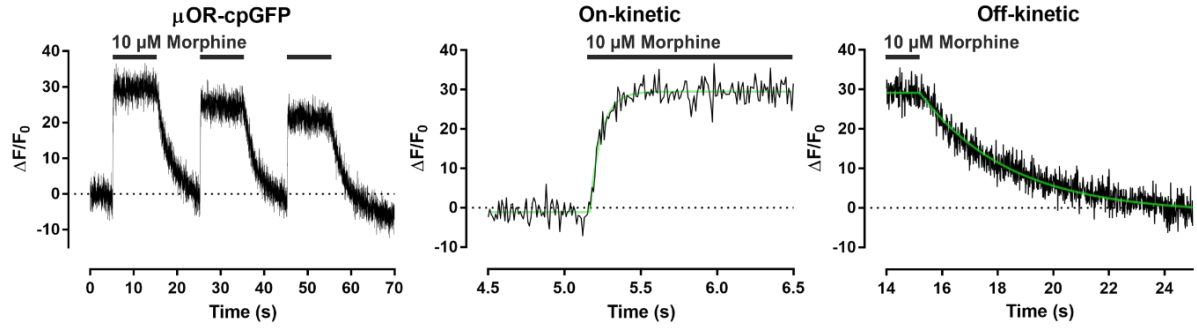

Figure 82: Image based kinetic measurements using the optimized μOR-cpGFP sensor
Test measurements with the microscope on receptor activation and deactivation kinetics. We measured an activation time (on-kinetic) of τ= 74 ± 8 ms and a deactivation time (off-kinetic) of 3.2 ± 0.16 s for the optimized μOR-cpGFP sensor.

To also check the functionality in FRET measurements, we conducted dual-color measurements of the H187 cAMP sensor after addition of 100 nM isoprenaline (**Figure 83a**) and obtained quite robust image based FRET-responses also without correction of channel crosstalk (**Figure 83b**).

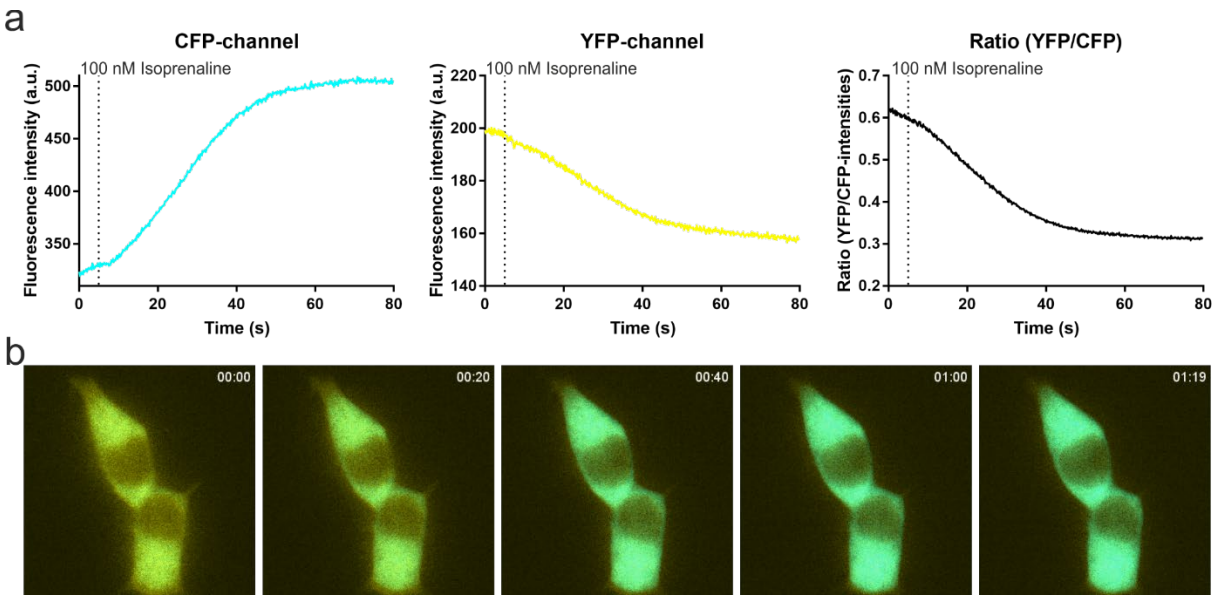

Figure 83: Image based FRET measurement with the H187 cAMP sensor
a), Uncorrected FRET traces obtained by dual color imaging of the cells shown in (b) indicate a robust FRET-response. b), Composite images of both detection channels during the measurement.

We provide with this microscope setup a user-friendly tool for robust image-based kinetic measurements down to the one-digit millisecond range. However, if a temporal resolution of microseconds is required, the image-based imaging on this setup reaches its limitations and the use of the PMTs on the right microscope port is preferable for signal detection.

7.4. Peptide expression for stabilization of intermediate receptor states

During the last years in GPCR research a repetitively discussed topic, mainly promoted by the Kobilka lab, is the existence, function and meaning of intermediate receptor states between the inactive and active receptor state[11,12,254,255]. Also, in our lab the existence of intermediate states and their involvement in receptor activation kinetics raised increasing interest[206]. A suggestion of reviewers to stabilize an intermediate state by G protein overexpression could not be satisfied, because the FRET sensors used are impaired in G protein coupling due to the insertion of fluorescent proteins in the ICL3 and at the C-terminal end of the receptor. The Kobilka lab showed last year structural data on an intermediate state of the β_2AR[16], stabilized by a peptide sequence that is based on the last 14 amino acids of the C-terminal end of the $G\alpha_s$ subunit and mimics the G protein's α-helical domain (AHD). Therefore, we tried to find a solution to transfer this tool into living cells.

We created plasmids encoding for the sequences of the last 14 amino acids of $G\alpha_s$, $G\alpha_i$ $G\alpha_0$ and $G\alpha_q$. To allow quantification of the expression levels and for a less biased expression due to the individual codon composition[256], we inserted N-terminally a SNAP-tag, followed by a T2A cleavage site (**Figure 84**). The T2A cleavage site elongates the resulting peptide by one proline, which we considered for now as inert for functional consequences in this N-terminal position[257].

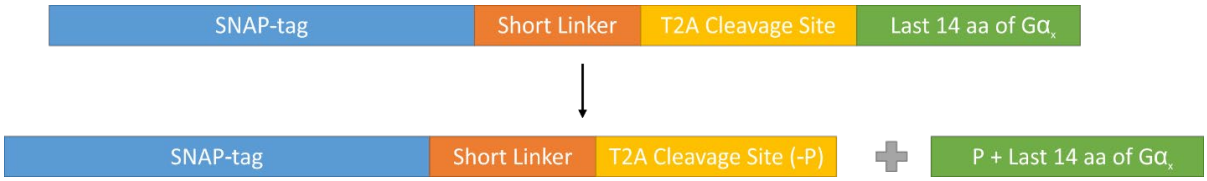

Figure 84: 14 amino-acid peptide expression constructs

Preliminary experiments with co-expression of the β_2AR, the peptide plasmids and the above mentioned H187 cAMP sensor show, in contrast to Gi and Gq peptides, a reduced dynamic range of the H187 sensor when the Gs peptide is co-expressed (**Figure 85a**). The reason for this can be found in a lower basal ratio (**Figure 85b**) and following a reduced ΔFRET after full sensor activaton (**Figure 85c**) with forskolin (FSK) and 3-isobutyl-1-methylxanthine (IBMX), when the Gs peptide is present.

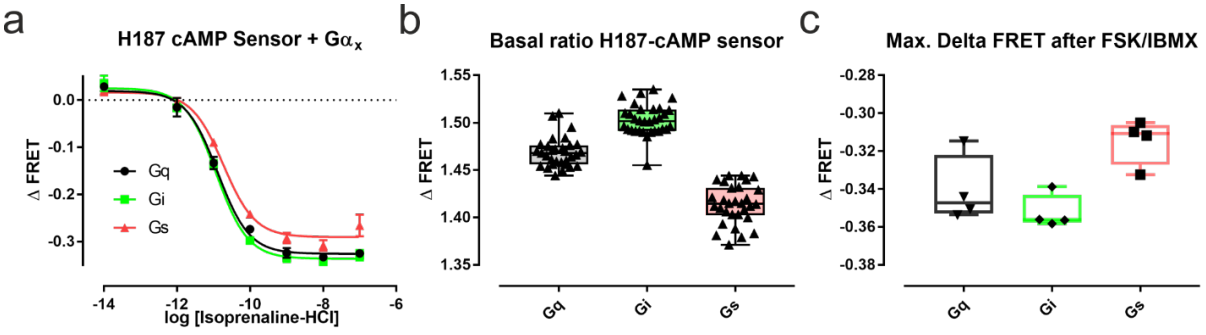

Figure 85: Experiments with the H187 cAMP sensor and co-expression of the 14aa peptides.

Attempts to see this effect at the receptor level using the β_2AR-FRET sensor failed to show a significant difference among the peptides. It has been shown by a colleague in the lab that a nanoBRET based version of the β_2AR-sensor has a larger dynamic range than the FRET-based sensor[132] and we repeated therefore such co-expression experiments with the nanoBRET-based sensor. Here, the Gs peptide showed a remarkable difference to Gi, but interestingly the Gq peptide showed almost the same response as Gs (**Figure 86a,b**). Comparison of the sequences led us to an attempt for an explanation of those observations. The physicochemical properties of the last 7 amino acids are very similar for Gq and Gs (**Figure 86c**), suggesting that they exhibit a similar effect in this isolated form, which lacks further selectivity determinants of Gα subunits.

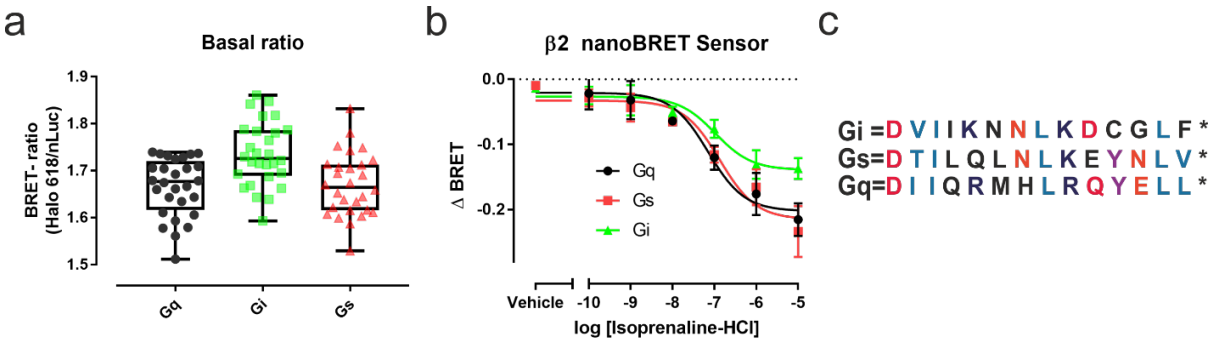

Figure 86: Co-expression experiments based on the conformational β_2AR BRET sensor

Our preliminary results give hope that at least for sensors with a large dynamic range, a stabilization of intermediate receptor states might be possible and that such intermediate states could facilitate receptor activation. Further evidence for functionality of this principle comes from an assay based on C-terminal hexapeptides of the AHD, which was published by a collaborator for the determination of G protein coupling selectivites[258]. Whether this peptide expression plasmids might be helpful for detection of kinetic differences by stabilization of intermediate receptor states, remains for now open but could be investigated in the future, perhaps in combination with cpGFP based GPCR sensors as described above for the μOR.

8. Bibliography

1. Pierce, K. L., Premont, R. T. & Lefkowitz, R. J. Seven-transmembrane receptors. *Nature Reviews Molecular Cell Biology* (2002) doi:10.1038/nrm908.
2. Fredriksson, R., Lagerström, M. C., Lundin, L.-G. & Schiöth, H. B. The G-Protein-Coupled Receptors in the Human Genome Form Five Main Families. Phylogenetic Analysis, Paralogon Groups, and Fingerprints. *Mol. Pharmacol.* **63**, 1256 LP – 1272 (2003).
3. Rosenbaum, D. M., Rasmussen, S. G. F. & Kobilka, B. K. The structure and function of G-protein-coupled receptors. *Nature* **459**, 356–363 (2009).
4. Birgül, N., Weise, C., Kreienkamp, H. J. & Richter, D. Reverse physiology in Drosophila: Identification of a novel allatostatin-like neuropeptide and its cognate receptor structurally related to the mammalian somatostatin/galanin/opioid receptor family. *EMBO J.* (1999) doi:10.1093/emboj/18.21.5892.
5. Ballesteros, J. A. & Weinstein, H. Integrated methods for the construction of three-dimensional models and computational probing of structure-function relations in G protein-coupled receptors. *Methods Neurosci.* (1995) doi:10.1016/S1043-9471(05)80049-7.
6. Venkatakrishnan, A. J. *et al.* Molecular signatures of G-protein-coupled receptors. *Nature* (2013) doi:10.1038/nature11896.
7. B., T. *et al.* Action of molecular switches in GPCRs - Theoretical and experimental studies. *Curr. Med. Chem.* (2012) doi:10.2174/092986712799320556 LK
8. Devree, B. T. *et al.* Allosteric coupling from G protein to the agonist-binding pocket in GPCRs. *Nature* (2016) doi:10.1038/nature18324.
9. Standfuss, J. *et al.* The structural basis of agonist-induced activation in constitutively active rhodopsin. *Nature* (2011) doi:10.1038/nature09795.
10. Flock, T. *et al.* Universal allosteric mechanism for Gα activation by GPCRs. *Nature* (2015) doi:10.1038/nature14663.
11. Staus, D. P. *et al.* Allosteric nanobodies reveal the dynamic range and diverse mechanisms of G-protein-coupled receptor activation. *Nature* (2016) doi:10.1038/nature18636.
12. Gregorio, G. G. *et al.* Single-molecule analysis of ligand efficacy in β2AR-G-protein activation. *Nature* (2017) doi:10.1038/nature22354.
13. Venkatakrishnan, A. J. *et al.* Diverse activation pathways in class A GPCRs converge near the G-protein-coupling region. *Nature* (2016) doi:10.1038/nature19107.
14. Lefkowitz, R. J., Mullikin, D. & Caron, M. G. Regulation of beta-adrenergic receptors by guanyl-5'-yl imidodiphosphate and other purine nucleotides. *J. Biol. Chem.* (1976).
15. Kent, R. S., De Lean, A. & Lefkowitz, R. J. A quantitative analysis of beta-adrenergic receptor interactions: resolution of high and low affinity states of the receptor by computer modeling of ligand binding data. *Mol. Pharmacol.* (1980).
16. Liu, X. *et al.* Structural Insights into the Process of GPCR-G Protein Complex Formation. *Cell* **177**, 1243-1251.e12 (2019).
17. McCudden, C. R., Hains, M. D., Kimple, R. J., Siderovski, D. P. & Willard, F. S. G-protein signaling: back to the future. *Cell. Mol. Life Sci.* **62**, 551–577 (2005).
18. Yin, J. *et al.* Structure of a D2 dopamine receptor–G-protein complex in a lipid membrane. *Nature* (2020) doi:10.1038/s41586-020-2379-5.
19. Koehl, A. & others. Structure of the μ-opioid receptor–Gi protein complex. *Nature* **558**, 547–555 (2018).
20. Kniazeff, J., Prézeau, L., Rondard, P., Pin, J.-P. & Goudet, C. Dimers and beyond: The functional puzzles of class C GPCRs. *Pharmacol. Ther.* **130**, 9–25 (2011).
21. Bayburt, T. H., Leitz, A. J., Xie, G., Oprian, D. D. & Sligar, S. G. Transducin activation by nanoscale lipid bilayers containing one and two rhodopsins. *J. Biol. Chem.* (2007) doi:10.1074/jbc.M701433200.
22. Whorton, M. R. *et al.* A monomeric G protein-coupled receptor isolated in a high-density lipoprotein particle efficiently activates its G protein. *Proc. Natl. Acad. Sci. U. S. A.* (2007) doi:10.1073/pnas.0611448104.
23. Kuszak, A. J. *et al.* Purification and functional reconstitution of monomeric μ-opioid receptors. Allosteric modulation of agonists binding by Gi2. *J. Biol. Chem.* (2009) doi:10.1074/jbc.M109.026922.
24. Milligan, G. & Bouvier, M. Methods to monitor the quaternary structure of G protein-coupled receptors.

FEBS Journal (2005) doi:10.1111/j.1742-4658.2005.04731.x.

25. Gandía, J., Lluís, C., Ferré, S., Franco, R. & Ciruela, F. Light resonance energy transfer-based methods in the study of G protein-coupled receptor oligomerization. *BioEssays* (2008) doi:10.1002/bies.20682.

26. Pin, J. P. *et al.* International union of basic and clinical pharmacology. LXVII. Recommendations for the recognition and nomenclature of G protein-coupled receptor heteromultimers. *Pharmacological Reviews* (2007) doi:10.1124/pr.59.1.5.

27. Ferré, S. *et al.* G protein-coupled receptor oligomerization revisited: functional and pharmacological perspectives. *Pharmacol. Rev.* **66**, 413–434 (2014).

28. Kasai, R. S. *et al.* Full characterization of GPCR monomer\dimer dynamic equilibrium by single molecule imaging. *J. Cell Biol.* **192**, 463–480 (2011).

29. Calebiro, D. & others. Single-molecule analysis of fluorescently labeled G-protein–coupled receptors reveals complexes with distinct dynamics and organization. *PNAS* **2**, 743–748 (2013).

30. Hern, J. A. *et al.* Formation and dissociation of M1 muscarinic receptor dimers seen by total internal reflection fluorescence imaging of single molecules. *Proc. Natl. Acad. Sci. U. S. A.* (2010) doi:10.1073/pnas.0907915107.

31. Stoneman, M. R. *et al.* A general method to quantify ligand-driven oligomerization from fluorescence-based images. *Nat. Methods* **16**, 493–496 (2019).

32. Annibale, P. & Lohse, M. J. Spatial heterogeneity in molecular brightness. *Nat. Methods* (2020) doi:10.1038/s41592-020-0732-0.

33. Stoneman, M. R., Biener, G. & Raicu, V. Reply to: Spatial heterogeneity in molecular brightness. *Nat. Methods* (2020) doi:10.1038/s41592-020-0735-x.

34. Manglik, A. & others. Crystal structure of the μ-opioid receptor bound to a morphinan antagonist. *Nature* **485**, 321–326 (2012).

35. Huang, W. & others. Structural insights into μ-opioid receptor activation. *Nature* **524**, 315–321 (2015).

36. Wu, B. *et al.* Structures of the CXCR4 chemokine GPCR with small-molecule and cyclic peptide antagonists. *Science* **330**, 1066–1071 (2010).

37. Wu, H. *et al.* Structure of the human κ-opioid receptor in complex with JDTic. *Nature* **485**, 327–332 (2012).

38. Huang, J., Chen, S., Zhang, J. J. & Huang, X.-Y. Crystal structure of oligomeric β1-adrenergic G protein–coupled receptors in ligand-free basal state. *Nat. Struct. Mol. Biol.* **20**, 419–425 (2013).

39. Salom, D. *et al.* Crystal structure of a photoactivated deprotonated intermediate of rhodopsin. *Proc. Natl. Acad. Sci. U. S. A.* **103**, 16123–8 (2006).

40. Milligan, G. The prevalence, maintenance, and relevance of G protein-coupled receptor oligomerization. *Mol. Pharmacol.* **84**, 158–169 (2013).

41. Villardaga, J. P. & others. Conformational cross-talk between α2A-adrenergic and μ-opioid receptors controls cell signaling. *Nat. Chem. Biol.* **4**, 126–131 (2008).

42. Ng, J., Rashid, A. J., So, C. H., O'Dowd, B. F. & George, S. R. Activation of calcium/calmodulin-dependent protein kinase alpha in the striatum by the heteromeric D1-D2 dopamine receptor complex. *Neuroscience* **165**, 535–541 (2010).

43. Lambert, N. A. & Javitch, J. A. CrossTalk opposing view: Weighing the evidence for class A GPCR dimers, the jury is still out. *J. Physiol.* **592**, 2443–2445 (2014).

44. Milligan, G., Ward, R. J. & Marsango, S. GPCR homo-oligomerization. *Curr. Opin. Cell Biol.* **57**, 40–47 (2019).

45. Kasai, R. S. & Kusumi, A. Single-molecule imaging revealed dynamic GPCR dimerization. *Curr. Opin. Cell Biol.* **27**, 78–86 (2014).

46. Khelashvili, G. *et al.* GPCR-OKB: the G Protein Coupled Receptor Oligomer Knowledge Base. *Bioinformatics* **26**, 1804–1805 (2010).

47. Beckett, A. H. & Casy, A. F. SYNTHETIC ANALGESICS: STEREOCHEMICAL CONSIDERATIONS. *J. Pharm. Pharmacol.* (1954) doi:10.1111/j.2042-7158.1954.tb11033.x.

48. Bunzow, J. R. *et al.* Molecular cloning and tissue distribution of a putative member of the rat opioid receptor gene family that is not a μ, δ or κ opioid receptor type. *FEBS Lett.* (1994) doi:10.1016/0014-5793(94)00561-3.

49. Akil, H. *et al.* Endogenous Opioids: Biology and Function. *Annu. Rev. Neurosci.* **7**, 223–255 (1984).

50. Zadina, J. E., Hackler, L., Ge, L.-J. & Kastin, A. J. A potent and selective endogenous agonist for the μ-opiate receptor. *Nature* **386**, 499–502 (1997).

51. Lutz, P.-E., Courtet, P. & Calati, R. The opioid system and the social brain: implications for depression and suicide. *J. Neurosci. Res.* **98**, 588–600 (2020).

52. PATERSON, S. J., ROBSON, L. E. & KOSTERLITZ, H. W. CLASSIFICATION OF OPIOID RECEPTORS. *Br. Med. Bull.* **39**, 31–36 (1983).

53. Hollt, V. Opioid Peptide Processing and Receptor Selectivity. *Annu. Rev. Pharmacol. Toxicol.* (1986) doi:10.1146/annurev.pharmtox.26.1.59.

54. Civelli, O. *et al.* The next frontier in the molecular biology of the opioid system - The opioid receptors. *Mol. Neurobiol.* (1987) doi:10.1007/BF02935742.

55. Surratt, C. K. *et al.* μ opiate receptor. Charged transmembrane domain amino acids are critical for agonist recognition and intrinsic activity. *J. Biol. Chem.* (1994).

56. Pogozheva, I. D., Lomize, A. L. & Mosberg, H. I. Opioid receptor three-dimensional structures from distance geometry calculations with hydrogen bonding constraints. *Biophys. J.* (1998) doi:10.1016/S0006-3495(98)77552-6.

57. Kaserer, T., Lantero, A., Schmidhammer, H., Spetea, M. & Schuster, D. μ Opioid receptor: novel antagonists and structural modeling. *Sci. Rep.* **6**, 21548 (2016).

58. Al-Hasani, R. & Bruchas, M. R. Molecular mechanisms of opioid receptor-dependent signaling and behavior. *Anesthesiology* (2011) doi:10.1097/ALN.0b013e318238bba6.

59. Halls, M. L. & others. Plasma membrane localization of the μ-opioid receptor controls spatiotemporal signaling. *Sci. Signal.* **9**, ra16 (2016).

60. Mochizuki, N. *et al.* Activation of the ERK/MAPK pathway by an isoform of rap1GAP associated with Gαi. *Nature* **400**, 891–894 (1999).

61. Machelska, H. & Celik, M. Ö. Advances in Achieving Opioid Analgesia Without Side Effects. *Front. Pharmacol.* **9**, 1388 (2018).

62. Sadja, R., Alagem, N. & Reuveny, E. Gating of GIRK channels: Details of an intricate, membrane-delimited signaling complex. *Neuron* (2003) doi:10.1016/S0896-6273(03)00402-1.

63. Peleg, S., Varon, D., Ivanina, T., Dessauer, C. W. & Dascal, N. Gαi controls the gating of the G protein-activated K+ channel, GIRK. *Neuron* (2002) doi:10.1016/S0896-6273(01)00567-0.

64. Zhang, J. *et al.* Role for G protein-coupled receptor kinase in agonist-specific regulation of μ-opioid receptor responsiveness. *Proc. Natl. Acad. Sci.* **95**, 7157–7162 (1998).

65. Li, A. H. & Wang, H.-L. G protein-coupled receptor kinase 2 mediates μ-opioid receptor desensitization in GABAergic neurons of the nucleus raphe magnus. *J. Neurochem.* **77**, 435–444 (2001).

66. Zuo, Z. The role of opioid receptor internalization and β-arrestins in the development of opioid tolerance. *Anesth. Analg.* (2005) doi:10.1213/01.ANE.0000160588.32007.AD.

67. Bohn, L. M., Gainetdinov, R. R., Lin, F. T., Lefkowitz, R. J. & Caron, M. G. μ-opioid receptor desensitization by β-arrestin-2 determines morphine tolerance but not dependence. *Nature* (2000) doi:10.1038/35047086.

68. Zheng, H., Loh, H. H. & Law, P. Y. β-arrestin-dependent μ-opioid receptor-activated extracellular signal-regulated kinases (ERKs) translocate to nucleus in contrast to g protein-dependent ERK activation. *Mol. Pharmacol.* (2008) doi:10.1124/mol.107.039842.

69. Kuhar, J. R. *et al.* Mu opioid receptor stimulation activates c-Jun N-terminal kinase 2 by distinct arrestin-dependent and independent mechanisms. *Cell. Signal.* (2015) doi:10.1016/j.cellsig.2015.05.019.

70. Chavkin, C., Schattauer, S. S. & Levin, J. R. Arrestin-mediated activation of p38 MAPK: Molecular mechanisms and behavioral consequences. *Handb. Exp. Pharmacol.* (2014) doi:10.1007/978-3-642-41199-1

71. Skieterska, K., Rondou, P. & Van Craenenbroeck, K. Regulation of G protein-coupled receptors by ubiquitination. *International Journal of Molecular Sciences* (2017) doi:10.3390/ijms18050923.

72. Przewlocki, R. Opioid abuse and brain gene expression. *Eur. J. Pharmacol.* **500**, 331–349 (2004).

73. Yam, M. F. *et al.* General pathways of pain sensation and the major neurotransmitters involved in pain regulation. *International Journal of Molecular Sciences* (2018) doi:10.3390/ijms19082164.

74. Volkow, N. D. & Thomas McLellan, A. Opioid abuse in chronic pain-misconceptions and mitigation strategies. *New England Journal of Medicine* (2016) doi:10.1056/NEJMra1507771.

75. Weidner, C. *et al.* Neural signal processing: The underestimated contribution of peripheral human C-fibers. *J. Neurosci.* (2002) doi:10.1523/jneurosci.22-15-06704.2002.

76. Stein, C. Opioids, sensory systems and chronic pain. *European Journal of Pharmacology* (2013) doi:10.1016/j.ejphar.2013.01.076.

77. Lamas, X., Farre, M. & Cami, J. Acute effects of pentazocine, naloxone and morphine in opioid-dependent volunteers. *J. Pharmacol. Exp. Ther.* (1994).

78. Fan, T. *et al.* A role for the distal carboxyl tails in generating the novel pharmacology and G protein activation profile of μ and δ opioid receptor hetero-oligomers. *J. Biol. Chem.* (2005) doi:10.1074/jbc.M505644200.

79. Wang, D., Sun, X., Bohn, L. M. & Sadée, W. Opioid receptor homo- and heterodimerization in living cells by quantitative bioluminescence resonance energy transfer. *Mol. Pharmacol.* (2005) doi:10.1124/mol.104.010272.

80. Gomes, I. *et al.* Heterodimerization of mu and delta opioid receptors: A role in opiate synergy. *J. Neurosci.* (2000) doi:10.1523/JNEUROSCI.20-22-j0007.2000.

81. Lambert, N. A. & Javitch, J. A. Rebuttal from Nevin A. Lambert and Jonathan A. Javitch. *Journal of Physiology* (2014) doi:10.1113/jphysiol.2014.274241.

82. McGOWN, L. B. & NITHIPATIKOM, K. MOLECULAR FLUORESCENCE AND PHOSPHORESCENCE. *Appl. Spectrosc. Rev.* **35**, 353–393 (2000).

83. Förster, T. Zwischenmolekulare Energiewanderung und Fluoreszenz. *Ann. Phys.* **437**, 55–75 (1948).

84. Főrster, T. Delocalized excitation and excitation transfer. *U.S. At. Energy Comm. F. Full J. Title* (1965) doi:10.2172/4626886.

85. Bajar, B. T., Wang, E. S., Zhang, S., Lin, M. Z. & Chu, J. A Guide to Fluorescent Protein FRET Pairs. *Sensors (Basel).* **16**, 1488 (2016).

86. Woehler, A. Simultaneous quantitative live cell imaging of multiple FRET-based biosensors. *PLoS One* **8**, e61096–e61096 (2013).

87. Robinson, K. H., Yang, J. R. & Zhang, J. FRET and BRET-based biosensors in live cell compound screens. *Methods Mol. Biol.* **1071**, 217–225 (2014).

88. Berney, C. & Danuser, G. FRET or no FRET: a quantitative comparison. *Biophys. J.* **84**, 3992–4010 (2003).

89. BECKER, W. Fluorescence lifetime imaging – techniques and applications. *J. Microsc.* **247**, 119–136 (2012).

90. Chan, F. T. S., Kaminski, C. F. & Kaminski Schierle, G. S. HomoFRET Fluorescence Anisotropy Imaging as a Tool to Study Molecular Self-Assembly in Live Cells. *ChemPhysChem* **12**, 500–509 (2011).

91. Borghei, G. & Hall, E. A. H. BRET-linked ATP assay with luciferase. *Analyst* (2014) doi:10.1039/c4an00436a.

92. Piston, D. W. & Kremers, G.-J. Fluorescent protein FRET: the good, the bad and the ugly. *Trends Biochem. Sci.* **32**, 407–414 (2007).

93. Bajar, B. T. *et al.* Improving brightness and photostability of green and red fluorescent proteins for live cell imaging and FRET reporting. *Sci. Rep.* **6**, 20889 (2016).

94. McCullock, T. W., MacLean, D. M. & Kammermeier, P. J. Comparing the performance of mScarlet-I, mRuby3, and mCherry as FRET acceptors for mNeonGreen. *PLoS One* **15**, e0219886 (2020).

95. Giepmans, B. N. G., Adams, S. R., Ellisman, M. H. & Tsien, R. Y. The Fluorescent Toolbox for Assessing Protein Location and Function. *Science (80-.).* **312**, 217 LP – 224 (2006).

96. Bordeaux, J. *et al.* Antibody validation. *BioTechniques* (2010) doi:10.2144/000113382.

97. Michel, M. C., Wieland, T. & Tsujimoto, G. How reliable are G-protein-coupled receptor antibodies? *Naunyn-Schmiedeberg's Archives of Pharmacology* (2009) doi:10.1007/s00210-009-0395-y.

98. Thierauch, K.-H. Small Molecule Drugs. in *Encyclopedia of Cancer* (ed. Schwab, M.) 3448–3451 (Springer Berlin Heidelberg, 2011). doi:10.1007/978-3-642-16483-5_5374.

99. Stoddart, L. A., Kilpatrick, L. E., Briddon, S. J. & Hill, S. J. Probing the pharmacology of G protein-coupled receptors with fluorescent ligands. *Neuropharmacology* (2015) doi:10.1016/j.neuropharm.2015.04.033.

100. Gentzsch, C. *et al.* Selective and Wash-Resistant Fluorescent Dihydrocodeinone Derivatives Allow Single-Molecule Imaging of μ-Opioid Receptor Dimerization. *Angew. Chemie - Int. Ed.* (2020) doi:10.1002/anie.201912683.

101. Bosch, P. J. *et al.* Evaluation of fluorophores to label SNAP-Tag fused proteins for multicolor single-molecule tracking microscopy in live cells. *Biophys. J.* (2014) doi:10.1016/j.bpj.2014.06.040.

102. Hayashi, T. & Hamachi, I. Traceless Affinity Labeling of Endogenous Proteins for Functional Analysis in Living Cells. *Acc. Chem. Res.* **45**, 1460–1469 (2012).

103. Arttamangkul, S. *et al.* Visualizing endogenous opioid receptors in living neurons using ligand-directed chemistry. *Elife* (2019) doi:10.7554/eLife.49319.

104. Stoddart, L. A. *et al.* Ligand-directed covalent labelling of a GPCR with a fluorescent tag. *bioRxiv* 2020.04.21.053405 (2020) doi:10.1101/2020.04.21.053405.

105. Glazer, A. N. Light guides. Directional energy transfer in a photosynthetic antenna. *J. Biol. Chem.* **264**, 1–4 (1989).

106. Tsien, R. Y. THE GREEN FLUORESCENT PROTEIN. *Annu. Rev. Biochem.* **67**, 509–544 (1998).

107. Cubitt, A. B. *et al.* Understanding, improving and using green fluorescent proteins. *Trends Biochem. Sci.* **20**, 448–455 (1995).

108. Chudakov, D. M., Lukyanov, S. & Lukyanov, K. A. Fluorescent proteins as a toolkit for in vivo imaging. *Trends in Biotechnology* (2005) doi:10.1016/j.tibtech.2005.10.005.

109. Meech, S. R. Excited state reactions in fluorescent proteins. *Chem. Soc. Rev.* (2009) doi:10.1039/b820168b.

110. Frommer, W. B., Davidson, M. W. & Campbell, R. E. Genetically encoded biosensors based on engineered fluorescent proteins. *Chem. Soc. Rev.* (2009) doi:10.1039/b907749a.

111. Wiedenmann, J. *et al.* EosFP, a fluorescent marker protein with UV-inducible green-to-red fluorescence conversion. *Proc. Natl. Acad. Sci. U. S. A.* **101**, 15905 LP – 15910 (2004).

112. Lotze, J., Reinhardt, U., Seitz, O. & Beck-Sickinger, A. G. Peptide-tags for site-specific protein labelling: In vitro and in vivo. *Molecular BioSystems* (2016) doi:10.1039/c6mb00023a.

113. Howarth, M. & Ting, A. Y. Imaging proteins in live mammalian cells with biotin ligase and monovalent streptavidin. *Nat. Protoc.* (2008) doi:10.1038/nprot.2008.20.

114. Fernández-Suárez, M. *et al.* Redirecting lipoic acid ligase for cell surface protein labeling with small-molecule probes. *Nat. Biotechnol.* (2007) doi:10.1038/nbt1355.

115. Jing, C. & Cornish, V. W. A fluorogenic TMP-tag for high signal-to-background intracellular live cell imaging. *ACS Chem. Biol.* (2013) doi:10.1021/cb300657r.

116. Maier-Peuschel, M. *et al.* A fluorescence resonance energy transfer-based M2 muscarinic receptor sensor reveals rapid kinetics of allosteric modulation. *J. Biol. Chem.* **285**, 8793–8800 (2010).

117. Zürn, A. *et al.* Site-specific, orthogonal labeling of proteins in intact cells with two small biarsenical fluorophores. *Bioconjug. Chem.* (2010) doi:10.1021/bc900394j.

118. Fujishima, S. H. *et al.* Design of a multinuclear Zn(ii) complex as a new molecular probe for fluorescence imaging of His-tag fused proteins. *Chem. Commun.* (2012) doi:10.1039/c1cc16263b.

119. Litowski, J. R. & Hodges, R. S. Designing Heterodimeric Two-stranded α-Helical Coiled-coils: Effects of hydrophobicity and α-helical propensity on protein folding, stability, and specificity . *J. Biol. Chem.* **277**, 37272–37279 (2002).

120. Yano, Y., Furukawa, N., Ono, S., Takeda, Y. & Matsuzaki, K. Selective amine labeling of cell surface proteins guided by coiled-coil assembly. *Pept. Sci.* **106**, 484–490 (2016).

121. Tsutsumi, H. *et al.* Fluorogenically Active Leucine Zipper Peptides as Tag–Probe Pairs for Protein Imaging in Living Cells. *Angew. Chemie Int. Ed.* **48**, 9164–9166 (2009).

122. David, Y., Vila-Perelló, M., Verma, S. & Muir, T. W. Chemical tagging and customizing of cellular chromatin states using ultrafast trans-splicing inteins. *Nat. Chem.* **7**, 394–402 (2015).

123. Braner, M., Kollmannsperger, A., Wieneke, R. & Tampé, R. 'Traceless' tracing of proteins – high-affinity trans-splicing directed by a minimal interaction pair. *Chem. Sci.* **7**, 2646–2652 (2016).

124. Keppler, A. *et al.* A general method for the covalent labeling of fusion proteins with small molecules in vivo. *Nat. Biotechnol.* **21**, 59–86 (2003).

125. Gautier, A. *et al.* An Engineered Protein Tag for Multiprotein Labeling in Living Cells. *Chem. Biol.* **15**, 128–136 (2008).

126. Sungkaworn, T. & others. Single-molecule imaging reveals receptor–G protein interactions at cell surface hot spots. *Nature* **550**, 543–547 (2017).

127. Pries, F. *et al.* Histidine 289 Is Essential for Hydrolysis of the Alkyl-enzyme Intermediate of Haloalkane Dehalogenase. *J. Biol. Chem.* **270**, 10405–10411 (1995).

128. Los, G. *et al.* HaloTag™ Interchangeable labeling technology for cell imaging and protein capture. *Cell Notes* **11**, 2–6 (2005).

129. Marchesan, S. & Prato, M. Under the lens: Carbon nanotube and protein interaction at the nanoscale. *Chemical Communications* (2015) doi:10.1039/c4cc09173f.

130. Kaskova, Z. M., Tsarkova, A. S. & Yampolsky, I. V. 1001 lights: luciferins, luciferases, their mechanisms of action and applications in chemical analysis, biology and medicine. *Chem. Soc. Rev.* **45**, 6048–6077 (2016).

131. Pfleger, K. D. G. & Eidne, K. A. Illuminating insights into protein-protein interactions using bioluminescence resonance energy transfer (BRET). *Nat. Methods* **3**, 165–174 (2006).

132. Schihada, H. *et al.* A universal bioluminescence resonance energy transfer sensor design enables high-sensitivity screening of GPCR activation dynamics. *Commun. Biol.* **1**, 105 (2018).

133. Hall, M. P. *et al.* Engineered luciferase reporter from a deep sea shrimp utilizing a novel imidazopyrazinone substrate. *ACS Chem. Biol.* **7**, 1848–1857 (2012).

134. Patriarchi, T. & others. Ultrafast neuronal imaging of dopamine dynamics with designed genetically encoded sensors. *Science (80-.).* **360**, eaat4422 (2018).

135. Park, Y. Il, Lee, K. T., Suh, Y. D. & Hyeon, T. Upconverting nanoparticles: a versatile platform for wide-field two-photon microscopy and multi-modal in vivo imaging. *Chem. Soc. Rev.* **44**, 1302–1317 (2015).

136. Das Mikroskop. Leipzig 1867. pag. 85 ff.

137. Piston, D. W. Choosing Objective Lenses: The Importance of Numerical Aperture and Magnification in Digital Optical Microscopy. *Biol. Bull.* **195**, 1–4 (1998).

138. Axelrod, D. Total Internal Reflection Fluorescence Microscopy for Single-Molecule Studies BT - Encyclopedia of Biophysics. in (ed. Roberts, G. C. K.) 2623–2631 (Springer Berlin Heidelberg, 2013). doi:10.1007/978-3-642-16712-6_479.

139. Wang, Y. *et al.* Quantitative performance evaluation of a back-illuminated sCMOS camera with 95% QE for super-resolution localization microscopy. *Cytom. Part A* **91**, 1175–1183 (2017).

140. Cooper, J., Mullan, A., Marsh, A. & Barszczewski, M. Characterization of performance of back-illuminated SCMOS cameras versus conventional SCMOS and EMCCD cameras for microscopy applications. in *Proc.SPIE* vol. 10925 (2019).

141. Deschout, H. & Braeckmans, K. Single Particle Tracking BT - Encyclopedia of Biophysics. in (ed. Roberts, G. C. K.) 2326–2327 (Springer Berlin Heidelberg, 2013). doi:10.1007/978-3-642-16712-6_821.

142. Sauer, M. & Heilemann, M. Single-Molecule Localization Microscopy in Eukaryotes. *Chem. Rev.* **117**, 7478–7509 (2017).

143. Heilemann, M., Dedecker, P., Hofkens, J. & Sauer, M. Photoswitches: Key molecules for subdiffraction-resolution fluorescence imaging and molecular quantification. *Laser Photonics Rev.* (2009) doi:10.1002/lpor.200810043.

144. Rust, M. J., Bates, M. & Zhuang, X. Sub-diffraction-limit imaging by stochastic optical reconstruction microscopy (STORM). *Nat. Methods* **3**, 793–796 (2006).

145. Betzig, E. *et al.* Imaging Intracellular Fluorescent Proteins at Nanometer Resolution. *Science (80-.).* **313**, 1642 LP – 1645 (2006).

146. Heilemann, M. *et al.* Subdiffraction-Resolution Fluorescence Imaging with Conventional Fluorescent Probes. *Angew. Chemie Int. Ed.* **47**, 6172–6176 (2008).

147. van de Linde, S. *et al.* Photoinduced formation of reversible dye radicals and their impact on super-resolution imaging. *Photochem. Photobiol. Sci.* **10**, 499–506 (2011).

148. Endesfelder, U. & Heilemann, M. Direct Stochastic Optical Reconstruction Microscopy (dSTORM) BT - Advanced Fluorescence Microscopy: Methods and Protocols. in (ed. Verveer, P. J.) 263–276 (Springer New York, 2015). doi:10.1007/978-1-4939-2080-8_14.

149. Kottke, T., van de Linde, S., Sauer, M., Kakorin, S. & Heilemann, M. Identification of the Product of Photoswitching of an Oxazine Fluorophore Using Fourier Transform Infrared Difference Spectroscopy. *J. Phys. Chem. Lett.* **1**, 3156–3159 (2010).

150. Niekamp, S. *et al.* Nanometer-accuracy distance measurements between fluorophores at the single-molecule level. *Proc. Natl. Acad. Sci.* **116**, 4275 LP – 4284 (2019).

151. Malkusch, S. *et al.* Coordinate-based colocalization analysis of single-molecule localization microscopy data. *Histochem. Cell Biol.* **137**, 1–10 (2012).

152. Bar-On, D. *et al.* Super-resolution imaging reveals the internal architecture of nano-sized syntaxin clusters. *J. Biol. Chem.* (2012) doi:10.1074/jbc.M112.353250.

153. Karathanasis, C., Fricke, F., Hummer, G. & Heilemann, M. Molecule Counts in Localization Microscopy with Organic Fluorophores. *ChemPhysChem* **18**, 942–948 (2017).

154. Paddock, S. W. Principles and practices of laser scanning confocal microscopy. *Applied Biochemistry and Biotechnology - Part B Molecular Biotechnology* (2000) doi:10.1385/mb:16:2:127.

155. Cox, G. & Sheppard, C. J. R. Practical Limits of Resolution in Confocal and Non-Linear Microscopy. *Microsc. Res. Tech.* (2004) doi:10.1002/jemt.10423.

156. Dorsch, S., Klotz, K.-N., Engelhardt, S., Lohse, M. J. & Bünemann, M. Analysis of receptor oligomerization by FRAP microscopy. *Nat. Methods* **6**, 225–230 (2009).

157. Meral, D. *et al.* Molecular details of dimerization kinetics reveal negligible populations of transient μ-opioid receptor homodimers at physiological concentrations. *Sci. Rep.* **8**, (2018).

158. Kim, S. A., Heinze, K. G. & Schwille, P. Fluorescence correlation spectroscopy in living cells. *Nat. Methods* **4**, 963–973 (2007).

159. Mueller, J. D. Fluorescence Fluctuation Spectroscopy BT - Encyclopedia of Biophysics. in (ed. Roberts, G. C. K.) 800–803 (Springer Berlin Heidelberg, 2013). doi:10.1007/978-3-642-16712-6_504.

160. Isbilir, A. *et al.* Visualization of class A GPCR oligomerization by image-based fluorescence fluctuation spectroscopy. *bioRxiv* (2017) doi:Preprint_at: https://doi.org/10.1101/240903.

161. Chen, Y., Müller, J. D., So, P. T. & Gratton, E. The photon counting histogram in fluorescence fluctuation spectroscopy. *Biophys. J.* **77**, 553–567 (1999).

162. Digman, M. A., Dalal, R., Horwitz, A. F. & Gratton, E. Mapping the number of molecules and brightness in the laser scanning microscope. *Biophys. J.* **94**, 2320–2332 (2008).

163. Godin, A. G. *et al.* Revealing protein oligomerization and densities in situ using spatial intensity distribution analysis. *Proc. Natl. Acad. Sci. U. S. A.* (2011) doi:10.1073/pnas.1018658108.

164. Yung-Chi, C. & Prusoff, W. H. Relationship between the inhibition constant (KI) and the concentration of inhibitor which causes 50 per cent inhibition (I50) of an enzymatic reaction. *Biochem. Pharmacol.* (1973) doi:10.1016/0006-2952(73)90196-2.

165. van Unen, J. & others. A New Generation of FRET Sensors for Robust Measurement of Gαi1, Gαi2 and Gαi3 Activation Kinetics in Single Cells. *PLoS One* **11**, e0146789 (2016).

166. Klarenbeek, J., Goedhart, J., Van Batenburg, A., Groenewald, D. & Jalink, K. Fourth-generation Epac-based FRET sensors for cAMP feature exceptional brightness, photostability and dynamic range: Characterization of dedicated sensors for FLIM, for ratiometry and with high affinity. *PLoS One* (2015) doi:10.1371/journal.pone.0122513.

167. Sungkaworn, T., Rieken, F., Lohse, M. J. & Calebiro, D. High-resolution spatiotemporal analysis of receptor dynamics by single-molecule fluorescence microscopy. *J Vis Exp.* **Jul2014**, e51784 (2014).

168. Schindelin, J. & others. Fiji: an open-source platform for biological-image analysis. *Nat. Methods* **9**, 676–682 (2012).

169. Schindelin, J. *et al.* Fiji: an open-source platform for biological-image analysis. *Nat. Methods* **9**, 676–682 (2012).

170. Ovesný, M., Křížek, P., Borkovec, J., Švindrych, Z. & Hagen, G. M. ThunderSTORM: a comprehensive ImageJ plug-in for PALM and STORM data analysis and super-resolution imaging. *Bioinformatics* **30**, 2389–2390 (2014).

171. Jaqaman, K. & others. Robust single-particle tracking in live-cell time-lapse sequences. *Nat. Methods* **5**, 695–702 (2008).

172. Dupont, A., Stirnnagel, K., Lindemann, D. & Lamb, D. C. Tracking Image Correlation: Combining Single-Particle Tracking and Image Correlation. *Biophys. J.* **104**, 2373–2382 (2013).

173. Wolter, S. *et al.* Real-time computation of subdiffraction-resolution fluorescence images. *J. Microsc.* **237**, 12—22 (2010).

174. Malkusch, S. & Heilemann, M. Extracting quantitative information from single-molecule super-resolution imaging data with LAMA - LocAlization Microscopy Analyzer. *Sci. Rep.* **6**, 34486 (2016).

175. Hummer, G., Fricke, F. & Heilemann, M. Model-independent counting of molecules in single-molecule localization microscopy. *Mol. Biol. Cell* **27**, 3637–3644 (2016).

176. Serfling, R. *et al.* Quantitative Single-Residue Bioorthogonal Labeling of G Protein-Coupled Receptors in Live Cells. *ACS Chem. Biol.* **14**, 1141–1149 (2019).

177. Trullo, A., Corti, V., Arza, E., Caiolfa, V. R. & Zamai, M. Application limits and data correction in number of molecules and brightness analysis. *Microsc. Res. Tech.* **76**, 1135–1146 (2013).

178. Group, E. S. & Microsystems, L. FRET Acceptor PhotoBleaching (AB) in LASAF. *Confocal Appl. Notes* (2006).

179. Hoffmann, M., Fröhner, C. & Noé, F. ReaDDy 2: Fast and flexible software framework for interacting-particle reaction dynamics. *PLOS Comput. Biol.* **15**, 1–26 (2019).

180. Grimm, J. B. & others. A general method to improve fluorophores for live-cell and single-molecule microscopy. *Nat. Methods* **12**, 244–250 (2015).

181. Grimm, J. B., Brown, T. A., English, B. P., Lionnet, T. & Lavis, L. D. Synthesis of Janelia Fluor HaloTag and SNAP-Tag Ligands and their Use in cellular imaging experiments. *Methods Mol. Biol.* 179–188 (2017) doi:https://doi.org/10.1007/978-1-4939-7265-4_15.

182. Greene, J. L. & others. Covalent dimerization of CD28/CTLA-4 and oligomerization of CD80/CD86 regulate T cell costimulatory interactions. *J Biol Chem.* **271**, 26762–26771 (1996).

183. Dalal, R. B., Digman, M. A., Horwitz, A. F., Vetri, V. & Gratton, E. Determination of particle number and brightness using a laser scanning confocal microscope operating in the analog mode. *Microsc. Res. Tech.* (2008) doi:10.1002/jemt.20526.

184. Fries, J. R., Brand, L., Eggeling, C., Köllner, M. & Seidel, C. A. M. Quantitative Identification of Different Single Molecules by Selective Time-Resolved Confocal Fluorescence Spectroscopy. *J. Phys. Chem. A* **102**, 6601–6613 (1998).

185. Pasternak, G. W. & Snyder, S. H. Identification of novel high affinity opiate receptor binding in rat brain. *Nature* (1975) doi:10.1038/253563a0.

186. Ward, S. J., Portoghese, P. S. & Takemori, A. E. Pharmacological characterization in vivo of the novel opiate, β-funaltrexamine. *J. Pharmacol. Exp. Ther.* (1982).

187. Keith, D. E. *et al.* Morphine activates opioid receptors without causing their rapid internalization. *J. Biol. Chem.* (1996) doi:10.1074/jbc.271.32.19021.

188. He, L., Fong, J., von Zastrow, M. & Whistler, J. L. Regulation of Opioid Receptor Trafficking and Morphine Tolerance by Receptor Oligomerization. *Cell* **108**, 271–282 (2002).

189. Anselmi, L., Jaramillo, I., Palacios, M., Huynh, J. & Sternini, C. Ligand-induced μ opioid receptor internalization in enteric neurons following chronic treatment with the opiate fentanyl. *J. Neurosci. Res.* (2013) doi:10.1002/jnr.23214.

190. Yu, Y. *et al.* μ Opioid receptor phosphorylation, desensitization, and ligand efficacy. *J. Biol. Chem.* (1997) doi:10.1074/jbc.272.46.28869.

191. Doll, C. *et al.* Agonist-selective patterns of μ-opioid receptor phosphorylation revealed by phosphosite-specific antibodies. *Br. J. Pharmacol.* (2011) doi:10.1111/j.1476-5381.2011.01382.x.

192. Williams, J. T. *et al.* Regulation of μ-opioid receptors: Desensitization, phosphorylation, internalization, and tolerance. *Pharmacological Reviews* (2013) doi:10.1124/pr.112.005942.

193. Huang, P. & others. Functional role of a conserved motif in TM6 of the rat mu opioid receptor: constitutively active and inactive receptors result from substitutions of Thr6.34(279) with Lys and Asp.. *Biochemistry* **40**, 13501–13509 (2001).

194. Avigan, J. *et al.* Pertussis toxin-catalyzed ADP-ribosylation of G0.alpha. with mutations at the carboxyl terminus. *Biochemistry* **31**, 7736–7740 (1992).

195. Brillet, K., Kieffer, B. L. & Massotte, D. Enhanced spontaneous activity of the mu opioid receptor by cysteine mutations: Characterization of a tool for inverse agonist screening. *BMC Pharmacol.* (2003) doi:10.1186/1471-2210-3-14.

196. Sadée, W., Wang, D. & Bilsky, E. J. Basal opioid receptor activity, neutral antagonists, and therapeutic opportunities. *Life Sciences* (2005) doi:10.1016/j.lfs.2004.10.024.

197. Einstein, A. Über die von der molekularkinetischen Theorie der Wärme geforderte Bewegung von in ruhenden Flüssigkeiten suspendierten Teilchen. *Ann. Phys.* (1905) doi:10.1002/andp.19053220806.

198. Miess, E. *et al.* Multisite phosphorylation is required for sustained interaction with GRKs and arrestins during rapid μ-opioid receptor desensitization. *Sci. Signal.* **11**, (2018).

199. Willox, A. K., Sahraoui, Y. M. E. & Royle, S. J. Non-specificity of Pitstop 2 in clathrin-mediated endocytosis. *Biol. Open* (2014) doi:10.1242/bio.20147955.

200. Stahlschmidt, W., Robertson, M. J., Robinson, P. J., McCluskey, A. & Haucke, V. Clathrin terminal domain-ligand interactions regulate sorting of mannose 6-phosphate receptors mediated by AP-1 and GGA adaptors. *J. Biol. Chem.* (2014) doi:10.1074/jbc.M113.535211.

201. Hua, Y. *et al.* Blocking endocytosis enhances short-term synaptic depression under conditions of normal availability of vesicles. *Neuron* (2013) doi:10.1016/j.neuron.2013.08.010.

202. Fürstenberg, A. & Heilemann, M. Single-molecule localization microscopy-near-molecular spatial resolution in light microscopy with photoswitchable fluorophores. *Physical Chemistry Chemical Physics* (2013) doi:10.1039/c3cp52289j.

203. Sauer, M. A Practical Guide to dSTORM: Super-Resolution Imaging with Standard Fluorescent Probes. in (2012). doi:10.1007/4243_2012_41.

204. Dietz, M. S. & Heilemann, M. Optical super-resolution microscopy unravels the molecular composition of functional protein complexes. *Nanoscale* **11**, 17981–17991 (2019).

205. Fricke, F., Beaudouin, J., Eils, R. & Heilemann, M. One, two or three? Probing the stoichiometry of membrane proteins by single-molecule localization microscopy. *Sci. Rep.* **5**, 14072 (2015).

206. Grushevskyi, E. & others. Stepwise activation of a class C GPCR begins with millisecond dimer rearrangement. *Proc Natl Acad Sci U S A* **116**, 10150–10155 (2019).

207. Lohse, M. J., Nuber, S. & Hoffmann, C. Fluorescence/Bioluminescence Resonance Energy Transfer Techniques to Study G-Protein-Coupled Receptor Activation and Signaling. *Pharmacol. Rev.* **64**, 299–336 (2012).

208. Gradinaru, V. *et al.* Molecular and Cellular Approaches for Diversifying and Extending Optogenetics. *Cell* (2010) doi:10.1016/j.cell.2010.02.037.

209. Haryadi, R. *et al.* Optimization of heavy chain and light chain signal peptides for high level expression of therapeutic antibodies in CHO cells. *PLoS One* (2015) doi:10.1371/journal.pone.0116878.

210. Coloma, M. J., Hastings, A., Wims, L. A. & Morrison, S. L. Novel vectors for the expression of antibody molecules using variable regions generated by polymerase chain reaction. *J. Immunol. Methods* (1992) doi:10.1016/0022-1759(92)90092-8.

211. Yoshimura, K. *et al.* Successful immunogene therapy using colon cancer cells (colon 26) transfected with plasmid vector containing mature interleukin-18 cDNA and the Igκ leader sequence. *Cancer Gene Ther.* (2001) doi:10.1038/sj.cgt.7700277.

212. Yanagawa, M. Single-molecule diffusion-based estimation of ligand effects on G protein–coupled receptors. *Sci. Signal.* **11**, eaao1917 (2018).

213. Metz, M., Pennock, R., Krapf, D. & Hentges, S. Temporal dependence of shifts in mu opioid receptor mobility at the cell surface after agonist binding observed by single-particle tracking. *Sci. Rep.* **9**, 7297 (2019).

214. Grundmann, M. & Kostenis, E. Temporal Bias: Time-Encoded Dynamic GPCR Signaling. *Trends in Pharmacological Sciences* (2017) doi:10.1016/j.tips.2017.09.004.

215. Kupchik, Y. M. *et al.* A novel fast mechanism for GPCR-mediated signal transduction - Control of neurotransmitter release. *J. Cell Biol.* (2011) doi:10.1083/jcb.201007053.

216. Jullié, D. *et al.* A Discrete Presynaptic Vesicle Cycle for Neuromodulator Receptors. *Neuron* (2020) doi:10.1016/j.neuron.2019.11.016.

217. Stoeber, M. *et al.* A Genetically Encoded Biosensor Reveals Location Bias of Opioid Drug Action. *Neuron* (2018) doi:10.1016/j.neuron.2018.04.021.

218. Gondin, A. B., Halls, M. L., Canals, M. & Briddon, S. J. GRK Mediates μ-Opioid Receptor Plasma Membrane Reorganization. *Front. Mol. Neurosci.* **12**, 104 (2019).

219. Bhatia, S., Edidin, M., Almo, S. C. & Nathenson, S. G. Different cell surface oligomeric states of B7-1 and B7-2: Implications for signaling. *Proc. Natl. Acad. Sci.* **102**, 15569–15574 (2005).

220. Jordan, B. A., Gomes, I., Rios, C., Filipovska, J. & Devi, L. A. Functional Interactions between μ- Opioid and α2A-Adrenergic Receptors. *Mol. Pharmacol.* **64**, 1317–1324 (2003).

221. Lambert, N. A. GPCR dimers fall apart. *Science Signaling* (2010) doi:10.1126/scisignal.3115pe12.

222. Whorton, M. R. *et al.* Efficient coupling of transducin to monomeric rhodopsin in a phospholipid bilayer. *J. Biol. Chem.* (2008) doi:10.1074/jbc.M703346200.

223. Leitz, A. J., Bayburt, T. H., Barnakov, A. N., Springer, B. A. & Sligar, S. G. Functional reconstitution of β2-adrenergic receptors utilizing self-assembling Nanodisc technology. *Biotechniques* (2006) doi:10.2144/000112169.

224. Williams, J. T. *et al.* Regulation of μ-opioid Receptors: Desensitization, Phosphorylation, Internalization, and Tolerance. *Pharmacol. Rev.* **65**, 223–254 (2013).

225. Kang, Y. *et al.* Crystal structure of rhodopsin bound to arrestin by femtosecond X-ray laser. *Nature* (2015) doi:10.1038/nature14656.

226. Huang, W. *et al.* Structure of the neurotensin receptor 1 in complex with β-arrestin 1. *Nature* (2020) doi:10.1038/s41586-020-1953-1.

227. Yin, W. *et al.* A complex structure of arrestin-2 bound to a G protein-coupled receptor. *Cell Res.* (2019) doi:10.1038/s41422-019-0256-2.

228. Chen, Q. *et al.* Self-association of arrestin family members. *Handb. Exp. Pharmacol.* (2014) doi:10.1007/978-3-642-41199-1_11.

229. Zhan, X., Gimenez, L. E., Gurevich, V. V. & Spiller, B. W. Crystal structure of arrestin-3 reveals the basis of the difference in receptor binding between two non-visual subtypes. *J. Mol. Biol.* (2011) doi:10.1016/j.jmb.2010.12.034.

230. Sommer, M. E., Hofmann, K. P. & Heck, M. Arrestin-Rhodopsin Binding Stoichiometry in Isolated Rod Outer Segment Membranes Depends on the Percentage of Activated Receptors. *J. Biol. Chem.* **286**, 7359–7369 (2011).

231. Beyrière, F. *et al.* Formation and Decay of the Arrestin·Rhodopsin Complex in Native Disc Membranes. *J. Biol. Chem.* **290**, 12919–12928 (2015).

232. Lohse, M. J. & Hoffmann, C. Arrestin interactions with G protein-coupled receptors. in *Arrestins-Pharmacology and Therapeutic Potential* 15–56 (Springer, 2014).

233. Sposini, S. *et al.* Integration of GPCR Signaling and Sorting from Very Early Endosomes via Opposing APPL1 Mechanisms. *Cell Rep.* (2017) doi:10.1016/j.celrep.2017.11.023.

234. Jean-Alphonse, F. *et al.* Spatially restricted G protein-coupled receptor activity via divergent endocytic compartments. *J. Biol. Chem.* (2014) doi:10.1074/jbc.M113.526350.

235. Rouault, A. A. J. *et al.* The GPCR accessory protein MRAP2 regulates both biased signaling and constitutive activity of the ghrelin receptor GHSR1a. *Sci. Signal.* **13**, eaax4569 (2020).

236. Lommerse, P. H. M. *et al.* Single-Molecule Imaging of the H-Ras Membrane-Anchor Reveals Domains in the Cytoplasmic Leaflet of the Cell Membrane. *Biophys. J.* **86**, 609–616 (2004).

237. Manglik, A. *et al.* Structure-based discovery of opioid analgesics with reduced side effects. *Nature* (2016) doi:10.1038/nature19112.

238. Kliewer, A. *et al.* Phosphorylation-deficient G-protein-biased μ-opioid receptors improve analgesia and diminish tolerance but worsen opioid side effects. *Nat. Commun.* (2019) doi:10.1038/s41467-018-08162-1.

239. Gillis, A. *et al.* Low intrinsic efficacy for G protein activation can explain the improved side effect profiles of new opioid agonists. *Sci. Signal.* **13**, eaaz3140 (2020).

240. Nikolaev, V. O., Bünemann, M., Hein, L., Hannawacker, A. & Lohse, M. J. Novel single chain cAMP sensors for receptor-induced signal propagation. *J. Biol. Chem.* (2004) doi:10.1074/jbc.C400302200.

241. Surdo, N. C. *et al.* FRET biosensor uncovers cAMP nano-domains at b-adrenergic targets that dictate precise tuning of cardiac contractility. *Nat. Commun.* (2017) doi:10.1038/ncomms15031.

242. Hackley, C. R., Mazzoni, E. O. & Blau, J. cAMPr: A single-wavelength fluorescent sensor for cyclic AMP. *Sci. Signal.* (2018) doi:10.1126/scisignal.aah3738.

243. Grimm, J. B. *et al.* A general method to fine-tune fluorophores for live-cell and in vivo imaging. *Nat. Methods* (2017) doi:10.1038/nmeth.4403.

244. Xia, Y. & Kellems, R. E. Receptor-activating autoantibodies and disease: preeclampsia and beyond. *Expert Rev. Clin. Immunol.* **7**, 659–674 (2011).

245. Borda, E. *et al.* A circulating IgG in Chagas' disease which binds to beta-adrenoceptors of myocardium and modulates their activity. *Clin. Exp. Immunol.* **57**, 679–686 (1984).

246. Jahns, R., Boivin, V. & Lohse, M. J. β1-Adrenergic Receptor Function, Autoimmunity, and Pathogenesis of Dilated Cardiomyopathy. *Trends Cardiovasc. Med.* **16**, 20–24 (2006).

247. Jahns, R. *et al.* Direct evidence for a beta 1-adrenergic receptor-directed autoimmune attack as a cause of idiopathic dilated cardiomyopathy. *J. Clin. Invest.* **113**, 1419–1429 (2004).

248. Magnusson, Y., Wallukat, G., Waagstein, F., Hjalmarson, A. & Hoebeke, J. Autoimmunity in idiopathic dilated cardiomyopathy. Characterization of antibodies against the beta 1-adrenoceptor with positive chronotropic effect. *Circulation* **89**, 2760–2767 (1994).

249. Hutchings, C. J. *et al.* Monoclonal anti-β1-adrenergic receptor antibodies activate G protein signaling in the absence of β-arrestin recruitment. *MAbs* **6**, 246–261 (2014).

250. Hans-Peter, H. *et al.* Detection of Anti–β1-AR Autoantibodies in Heart Failure by a Cell-Based Competition ELISA. *Circ. Res.* **111**, 675–684 (2012).

251. Lee, Y. *et al.* Molecular basis of β-arrestin coupling to formoterol-bound β1-adrenoceptor. *Nature* (2020) doi:10.1038/s41586-020-2419-1.

252. Rock, E. P., Sibbald, P. R., Davis, M. M. & Chien, Y. H. CDR3 length in antigen-specific immune receptors. *J. Exp. Med.* **179**, 323–328 (1994).

253. Yokoyama, H., Mizutani, R., Noguchi, S. & Hayashida, N. Structural and biochemical basis of the formation of isoaspartate in the complementarity-determining region of antibody 64M-5 Fab. *Sci. Rep.* **9**, 18494 (2019).

254. Manglik, A. *et al.* Structural Insights into the Dynamic Process of β2-Adrenergic Receptor Signaling. *Cell* **161**, 1101–1111 (2015).

255. Weis, W. I. & Kobilka, B. K. The Molecular Basis of G Protein-Coupled Receptor Activation. *Annu. Rev. Biochem.* **87**, 897–919 (2018).

256. Andrews, S. J. & Rothnagel, J. A. Emerging evidence for functional peptides encoded by short open reading frames. *Nat. Rev. Genet.* **15**, 193–204 (2014).

257. Liu, Z. *et al.* Systematic comparison of 2A peptides for cloning multi-genes in a polycistronic vector. *Sci. Rep.* **7**, 2193 (2017).

258. Inoue, A. *et al.* Illuminating G-Protein-Coupling Selectivity of GPCRs. *Cell* **177**, 1933-1947.e25 (2019).

9. Annex

Individual datapoints and P values of the waterfall plots shown in this work:

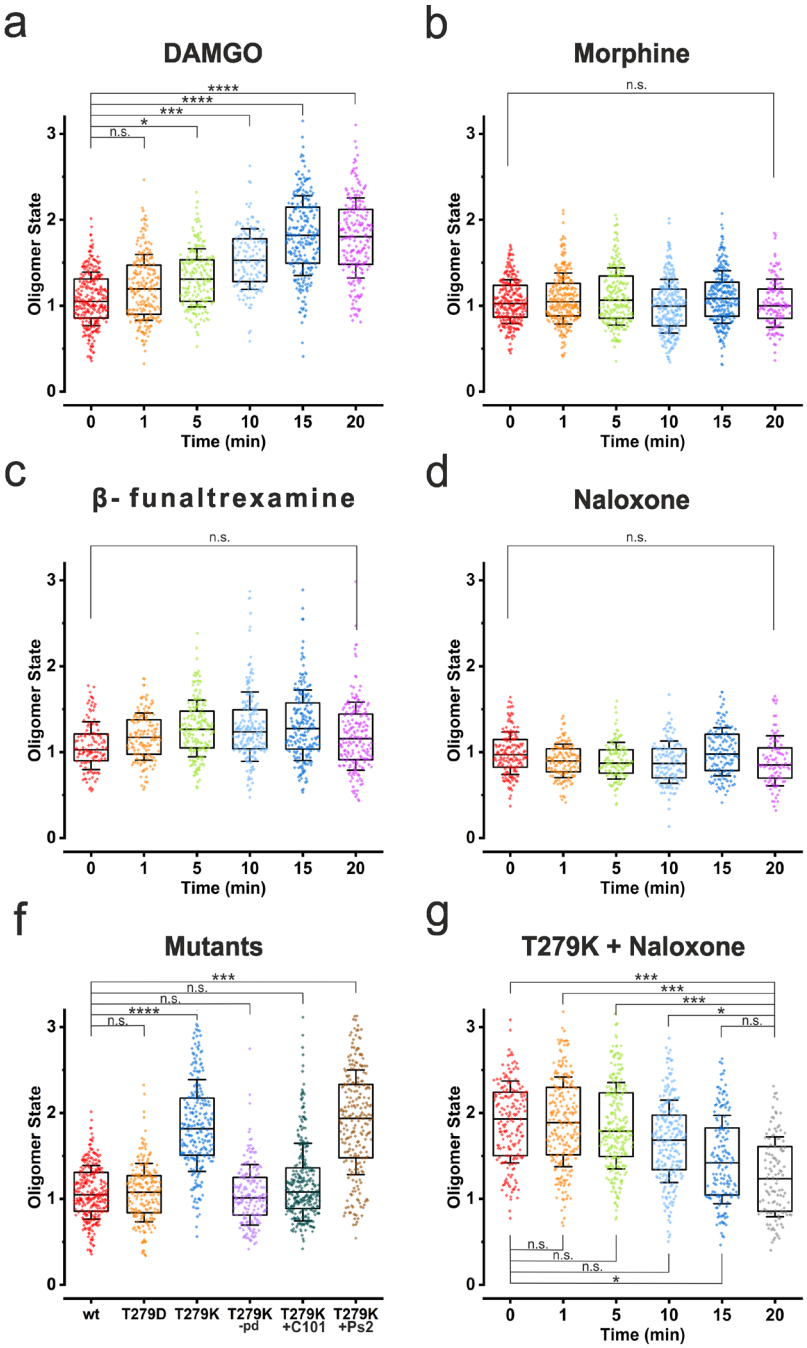

Panel A:			Panel F:			Panel G:	
Tukey's multiple comparisons test	P Value		Tukey's multiple comparisons test	P Value		Tukey's multiple comparisons test	P Value
Basal vs. 1 minute	0.9719		wt vs. T279D	>0.9999		Basal vs. 1 minute	>0.9999
Basal vs. 5 minutes	0.0404		wt vs. T279K	<0.0001		Basal vs. 5 minutes	0.9413
Basal vs. 10 minutes	0.0009		wt vs. T279K-pd	0.8788		Basal vs. 10 minutes	0.8421
Basal vs. 15 minutes	<0.0001		wt vs. T279K+C101	0.7124		Basal vs. 15 minutes	0.0118
Basal vs. 20 minutes	<0.0001		wt vs. T279K+PS2	<0.0001		Basal vs. 20 minutes	0.0003
Panel B:						1 minute vs. 20 minutes	0.0008
Basal vs. 20 minutes	0.9933					5 minutes vs. 20 minutes	0.0011
Panel C:						10 minutes vs. 20 minutes	0.0447
Basal vs. 20 minutes	0.0743					15 minutes vs. 20 minutes	>0.9999
Panel D:							
Basal vs. 20 minutes	0.0901						

P values are based on a one-way ANOVA followed by Tukey's multiple comparison test. Box- plots show median, the box is IQR and whiskers show SD.

10. Curriculum vitae

11. Acknowledgements

First, I want to thank my primary PhD supervisor Prof. Dr. Martin Lohse for giving me the unique opportunity to conduct my doctoral studies in his lab. It has been an impressive period of my life and I learned a lot from him during scientific as well as non-scientific conversations. Even in very busy times with short availabilities, he never gave me the feeling of being on my own or lacking his support for upcoming challenges or issues. His very comprehensive support in writing, rewriting and re-rewriting of my first publication was extremely motivating and it would have been impossible without him. Despite his exceptional knowledge of pharmacology and the promoting scientific discussions, he enabled me to get in contact with an outstanding community of researchers around the whole globe, an experience for which I am incredibly grateful. I believe that I could not have done a better choice of supervisor for my doctoral studies, an exceptionally exciting time, which allowed me to find my passion for science.

Furthermore, I want thank Prof. Dr. Michael Decker for his supportive opinions and discussions during annual thesis committee meetings as well as during retreats of the Elitenetwork of Bavaria (ENB). I am also very pleased that he included me into a very interesting publication of his lab. A very special thank goes also to my international supervisor Prof. Dr. Marta Filizola, who triggered an uncountable number of fruitful discussions during annual thesis committee meetings, regular Skype calls and several GPCR conferences. It was additionally a great experience to work together with her on a publication on receptor dimerization kinetics and I am very happy that I was included into this work. I am looking forward to keep this collaboration active after my doctoral studies and hope on a further follow-up publication in the close future. Finally, I would like to thank Prof. Dr. Markus Sauer very much for his support and for agreeing to join my Thesis Committee at short notice.

The most elementary acknowledgement goes to my parents. They enabled to my sister and me our undergraduate studies, which were the essential requirement to conduct my doctoral studies. Without their tremendous support during all phases of my life and an unbelievable patience, this would not have been possible neither. The promise of my father “I would give the shirt off my back for my children”, was something which definitely holds true for my mother and himself. Furthermore, I want to thank my sister Janine Möller and her family for being always supportive to me in several important times of my life.

A very special thank goes also to Titiwat Sungkaworn, who was a superior mentor with a very thorough, diligent, precise and patient working attitude. He has furthermore fascinating mentorship skills, which made working with him always a pleasure, but was at the same time highly efficient and educating. Apart from that he is also outside of the working environment a really good friend.

Finally, I also want to thank my friends and colleagues from the lab, especially those three uniquely reliable and honest (sometimes too honest) people that became during this time like my brothers: Ali Išbilir, Yevgenii Grushevskyi and Hannes Schihada. Not less important were also the two lab sisters, which were always a safe back up one could rely on: Selma Anton and Katharina Nemec. From the Würzburg-team I want to thank Ulrike Zabel and Monika Frank for their great support with molecular cloning, Christine Salomon for rescuing me in all administrative problems which I encountered throughout my PhD studies, Annette Hannawacker for supporting me with cells and Nadine Yurdagül

for helping me out with reagents and her consulting on antibodies. I further want to thank the Berlin-team especially Ruth Pareja, Bärbel Pohl and Marlies Grieben for their technical as well as mental support.

Moreover, I want to thank the outstanding team of collaborators which supported the publication of my first paper: Vikram Sunkara, Brendan Osberg, Christos Karathanasis, Mike Heilemann and Christof Schütte

Ultimately, I want to thank all the people, which are not related to science but were not less important and supportive during this period of my life: Markus Müller, Tobias Kiwitz, Milan Kosanovic and his mother, Jan-Christoph Witke, Susen Berger, Jim Edosah and a few more people that stay unmentioned here.

You were all a great support in many different ways,

Thank you!